UNIVERSITY OF OKLAHOMA

GRADUATE COLLEGE

RECEIVER FUNCTION IMAGING OF DEEP AND SHALLOW SUBSURFACE STRUCTURES OF OKLAHOMA

A DISSERTATION

SUBMITTED TO THE GRADUATE FACULTY

in partial fulfillment of the requirements for the

Degree of

DOCTOR OF PHILOSOPHY

By

ZHUOBO WANG

Norman, Oklahoma

2023

Downloaded from SHAREOK. Persistent Handle URL: https://hdl.handle.net/11244/338821

RECEIVER FUNCTION IMAGING OF DEEP AND SHALLOW SUBSURFACE STRUCTURES OF OKLAHOMA

A DISSERTATION APPROVED FOR THE
SCHOOL OF GEOSCIENCES

BY THE COMMITTEE CONSISTING OF

Dr. Brett M. Carpenter, Chair

Dr. Xiaowei Chen, Co-Chair

Dr. Junle Jiang

Dr. Michael Behm

Dr. Xingru Wu

Chapter [2] was previously published as:

Wang, Z., Behm, M., Persaud, P., Chen, X., & Carpenter, B. M. (2023). New insights on Moho depth and regional lithospheric structure of central Oklahoma based on receiver function analysis from dense seismic networks. *Tectonophysics, 854*, 229818. https://doi.org/10.1016/j.tecto.2023.229818 © 2023 Elsevier B.V.

All other content © Copyright by ZHUOBO WANG 2023

All rights reserved.

Table of Contents

Table of Contents ..... **iv**

List of Figures ..... **vi**

List of Tables ..... **xiv**

Acknowledgement ..... **xv**

Abstract of the Dissertation ..... **xvii**

1 Introduction **1**

1.1 Introduction 1

1.2 P-to-S Receiver function 4

1.3 Overview of the dissertation 6

1.4 Structure of the dissertation 8

1.5 References 10

2 New Insights on Moho Depth and Regional Lithospheric Structure of Central Oklahoma Based on Receiver Function Analysis from Dense Seismic Networks **17**

2.1 Abstract 17

2.2 Introduction 18

2.3 Geologic and Tectonic Setting 24

2.4 Data and Methods 26

2.5 Results 29

2.5.1 Stacked RF 30

2.5.2 Moho Depth Map 33

2.6 Discussion 35

2.6.1 Moho Depths 35

2.6.2 Integration with basement depths, crustal velocities, and potential field datasets 37

2.6.3 Mid-Continent Rift 44

2.6.4 Mid-lithospheric discontinuity (MLD) 46

2.7 Conclusions 48

2.8 References 50

3 High-resolution Receiver Function Imaging Using Local Earthquakes and a Multi-channel Inversion Routine **64**

3.1 Abstract 64

3.2 Introduction 65
3.3 Method 68
3.4 Forward modeling of local earthquakes 76
3.5 Application of the blind receiver function methodology to real data 79
3.5.1 Area and geology 79
3.5.2 Data 81
3.5.3 Application and results 85
3.6 Discussion 91
3.6.1 Shallow RF imaging with local earthquakes 91
3.6.2 Cushing Fault structure 93
3.7 Conclusion 99
3.8 References 100
4 Comparative Analysis of the Teleseismic Event Record by Multiple Distributed Acoustic Sensing Arrays 110
4.1 Abstract 110
4.2 Introduction 111
4.3 Array and Data information 114
4.4 Waveform Analysis 118
4.4.1 Overview of DAS data quality 118
4.4.2 Comparison of stacked DAS data and broadband seismometer data 124
4.4.3 Spectral Analysis 130
4.5 DAS Receiver functions. 134
4.6 Discussion 137
4.7 Conclusion 139
4.8 References 140
5 Conclusions and Future Work 146
5.1 Conclusion 146
5.2 Future work 147
Appendix 149
A1. Station and event information 149
A2. $\mathbf{H-\kappa}$ stacking results and Moho depth from depth converted RFs 158
A3. Uncertainty analysis 167

List of Figures

Figure 1.1 a) Diagram of the teleseismic P wave, converted S wave and multiples, and b) representation of receiver function waveform of the two-layer model depicted in a). 5

Figure 2.1 Bouguer gravity anomaly map of the study area and its surroundings (*Gravity anomaly map of North America [Map]*, 1988). Tectonic provinces are defined by black dashed lines (Modified from Bickford et al., 2015). The southern extension of the western arm of MCR as proposed by (Adams and Keller, 1996; Stein *et al.*, 2014) is indicated by the red dashed line. The gray dashed line is the Nd line. A high-pass wavelength filter (200 km) is applied to the gravity data to suppress upper mantle features. 21

Figure 2.2 Main geologic provinces and major faults in Oklahoma (Oklahoma Geological Provinces [Map] by Oklahoma Geological Survey). Blue triangles show the seismic stations used in this study. Geological features (platform and shelf, basin, and uplift) are shown in different colors. 22

Figure 2.3 The distribution of teleseismic events used in the receiver function analysis. The state of Oklahoma is shown in red in the center of the map. Event magnitudes are indicated with different colors. 29

Figure 2.4 Stacked RF traces for each station grouped by geological provinces and waveform characteristics. a) The Anadarko shelf, b) the Nemaha uplift, c) the Northern Cherokee Platform, d) the Anadarko Basin, and e) the Southern Cherokee Platform. The RF traces are plotted by station longitude at the Anadarko shelf and the Nemaha uplift region and by station latitude at the Northern Cherokee Platform, the Southern Cherokee Platform, and the Anadarko Basin. Interpreted intracrustal layer, P-to-S conversion of Moho, and negative velocity gradient (NVG)

are marked. The stations of each subset are shown with different colors on top of the basement depth map of the study area (Campbell and Weber, 2006). 32
Figure 2.5 The interpolated Moho depth map. Grey lines indicate major basement faults. The red shape encompasses the possible continuation of the MCR into Oklahoma as proposed by C. A. Stein (2014). 35
Figure 2.6 RF Pseudo-cross section A-B overlain with crustal P wave velocity anomaly (Ratre and Behm, 2021). The velocity anomaly represents the deviation of an average 1D velocity-depth function. The thick black line is the Moho depth extracted from the interpolated Moho depth map (Figure 2.5). The grey line is the intracrustal discontinuity, and the pink line denotes the MLD (mid-lithospheric discontinuity) of the upper mantle. This profile is from the Anadarko Shelf, trending southeast, to the Cherokee Platform near central Oklahoma as shown in the inset map. Above the cross-section, the magnetic anomaly (green line), Bouguer gravity anomaly (red line), and basement depths (black line) along the profile are shown. The overlapping region of the proposed MCR with this profile is marked with a shaded rectangle. Note that the equidistant trace spacing does not represent true inter-station distances. Uncertainty of Moho estimation prior to interpolation and smoothing is plotted with blue error bars on top of the Pms phase. 39
Figure 2.7 RF Pseudo-cross section A-C overlapped with crustal P wave anomaly. This profile is from the Anadarko Shelf, trending east to the northern part of the Cherokee Platform. All lines, symbols and annotations are the same as in Figure 2.6. 42
Figure 2.8 RF Pseudo-cross section D-E overlapped with crustal P wave anomaly (Ratre and Behm, 2021). This profile is from the Nemaha Uplift, trending south, to the Arbuckle Uplift near the Southern Oklahoma Aulacogen. All lines, symbols and annotations are the same as in Figure 6 while the location of the intersection between this profile and the Nd line is denoted. 43

Figure 3.1 Wave propagation diagram of receiver function and b) blind deconvolution scheme. Note the dashed line represents converted S-wave. 69
Figure 3.2 Wave propagation diagram of direct P wave and surface multiples. Note the dashed line represents surface reflected wave in the blind deconvolution scheme. 71
Figure 3.3 Synthetic waveform of local earthquakes and diagram of wave propagation at receiver side. a) Synthetic vertical component of local earthquakes at five receivers with different epicentral distance b) Synthetic radial component of local earthquakes at five receivers with different epicentral distance c) Wave propagation diagram with phases that are considered in the synthetic waves. Note that the dashed line represents converted S-wave. 78
Figure 3.4 Map view of Cushing nodal array and 2015 earthquake sequence overlaid by basement depth. The background is the basement depth map derived from basement penetrating wells (Northcutt and Campbell, 1996). Two coordinate axes (inline, crossline) used in the following figures are plotted in yellow arrows. 81
Figure 3.5 Map view of local and regional events used in this study. Earthquake events are plotted in red circles in different sizes which represent the relative magnitude of each event. 83
Figure 3.6 An example of a local earthquake recorded by selected stations of the Cushing array. Event information: epicentral distance: 1.01 degrees; Magnitude: 2.8 (Mw) a) Raw vertical component of this event. b) Normalized power spectral density of this event. The power spectral density of each single trace in a) present green lines while the red line indicates average power spectral density of all selected traces c) Aligned radial component of this event raw vertical component of this event. D) Aligned vertical component of this event. 84

Figure 3.7 Projection of all blind RFs on a vertical plane perpendicular to the fault strike (see yellow axes in Figure 3.4). Note the prominent P-to-S conversion that is marked by dashed line. 88

Figure 3.8 Projection of all blind RFs on a vertical plane parallel to the fault strike (see yellow axes in Figure 3.4). Note the prominent P-to-S conversion that is marked by dashed line. 89

Figure 3.9 Zoomed projection of all RFs by in-line fault distance with extracted basement depth (solid black line) from OGS basement map (Figure 3.4). Depth derived from the velocity model mentioned in the text is labeled on the ride side of this pseudo-cross-section. 91

Figure 3.10 Left: RF cross-section of an east-west path in the array. Red line: interpreted basement top conversion. Right: Map view of the array geometry, with black line denoting the cross-section array shown in the left. The red, green and blue circles mark the start station, intersection with the fault strike and end station of the cross-section, respectively. 95

Figure 3.11 Left: RF cross-section of an east-west path in the array. Red line: interpreted basement top conversion. Right: Map view of the array geometry, with black line denoting the cross-section array shown in the left. The red, green and blue circles mark the start station, intersection with the fault strike and end station of the cross-section, respectively. 96

Figure 3.12 Left: RF cross-section of an north-south path in the array. Red line: interpreted basement top conversion. Right: Map view of the array geometry, with black line denoting the cross-section array shown in the left. The red, green and blue circles mark the start station, intersection with the fault strike and end station of the cross-section, respectively. 97

Figure 3.13 Projection of RFs and M5 Cushing sequence hypocenters (black circles) perpendicular to the fault following the diagram in Figure 3.3. Black line: interpreted basement top conversion. Red square box: area of basement conversion right above the vertical fault

geometry. Depth derived from the velocity model mentioned in the text is labeled on the ride side of this pseudo-cross-section. 98

Figure 4.1 Map view of the Alaska Peninsula Mw 8.2 earthquake and Ridgecrest, Enid, and State College DAS array. The epicenter of the earthquake is marked by a red circle and DAS array location is marked by black triangles. Epicentral distance is marked in the figure for each array. 114

Figure 4.2 Local map view of a) Enid town location in northwest Oklahoma, b) relative position between Enid DAS array (color path) and nearby broadband station (OK-AMES, OK-CROK), and c) Enid DAS array that goes through Enid town. Note the DAS array is plotted in different colors with numbers that represent segments assigned by cable geometry. 116

Figure 4.3 Local map view of Ridgecrest location in south California and relative position between Ridgecrest DAS array with segment number and nearby broadband station (CI-SRT). 117

Figure 4.4 Local map view of a) State College location in central Pennsylvania, b) relative position between FORESEE-urban DAS array and a nearby broadband station (IU-SSPA), and c) FORESEE-urban DAS array with segments number that passes through State College. 118

Figure 4.5 Enid DAS data (strain rate, bandpass filter: 0.02-1 Hz) of the Alaska Peninsula earthquake. a) Normalized strain rate waveform of Enid DAS array b) Normalized strain rate waveform of first three segments (channel 1- 726). Segment assignment of the whole array is laid out at the left side of a) whose color is consistent with that in Figure 4.2. For comparison, the east channel of OK-AMES is overplotted in solid black line. The arrival time of P wave and S wave for AMES is marked in red line. Yellow arrows in (a) point out passing traffic signals along

state highway. Shaded channels in a) denote the segments that have higher SNR which is zoomed in at the bottom figure. 121
Figure 4.6 Ridgecrest DAS data (strain, bandpass filter: 0.02-1 Hz) of the Alaska Peninsula earthquake. For comparison, the east channel of CI-SRT (bandpass filter: 0.02-1 Hz) is overplotted in solid black line. The arrival time of P wave and S wave for SRT is marked in red line. Note the consistent waveform quality throughout all the channels. 122
Figure 4.7 State College FORESEE-urban DAS data (strain rate, bandpass filter: 0.02-1 Hz) of the Alaska Peninsula earthquake. Segment assignment of the whole array is laid out at the left side whose color is consistent with that in Figure 4.4. For comparison, the east channel of IU-SSPA (bandpass filter: 0.02-1 Hz) is overplotted in solid black line. The arrival time of P wave and S wave for SSPA is marked in red line. 123
Figure 4.8 Stacked DAS data of Enid and rotated horizontal component of broadband seismometer. a) Stacked DAS particle velocity waveform by segment (bandpass filter: 0.02- 1 Hz). b) Stacked DAS particle velocity waveform by segment (bandpass filter: 0.01- 0.1 Hz). c) Filtered DAS particle velocity (segment 3) and rotated horizontal component of OK-AMES (bandpass filter: 0.01-0.1 Hz). d) DAS particle velocity waveform of segment 3 with different bandpass filter. Frequency band is printed below each trace. 127
Figure 4.9 Stacked DAS data of FORESEE-urban array and rotated horizontal component of broadband seismometer. a) Stacked DAS particle velocity waveform by segment (bandpass filter: 0.01- 1 Hz). b) Stacked DAS particle velocity waveform by segment (bandpass filter: 0.01- 0.1 Hz). c) Filtered DAS particle velocity (segment 3) and rotated horizontal component of IU-SSPA (bandpass filter: 0.01-0.1 Hz). d) DAS particle velocity waveform of segment 3 with different bandpass filter. Frequency band is printed below each trace. 128

Figure 4.10 Stacked DAS data of Ridgecrest array and rotated horizontal component of broadband seismometer. a) Stacked DAS particle velocity waveform by segment (bandpass filter: 0.01- 1 Hz). b) Stacked DAS particle velocity waveform by segment (bandpass filter: 0.01- 0.1 Hz). c) Filtered DAS particle velocity (segment 3) and rotated horizontal component of CI-SRT (bandpass filter: 0.01-0.1 Hz). d) DAS particle velocity waveform of segment 3 with different bandpass filter. Frequency band is printed below each trace. 129

Figure 4.11 SNR of each segment of Enid (a, b), FORESEE (c, d), Ridgecrest (d, e) DAS array under body wave frequency band (0.02-1 Hz) and surface wave frequency band (0.01-0.1 Hz). 130

Figure 4.12 Spectrogram of a) Enid DAS data and b) broadband seismometer (AMES HHE) waveform. 132

Figure 4.13 Spectrogram of a) FORESEE-urban DAS data and b) broadband seismometer (SSPA BHE) waveform. 133

Figure 4.14 Spectrogram of a) Ridgecrest DAS data and b) broadband seismometer (SRT BHE) waveform. 134

Figure 4.15 Stacked subset DAS data and RFs derived from DAS and vertical channel of broadband station. a) Stacked DAS particle velocity of subset of Enid array segment 3. b) RFs derived from the DAS waveform in a) and vertical channel of OK-AMES. c) RFs from two broadband stations (OK-AMES & OK-CROK) and DAS RFs. Note the stacked RF traces from AMES and CROK are modified from (Wang et al., 2023). Coherent phases (red arrow: Moho conversion; blue arrow: basement reverberation) are marked by arrows. 137

Figure A 1 Number of events used in this study and for deriving the Moho map. a) the total number of events used in each station. b) number of prescreened events used in the H-k stacking and depth-conversion 158
Figure A 2 The Moho depth of each station obtained by H-kappa stacking. The result is shown in five intervals from 40 km to 55 km. Note the compelling scattering of results for nearby stations where the depth of Moho fluctuates dramatically in short distances. 162
Figure A 3 The Vp/Vs ratio of each station obtained from H-kappa stacking. The result is shown in five intervals from 1.6 to 1.9. Note the scattering of the Vp/Vs ratio is even more significant than the Moho depth result, where the crustal Vp/Vs ratio oscillates greatly across the study area. 163
Figure A 4 The semi-automatically picked Moho depth of each station. The result is shown in 11 intervals from 40 to 49. The color range corresponds to the same color range of interpolated Moho map (Figure 2.5). 167
Figure A 5 Uncertainty of individual stations for Moho map interpolation. Note the majority of stations have the error of Moho depth estimation of 1-4 km. 168

List of Tables

Table 3-1 Local and regional events information 82

Table A 1 Stations used in the study chapter 2 149

Table A 2 Teleseismic events information of receiver function analysis in chapter 2 153

Table A 3 Moho depth and Vp/Vs ratio of each station from H − κ stacking 158

Table A 4 Moho depth from converted RFs by semi-automatically picking 164

Acknowledgement

Throughout my PhD journey, which spanned five years, I have felt as though I embarked on an arduous and lengthy expedition from the very first day I became a doctoral student. Pursuing a PhD degree is widely recognized as a challenging endeavor, and my own journey was no exception, especially given the additional complexities posed by the COVID pandemic. Nevertheless, I take great pride in presenting this dissertation as the culmination of my PhD efforts, not only for my committee but also for all the individuals who love me, whom I cherish dearly, and, most importantly, for myself.

I am deeply grateful to my esteemed committee members, particularly Dr. Michael Behm and Dr. Xiaowei Chen, and Dr. Brett M. Carpenter who served as my advisors during the PhD program. Their invaluable guidance, both academically and personally, proved crucial in completing this dissertation and successfully finishing the program. Additionally, I extend my sincere appreciation to Dr. Patricia Persaud, an external committee member, whose unwavering support throughout my receiver function research journey has been truly memorable, including the enriching discussions we had during a week-long visit to LSU in the summer of 2019.

I would like to express my thanks to Dr. Zhongwen Zhan's group of Observational Seismology at Caltech and Dr. Tianyuan Zhu's Environmental Geophysics Group of Penn State for generously providing the DAS data.

To all the friends I met at the University of Oklahoma, thank you for the unforgettable moments we shared together. I am also deeply grateful for the overwhelming support from some of my personal friends, whom I've known since high school and college.

Last but not least, I extend my deepest gratitude to my parents and grandparents for their unwavering and unconditional support in every aspect of my life. Without their love and trust, I wouldn't have been able to study abroad and pursue this PhD journey. A special mention goes to my wife, Hanwen Yan, who married me during my first year of the PhD and has been by my side, offering her unwavering support throughout this entire journey. This dissertation is dedicated to them, and I hope it fills them with pride.

Abstract of the Dissertation

The advancement of seismic imaging methodologies is driven by the requirement to attain a more comprehensive and accurate understanding of the subsurface, which holds significant importance for natural resource exploration, geohazard mitigation, and the interest of humanity about the geological history of the Earth and its prospective evolution. While active seismic imaging is dominantly applied in the exploration industry, passive seismic imaging methods which extract the subsurface information from natural sources (e.g., earthquakes, ambient noise, microseismism) offer nondestructive, economical access to the subsurface structures. Receiver function (RF) is an established passive seismic imaging method which traditionally reveals the deep-earth structure from teleseismic recordings. The abundance of earthquake sources around the world and established processing workflow makes the RF a promising method in investigating the upper mantle and crustal structure.

Oklahoma, situated geologically in the middle of the North American plate, has garnered significant attention from both the general public and the geoscience community due to the notable increase in intraplate seismicity over the past decade. However, our understanding of the deep structure of the Oklahoma crust and mantle remains limited, despite having approximate crust thickness estimates from seismic investigations on a continental scale. I address the crustal and mantle structure of the Oklahoma lithosphere by conducting teleseismic RF analysis in central Oklahoma, utilizing data from 169 broadband and short-period seismometers deployed by various monitoring networks. By converting the stacked RFs into the depth domain, this study provides the first detailed Moho map of central Oklahoma. The results indicate an eastward shallowing Moho, transitioning from over 50 km in the northwest to approximately 40 km in the east.

Additionally, the RF depth cross-section reveals a mid-lithosphere discontinuity at a depth of 60-80 km within the upper mantle. Regarding the ongoing debate regarding the validation of midcontinent rift extension in Oklahoma over the gravity-anomalous zone, the RF analysis does not exhibit similar characteristics of crustal structure that are observed in the northern part of MCR, suggesting limited impact from the rifting processing within Oklahoma crust. However, the presence of intracrustal discontinuities observed in the RFs suggests the potential existence of rift-filling magmatism.

RFs derived from teleseismic events have limited capability in resolving shallow structures with high-resolution, primarily due to the absence of high-frequency components in teleseismic waveforms. Furthermore, deconvolution involving high-frequency component introduces instabilities to the inversion process and consequently less reliable RFs. To obtain high-resolution imaging of the shallow structures in the fault zone that ruptured the 2016 Mw 5.0 Cushing earthquake, I derived the RFs using local and regional earthquake data recorded by a nodal array comprising 130 portable seismic recording stations. A multichannel blind deconvolution approach is adopted to establish an inversion routine for retrieving high-resolution RF from local and regional earthquake data at a densely spaced array. The RFs clearly illustrate the primary conversion from the basement top interface, which cannot be observed from teleseismic RFs. The depth of this converted interface is approximately 1.15 km, which agrees well with an existing basement depth map.

Distributed Acoustic Sensing (DAS) from dark fiber introduces a new kind of data to the seismological community and holds great potential for earthquake detection applications. However, the earthquake wave responses of different DAS arrays may exhibit notable variations in signal to noise ratio and spectral sensitivity. These variations can be attributed to factors such

as deployment conditions, surrounding noise levels, and fiber geometry. I present a comparative analysis of the waveforms of 2016 Mw 8.2 Alaska Peninsula earthquake from three DAS arrays (Enid, Ridgecrest, FORESEE-urban in State College). For comparison, waveform from nearby broadband stations is reviewed along with the converted particle velocity waveform from DAS strain and strain rate data. The three DAS arrays present the capability in capturing low-frequency signals while the variations of SNR exhibit between DAS arrays and internal sections, respectively. RF obtained from the combined Enid DAS array and conventional seismic receiver array show comparable conversion phases to those obtained from a broadband station.

Chapter 1

1 Introduction

1.1 Introduction

The Earth, as the foundation of all human beings, holds numerous secrets within its vast interior. Despite the majority of human activities taking place on the surface, comprehending the Earth's subsurface holds significant meaning for our collective destiny. Geophysical imaging methods serve as the primary tools for investigating the Earth's interior, providing insights into its subsurface structure(Claerbout, 1985). Among these methods, seismic imaging plays a pivotal role, utilizing acoustic and elastic waves propagating through the Earth to decipher the heterogeneous subsurface space(Claerbout, 1985; Biondi, 2006; Stein and Wysession, 2009). Seismic imaging is widely applied across diverse fields including fossil energy exploration, investigations of deep structures and seismic studies related to earthquakes(Payton, 1977; Zhu and Kanamori, 2000; Etgen, Gray and Zhang, 2009; Grad and Tiira, 2009; Rawlinson, Pozgay and Fishwick, 2010).

One established technique in passive seismic imaging is receiver function analysis, which utilizes conversion waves generated from incident earthquake waves at impedance discontinuities to delineate subsurface boundaries(Stein and Wysession, 2009). The foundational development of receiver function is based on the studies of Langston in the 1970s (Langston and Helmberger, 1975; Langston, 1977a, 1977b, 1979), which synthesized the teleseismic P-wave spectral amplitude ratio of vertical displacement to radial displacement in the time domain, and developed

deconvolution techniques, laying the groundwork for the modern receiver function analysis. Subsequent advancements in the 1980s and 1990s expanded the methodology, incorporating waveform fitting, deconvolution methods, time-depth conversion, stacking and migration techniques (Owens, Zandt and Taylor, 1984; Ammon, Randall and Zandt, 1990; Ammon, 1991; Dueker and Sheehan, 1997; Yuan et al., 1997). With the increasing availability of teleseismic data due to regional and global broadband network deployments, receiver function analysis has become a prominent technique for studying lateral discontinuities in the crust and upper mantle. Over the past few decades, as seismometers worldwide have proliferated, receiver function studies have significantly contributed to the further understanding of crust and mantle structures, particularly at the Moho discontinuity and lithosphere-asthenosphere boundary (LAB), in subduction zones and for rifting process around the world (Zhu and Kanamori, 2000; Dugda, 2005; Nair et al., 2006; Kind, Yuan and Kumar, 2012a; Li, Gao and Wu, 2014; Shen and Ritzwoller, 2016a).

The early geological understanding of subsurface Oklahoma dates back to 1950s when the vast exploration for oil took place in the Anadarko Basin in western Oklahoma (Jacobsen, 1949; Wheeler, 1955; Beebe, 1959). The shallow subsurface geology of Oklahoma is dominated by the sedimentary layers deposited from Cambrian to Permian period with thickness of 1-3 km in the east and over 10 km in the Anadarko Basin to the west (W. Perry, 1989; Ball, Henry and Frezon Sherwood E., 1991; Crain and Chang, 2018). The defining of geologic provinces of Oklahoma are mainly shaped by the tectonic activities of Pennsylvanian age (Robert A. Northcutt and Campbell, 1996). Buried under the sedimentary rocks is the Pre-Cambrian crystalline basement, which is the southern part of the Southern Granite Rhyolite Province of North American craton (Bickford et al., 1981; Bickford, Van and Zietz, 1986a; Kolawole et al., 2019; Kolawole, Simpson Turko and Carpenter, 2020). The majority of Oklahoma's crust is formed at 1.35-1.48 Ga, during the south-

ward expansion of Laurentia, the early core of the North American craton (Bickford, Van and Zietz, 1986a; Whitmeyer and Karlstrom, 2007; Bickford et al., 2015; Wang and Behm, 2020).

Despite being located in a tectonically quiet zone within the middle of the North American continent, Oklahoma has experienced a significant increase in earthquakes over the past decades due to wastewater injection from hydrocarbon production, drawing considerable attention from academia and the general public (Ellsworth, 2013; Keranen et al., 2014). Consequently, numerous seismic networks have emerged in Oklahoma for earthquake monitoring following the concerns of raising earthquakes. Additionally, non-traditional sensors such as nodal arrays and Distributed Acoustic Sensing (DAS) have become available, contributing novel seismic datasets for receiver function analysis. The overall motivation of this dissertation is to employ receiver function analysis to gain insights into the multiscale structure of Oklahoma's subsurface, ranging from the upper mantle to the basin scale. Simultaneously, this dissertation aims to contribute and apply novel algorithms to non-traditional datasets to advance the receiver function technique. The specific motivations of each section are as follows: (1) providing insights into Moho depth and upper mantle structure through receiver function analysis using data from multiple networks in Oklahoma, (2) exploring the application of receiver function analysis using local earthquake data recorded by nodal arrays and obtaining high-resolution images of basement-top interfaces in fault zones, and (3) comparing teleseismic waveforms recorded by Distributed Acoustic Sensing arrays across the US.

1.2 P-to-S Receiver function

The receiver function provides insight about the structure beneath the receiver by isolating the structure response of earthquake wave from the source-time function and far-away-structure effect (Stein and Wysession, 2009). The basic aspect of the receiver function method is the wave mode conversion occurrence when a teleseismic wave incident to discontinuities as the wave propagates through the subsurface. Since the studies presented in this dissertation solely focus on the P-to-S receiver function, the following introduction will concentrate on the P-to-S receiver function method and its processing techniques.

In the P-to-S receiver function studies, the P wave of a teleseismic with event epicentral distance greater than 30° can be assumed as plane wave (Figure 1.1a). Part of the incident teleseismic P wave is converted to S wave (Ps) at impedance boundaries as it propagates upward from the mantle to the surface. The Ps wave arrives at the station within the P wave coda right after the direct P wave arrival. Then, the simplified relationship between the P wave and converted S wave is given as:

$$\text{Converted S} - \text{wave (t)} = \text{P} - \text{wave(t)} * \text{rf(t)}$$

where the rf(t) represents the time receiver function and $*$ represents convolution. This equation is based on a couple of assumptions 1) the source time function is approximated by the P-wave wavelet, and 2) the instrument response and noise are not considered in this ideal situation. So, the derivation of receiver function is the deconvolution of the P-wave from the converted S wave. Figure 1.1b presents a synthetic waveform of receiver function for a two-layer model where the impedance of bottom layer is larger than the top layer. The amplitude phases in the receiver function waveform are associated with the primary conversion or surface related multiples while

the time of the phases are related to the depth of the conversion interface, velocity model of the top layer, and the ray parameter to the teleseismic P wave (Zhu and Kanamori, 2000).

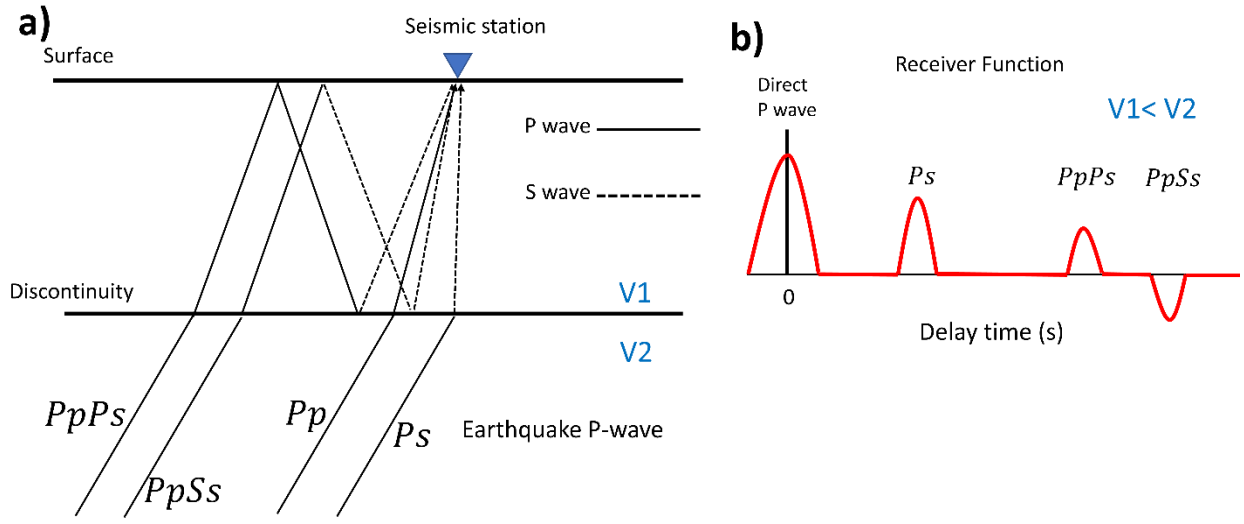


Figure 1.1 a) Diagram of the teleseismic P wave, converted S wave and multiples, and b) representation of receiver function waveform of the two-layer model depicted in a).

When deriving the receiver function from 3-component seismograms of teleseismic events, it is generally accepted to assume that the direct P wave is predominantly recorded by the vertical component, while the converted S wave is mainly captured by the two horizontal components. To obtain the converted SV and SH waves separately, a common practice is to rotate the EW and NS components to the radial and transverse components using the back azimuth of the teleseismic event with respect to the station. With a comprehensive understanding of the near-surface geology in the study area, more precise rotation can be performed for each wave component. By knowing the incident angle of the P wave arrival, the P-wave and converted SV wave can be effectively isolated through a rotation technique called LQT rotation. In LQT rotation, the L component aligns

with the direction of P wave propagation, the Q component aligns with the direction of SV phase movement, and the T component aligns with the direction of SH phase movement.

When it comes to deriving the receiver function from the rotated three-component seismograms of teleseismic events, the deconvolution process plays a vital role and involves several mathematical considerations. Three primary deconvolution methods are commonly employed in receiver function analysis: 1) water-level frequency domain deconvolution (Clayton and Wiggins, 1976a), 2) iterative time domain deconvolution (Ligorría and Ammon, 1999a), and 3) multiple-taper spectral deconvolution (Park and Levin, 2000). In recent years, statistics-based inversion methods have also been introduced to extract coherent conversion phases within the receiver function (Kolb and Leki, 2014; Zhong and Zhan, 2020). These methods offer alternative approaches for retrieving valuable information from the receiver function waveform.

1.3 Overview of the dissertation

Chapter 2 of my dissertation focuses on the application of receiver function analysis in Oklahoma using various locally deployed broadband and short-period stations. The goal is to gain insights into the crustal and upper mantle structure of the region. Previous seismological studies, such as those conducted by the USArray project, which deployed over 2000 seismometers across the United States following a rolling style, have provided an overview of crust thickness in the country, suggesting a Moho depth of around 45 km in Oklahoma (Kumar et al., 2012; Kind et al., 2015; Ma and Lowry, 2017). However, detailed imaging of the crust and mantle structure in Oklahoma has been limited. To address this, I utilized teleseismic data recorded by locally deployed

broadband and short-period networks in Oklahoma, which are rarely used for deep structure imaging. By analyzing receiver functions from 169 three-component seismometers across five networks, I generated a depth map of the Moho discontinuity. The results indicate an eastward shallowing of Moho, with the deepest part located in the northwest of Oklahoma at depths exceeding 50 km. The receiver function analysis also revealed the presence of a mid-lithosphere discontinuity, consistent with upper mantle discontinuity depths observed in continental-wide seismic studies. Furthermore, the results suggest no evidence of the Midcontinent Rift extension in Oklahoma, but the possibility of rift-filling magmatism.

In Chapter 3, I demonstrate the application of multichannel blind deconvolution to retrieve high-resolution receiver functions from local earthquake data recorded by a nodal array near the 2016 Mw 5.2 earthquake sequence at Cushing, Oklahoma. A nodal array consisting of 130 3-C Z Land node was deployed near the 2016 Mw 5.0 Earthquake sequence near Cushing, Oklahoma to characterize the fault where the earthquake sequence ruptured (Qin et al., 2022). Instead of teleseismic data, local earthquakes are used to derive high-resolution receiver functions. To ensure stability in deconvolution analysis of high-frequency local earthquake data, I adapted a multichannel blind deconvolution technique (Behm and Shekar, 2014) for RF analysis. The results provide a high-resolution receiver function that clearly delineates the conversion phase of the basement top interface. The depths map obtained from the receiver function analysis align remarkably well with the basement map from the Oklahoma Geological Survey. Across the array, the basement conversion phase does not exhibit evidence of vertical displacement from the fault, which is consistent with focal mechanism studies (Deng, Liu and Chen, 2020; Qin et al., 2022) indicating dominant strike-slip movement during the earthquake sequence.

Chapter 4 focuses on a comparison of the teleseismic response of a mega-earthquake recorded by three dark fiber Distributed Acoustic Sensing (DAS) arrays. DAS technology leverages optical fiber reflectometry, repurposing dark optical fibers (inactivated telecommunication fibers) as dense-spaced seismometers. I collected DAS data for the 2021 Alaska Peninsula Mw 8.2 earthquake from three DAS arrays: Ridgecrest DAS array, FORESEE-urban DAS array, and Enid DAS array. This study compares the waveforms in the time and frequency domains to assess data quality and spectral sensitivity, which revealed distinct signal-to-noise ratios among the arrays and their internal sections. Additionally, I performed receiver function analysis on the Enid DAS data for this earthquake, which demonstrated similar conversion phases as those observed from broadband station receiver functions.

1.4 Structure of the dissertation

This dissertation consists of 3 main chapters with the first main chapter reformatted from a published manuscript and the other two chapters in preparation for submission. The chapters are as follows:

Chapter 2: New Insights on Moho Depth and Regional Lithospheric Structure of Central Oklahoma Based on Receiver Function Analysis from Dense Seismic Networks.

Published: Wang, Zhuobo, Michael Behm, Patricia Persaud, Xiaowei Chen, and Brett M. Carpenter. "New insights on Moho depth and regional lithospheric structure of central Oklahoma based on receiver function analysis from dense seismic networks." Tectonophysics 854 (2023): 229818.

Chapter 3: High-resolution receiver function imaging using local earthquakes and multi-channel inversion routine.

In preparation for submission

Chapter 4: Investigation of the Teleseismic Event Record by Multiple Distributed Acoustic Sensing Arrays

In preparation for submission

1.5 References

Ammon, C. J. (1991). The isolation of receiver effects from teleseismic P waveforms. Bulletin of the Seismological Society of America, 81(6), 2504–2510. https://doi.org/10.1785/BSSA0810062504

Ammon, C. J., Randall, G. E., & Zandt, G. (1990). On the nonuniqueness of receiver function inversions. Journal of Geophysical Research, 95(B10), 15303. https://doi.org/10.1029/JB095iB10p15303

Ball, M. M., Henry, M. E., & Frezon Sherwood E. (1991). Petroleum geology of the Anadarko Basin region, province (115), Kansas, Oklahoma, and Texas.

Beebe, B. W. (1959). Characteristics of Mississippian Production in the Northwestern Anadarko Basin. Tulsa Geological Society Digest, 27, 190–205.

Behm, M., & Shekar, B. (2014). Blind deconvolution of multichannel recordings by linearized inversion in the spectral domain. GEOPHYSICS, 79(2), V33–V45. https://doi.org/10.1190/geo2013-0170.1

Bickford, M. E., HARROWER, K. L., HOPPE, W. J., NELSON, B. K., NUSBAUM, R. L., & THOMAS, J. J. (1981). Rb-Sr and U-Pb geochronology and distribution of rock types in the Precambrian basement of Missouri and Kansas. Geological Society of America Bulletin, 92(6), 323. https://doi.org/10.1130/0016-7606(1981)92<323:RAUGAD>2.0.CO;2

Bickford, M. E., Van Schmus, W. R., Karlstrom, K. E., Mueller, P. A., & Kamenov, G. D. (2015). Mesoproterozoic-trans-Laurentian magmatism: A synthesis of continent-wide age distributions, new SIMS U–Pb ages, zircon saturation temperatures, and Hf and Nd isotopic

compositions. Precambrian Research, 265, 286–312. https://doi.org/10.1016/j.precamres.2014.11.024

Bickford, M. E., Van, W. R., & Zietz, I. (1986). Proterozoic history of the midcontinent region of North America. Geology, 14(6), 492. https://doi.org/10.1130/0091-7613(1986)14<492:PHOTMR>2.0.CO;2

Biondi, B. (2006). 3D seismic imaging. Society of Exploration Geophysics.

Claerbout, J. F. (1985). Imaging the earth's interior. Oxford: Blackwell Scientific Publications, 1.

Clayton, R. W., & Wiggins, R. A. (1976). Source shape estimation and deconvolution of teleseismic bodywaves. Geophysical Journal International, 47(1), 151–177. https://doi.org/10.1111/j.1365-246X.1976.tb01267.x

Crain, K. D., & Chang, J. C. (2018). Elevation map of the top of the crystalline basement in Oklahoma and surrounding states. Oklahoma Geological Survey Open-File Report.

Deng, K., Liu, Y., & Chen, X. (2020). Correlation Between Poroelastic Stress Perturbation and Multidisposal Wells Induced Earthquake Sequence in Cushing, Oklahoma. Geophysical Research Letters, 47(20). https://doi.org/10.1029/2020GL089366

Dueker, K. G., & Sheehan, A. F. (1997). Mantle discontinuity structure from midpoint stacks of converted P to S waves across the Yellowstone hotspot track. Journal of Geophysical Research: Solid Earth, 102(B4), 8313–8327. https://doi.org/10.1029/96JB03857

Dugda, M. T. (2005). Crustal structure in Ethiopia and Kenya from receiver function analysis: Implications for rift development in eastern Africa. Journal of Geophysical Research, 110(B1), B01303. https://doi.org/10.1029/2004JB003065

Ellsworth, W. L. (2013). Injection-Induced Earthquakes. Science, 341(6142). https://doi.org/10.1126/science.1225942

Etgen, J., Gray, S. H., & Zhang, Y. (2009). An overview of depth imaging in exploration geophysics. GEOPHYSICS, 74(6), WCA5–WCA17. https://doi.org/10.1190/1.3223188

Grad, M., & Tiira, T. (2009). The Moho depth map of the European Plate. Geophysical Journal International, 176(1), 279–292. https://doi.org/10.1111/j.1365-246X.2008.03919.x

Jacobsen, L. (1949). Structural Relations on East Flank of Anadarko Basin, Cleveland and McClain Counties, Oklahoma. AAPG Bulletin, 33. https://doi.org/10.1306/3D933D55-16B1-11D7-8645000102C1865D

Keranen, K. M., Weingarten, M., Abers, G. A., Bekins, B. A., & Ge, S. (2014). Sharp increase in central Oklahoma seismicity since 2008 induced by massive wastewater injection. Science, 345(6195), 448–451. https://doi.org/10.1126/science.1255802

Kind, R., Yuan, X., & Kumar, P. (2012). Seismic receiver functions and the lithosphere–asthenosphere boundary. Tectonophysics, 536–537, 25–43. https://doi.org/10.1016/j.tecto.2012.03.005

Kind, R., Yuan, X., Mechie, J., & Sodoudi, F. (2015). Structure of the upper mantle in the north-western and central United States from USArray S-receiver functions. Solid Earth, 6(3), 957–970. https://doi.org/10.5194/se-6-957-2015

Kolawole, F., Johnston, C. S., Morgan, C. B., Chang, J. C., Marfurt, K. J., Lockner, D. A., Reches, Z., & Carpenter, B. M. (2019). The susceptibility of Oklahoma's basement to

seismic reactivation. Nature Geoscience, 12(10), 839–844. https://doi.org/10.1038/s41561-019-0440-5

Kolawole, F., Simpson Turko, M., & Carpenter, B. M. (2020). Basement-controlled deformation of sedimentary sequences, Anadarko Shelf, Oklahoma. Basin Research, 32(6), 1365–1387. https://doi.org/10.1111/bre.12433

Kolb, J. M., & Leki, V. (2014). Receiver function deconvolution using transdimensional hierarchical Bayesian inference. Geophysical Journal International, 197(3), 1719–1735. https://doi.org/10.1093/gji/ggu079

Kumar, P., Kind, R., Yuan, X., & Mechie, J. (2012). USArray Receiver Function Images of the Lithosphere-Asthenosphere Boundary. Seismological Research Letters, 83(3), 486–491. https://doi.org/10.1785/gssrl.83.3.486

Langston, C. A. (1977a). Corvallis, Oregon, crustal and upper mantle receiver structure from teleseismic P and S waves. Bulletin of the Seismological Society of America, 67(3), 713–724. https://doi.org/10.1785/BSSA0670030713

Langston, C. A. (1977b). The effect of planar dipping structure on source and receiver responses for constant ray parameter. Bulletin of the Seismological Society of America, 67(4), 1029–1050.

Langston, C. A. (1979). Structure under Mount Rainier, Washington, inferred from teleseismic body waves. Journal of Geophysical Research, 84(B9), 4749. https://doi.org/10.1029/JB084iB09p04749

Langston, C. A., & Helmberger, D. V. (1975). A Procedure for Modelling Shallow Dislocation Sources. Geophysical Journal International , 42(1), 117–130.

Li, Y., Gao, M., & Wu, Q. (2014). Crustal thickness map of the Chinese mainland from teleseismic receiver functions. Tectonophysics, 611, 51–60. https://doi.org/10.1016/j.tecto.2013.11.019

Ligorría, J. P., & Ammon, C. J. (1999). Iterative deconvolution and receiver-function estimation. Bulletin of the Seismological Society of America, 89(5), 1395–1400. https://doi.org/10.1785/BSSA0890051395

Ma, X., & Lowry, A. R. (2017). USArray Imaging of Continental Crust in the Conterminous United States. Tectonics, 36(12), 2882–2902. https://doi.org/10.1002/2017TC004540

Nair, S. K., Gao, S. S., Liu, K. H., & Silver, P. G. (2006). Southern African crustal evolution and composition: Constraints from receiver function studies. Journal of Geophysical Research: Solid Earth, 111(B2), n/a-n/a. https://doi.org/10.1029/2005JB003802

Northcutt, R. A., & Campbell, J. A. (1996). Geologic provinces of Oklahoma. In The Shale Shaker (Vol. 46, pp. 99–103). Oklahoma City Geological Society.

Owens, T. J., Zandt, G., & Taylor, S. R. (1984). Seismic evidence for an ancient rift beneath the Cumberland Plateau, Tennessee: A detailed analysis of broadband teleseismic P waveforms. Journal of Geophysical Research: Solid Earth, 89(B9), 7783–7795. https://doi.org/10.1029/JB089iB09p07783

Park, J., & Levin, V. (2000). Receiver Functions from Multiple-Taper Spectral Correlation Estimates. Bulletin of the Seismological Society of America, 90(6), 1507–1520. https://doi.org/10.1785/0119990122

Payton, C. E. (1977). Seismic Stratigraphy — Applications to Hydrocarbon Exploration. American Association of Petroleum Geologists. https://doi.org/10.1306/M26490

Perry, W. (1989). Tectonic evolution of the Anadarko Basin region, Oklahoma. Department of the Interior, US Geological Survey .

Qin, Y., Chen, X., Chen, T., & Abercrombie, R. E. (2022). Influence of Fault Architecture on Induced Earthquake Sequence Evolution Revealed by High-Resolution Focal Mechanism Solutions. Journal of Geophysical Research: Solid Earth, 127(11). https://doi.org/10.1029/2022JB025040

Rawlinson, N., Pozgay, S., & Fishwick, S. (2010). Seismic tomography: A window into deep Earth. Physics of the Earth and Planetary Interiors, 178(3–4), 101–135. https://doi.org/10.1016/j.pepi.2009.10.002

Shen, W., & Ritzwoller, M. H. (2016). Crustal and uppermost mantle structure beneath the United States. Journal of Geophysical Research: Solid Earth, 121(6), 4306–4342. https://doi.org/10.1002/2016JB012887

Stein, S., & Wysession, M. (2009). An introduction to seismology, earthquakes, and earth structure. John Wiley & Sons.

Wang, Z., & Behm, M. (2020). Receiver function analysis from a dense nodal array: Delineating shallow crustal structure from local and teleseismic receiver function analysis. AGU Fall Meeting Abstracts, 2020, S069-04.

Wheeler, R. R. (1955). Origin and Oil Possibilities of the Anadarko Basin. The Shale Shaker Digest I, I–V, 22–32.

Whitmeyer, S., & Karlstrom, K. (2007). Tectonic model for the Proterozoic growth of North America. Geosphere, 3(4), 220. https://doi.org/10.1130/GES00055.1

Yuan, X., Ni, J., Kind, R., Mechie, J., & Sandvol, E. (1997). Lithospheric and upper mantle structure of southern Tibet from a seismological passive source experiment. Journal of Geophysical Research: Solid Earth, 102(B12), 27491–27500. https://doi.org/10.1029/97JB02379

Zhong, M., & Zhan, Z. (2020). An array-based receiver function deconvolution method: methodology and application. Geophysical Journal International, 222(1), 1–14. https://doi.org/10.1093/gji/ggaa113

Zhu, L., & Kanamori, H. (2000). Moho depth variation in southern California from teleseismic receiver functions. Journal of Geophysical Research: Solid Earth, 105(B2), 2969–2980. https://doi.org/10.1029/1999JB900322

Chapter 2

2 New Insights on Moho Depth and Regional Lithospheric Structure of Central Oklahoma Based on Receiver Function Analysis from Dense Seismic Networks

2.1 Abstract

Knowledge of the midcontinent crustal structure of North America is crucial for understanding the evolutionary history of the ancient North American craton as Laurentia grew through accretion ~1.5 Ga to 1 Ga. Although Oklahoma has been recognized as a tectonically stable region since the Phanerozoic, its crustal structure records the earlier formation of the Mazatzal and southern Granite-Rhyolite provinces 1.6 Ga to 1.4 Ga. We present results from teleseismic receiver function analysis applied to 221 events recorded on 169 broadband stations in central Oklahoma. Our findings include a Moho depth map of central Oklahoma based on stacked and depth-converted teleseismic P receiver functions. The results are interpreted together with gravimetric and magnetic datasets and a recently established seismic velocity model of the crust.

The Moho map shows a generally flat crust-mantle boundary in central Oklahoma with an average depth of 43.5 km while we observe a sudden thickening on the crust of the northwestern part of

Oklahoma where the Moho deepens to over 50 km depth. We also find a Mid-lithosphere discontinuity at the upper-most mantle in north-central Oklahoma, presented as a negative phase deepening southeastward from 60 km to 80 km. We further observe an intracrustal discontinuity at the Nemaha uplift and Anadarko shelf regions in a depth range of 17-30 km. The hypothesis of the Mid-continent Rift (MCR) extending into Oklahoma is examined in terms of the crustal structure and Moho depth variation revealed by receiver functions. We do not find evidence of Moho structure or lower-crustal underplay characteristics similar to what has been discovered in the northern part of MCR, but the intracrustal discontinuity that deepens towards the hypothesized MCR region suggests upper-crustal volcanics potentially caused by the extended expansion regime of the failed rift near the south-most termination.

2.2 Introduction

The current understanding of the lithospheric structure in the US midcontinent (Figure 2.1) is largely based on gravity and magnetic data as well as on the geochemical analysis of basement rock samples where they are accessible through drilling or outcrops. The analysis from different data sources provides some understanding of the formation of the Oklahoma crust, although different lines of interpretation are presented in the literature (Bickford, Van and Zietz, 1986b; Rivers, 1997; Rivers and Corrigan, 2000; Karlstrom et al., 2001; Slagstad et al., 2009; Bickford et al., 2015; Cawood and Pisarevsky, 2017).

Based on isotopic studies, the southwest-northeast trending ‘Nd line’ runs across the SGRP (Southern Granite-Rhyolite Province) and EGRP (Eastern Granite-Rhyolite Province), separating craton lithosphere in the northwest having formed before 1.55 Ga from more juvenile crust in the

southeast (Bickford et al., 1981, 2015; Nelson and DePaolo, 1985; van Schmus, Bickford and Turek, 1996; Renee Rohs and van Schmus, 2007). The tectonic setting of this Paleoproterozoic-to-Mesoproterozoic transition zone and formation mechanisms of the Granite-Rhyolite provinces are explained in the literature through both 'orogenic' and 'anorogenic' processes (Anderson, 1999; Anderson & Bender, 1989a; Anderson & Morrison, 1992, 2005; Karlstrom et al., 2001; Karlstrom & Humphreys, 1998; Menuge et al., 2002; Rivers, 1997; Slagstad et al., 2009; Whitmeyer & Karlstrom, 2007). Early studies favored the hypothesis of 'granitoidic' emplacement in a compressive or transgressive regime for the formation of the Granite-Rhyolite province (Bickford and Lewis, 1979; Bickford et al., 1981; Bickford, Van and Zietz, 1986a; Nyman et al., 1994). However, contrasting hypotheses are derived from recent studies. Isotopic studies of'A-type' plutons, which are usually considered 'anorogenic' due to less foliation, indicate an older crust of craton origin (Anderson and Bender, 1989a; Anderson and Morrison, 1992; Anderson, 1999; Goodge and Vervoort, 2006; Whitmeyer and Karlstrom, 2007). More recent studies suggest an intracratonic setting, in which magmatism occurred in a back-arc setting associated with the early phase of the Grenville orogeny (Karlstrom et al., 2001; Menuge, Brewer and Seeger, 2002; Slagstad et al., 2009).

Another discussion revolves around the southern extension of the Mesoproterozoic Midcontinent Rift (MCR) western arm into Oklahoma (Schmus and Hinze, 1985; Woelk and Hinze, 1991a; Stein et al., 2014, 2015; Elling et al., 2020; Hinze and Chandler, 2020; Ratre and Behm, 2021). A widely accepted configuration includes its west branch stretching from the center of Lake Superior into southwest Kansas (Schmus and Hinze, 1985; Ruppel, 1995; Ojakangas, Morey and Green, 2001; Elling et al., 2020). Based on a linear gravity anomaly trending from Kansas to Oklahoma and isotopic analysis of diffuse volcanism, several authors propose an extension of the MCR into north-

central Oklahoma (Adams and Keller, 1994; S. Stein et al., 2018; Elling et al., 2020). Although the gravity map of Oklahoma and the surrounding regions (Figure 2.1) is indicative of lateral crustal variations at regional scales, the extension is still under debate due to a lack of validation from other data sets (Woelk and Hinze, 1991a; Hinze and Chandler, 2020; Ratre and Behm, 2021).

Another notable lithospheric structure of the midcontinent is the upper mantle negative velocity gradient which is frequently observed in seismological studies across the United States (Abt et al., 2010; Yuan and Romanowicz, 2010; Kind, Yuan and Kumar, 2012b; Lekić and Fischer, 2014a; Hansen, Dueker and Schmandt, 2015; Hopper and Fischer, 2015a; Kind et al., 2015; Chen et al., 2018). Although a negative velocity gradient is well resolved in many receiver function studies (Yuan and Romanowicz, 2010; Kind, Yuan and Kumar, 2012b; Lekić and Fischer, 2014a; Hansen, Dueker and Schmandt, 2015; Kind et al., 2015; Chen et al., 2018), the relation of the negative velocity gradient to a shallow lithosphere-asthenosphere boundary (LAB) or other mid-lithospheric discontinuities is uncertain (Yuan and Romanowicz, 2010). Only a few studies present the upper mantle structure of the Oklahoma lithosphere with the negative velocity gradient revealed, and continental scale lithospheric structure studies often lack detailed investigation of the mid-to-mideast continent (Yuan and Romanowicz, 2010; Kind, Yuan and Kumar, 2012b; Lekić and Fischer, 2014a; Hopper and Fischer, 2015a).

Overall, detailed regional knowledge about deeper subsurface structures is still sparse for this part of the midcontinent, owing to a lack of dedicated deep-sounding active and passive source seismic experiments when compared to other parts of North America. A detailed Moho depth map and insight on other lithospheric features can therefore contribute to the understanding of the GRP and the Paleoproterozoic-Mesoproterozoic transition zone. Additionally, imaging of the Moho and crust may help to resolve the question of the possible MCR extension into northern Oklahoma.

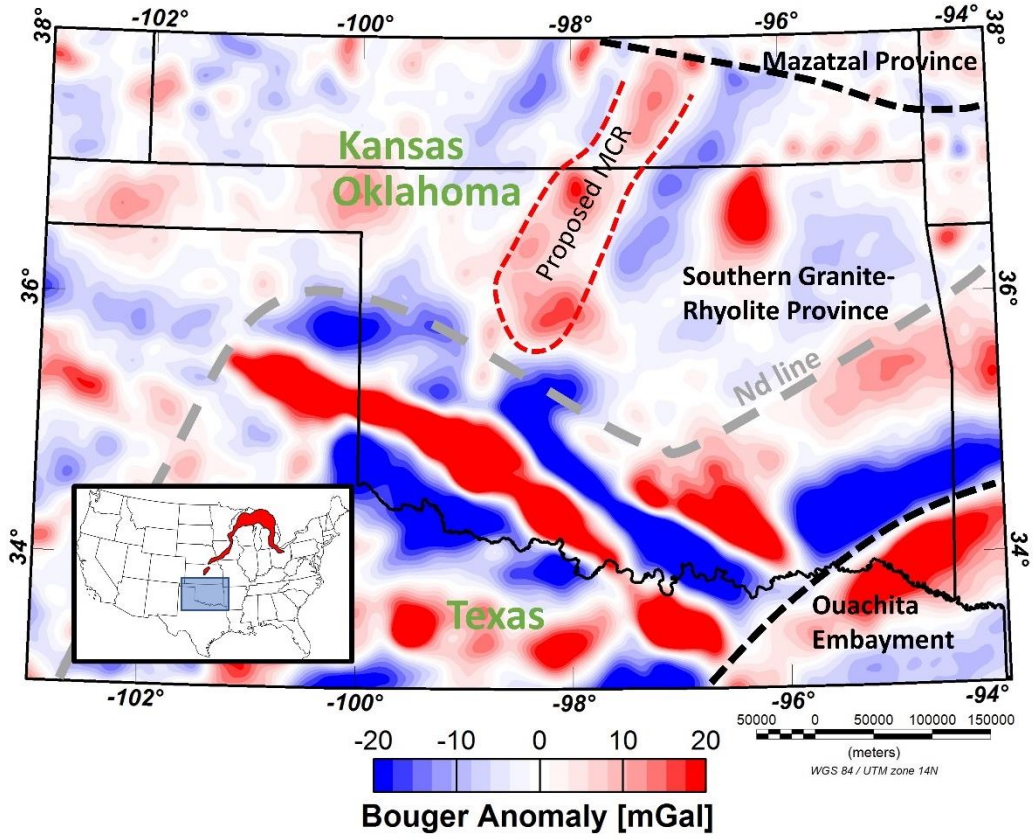


Figure 2.1 Bouguer gravity anomaly map of the study area and its surroundings (Gravity anomaly map of North America [Map], 1988). Tectonic provinces are defined by black dashed lines (Modified from Bickford et al., 2015). The southern extension of the western arm of MCR as proposed by (Adams and Keller, 1996; Stein et al., 2014) is indicated by the red dashed line. The gray dashed line is the Nd line. A high-pass wavelength filter (200 km) is applied to the gravity data to suppress upper mantle features.

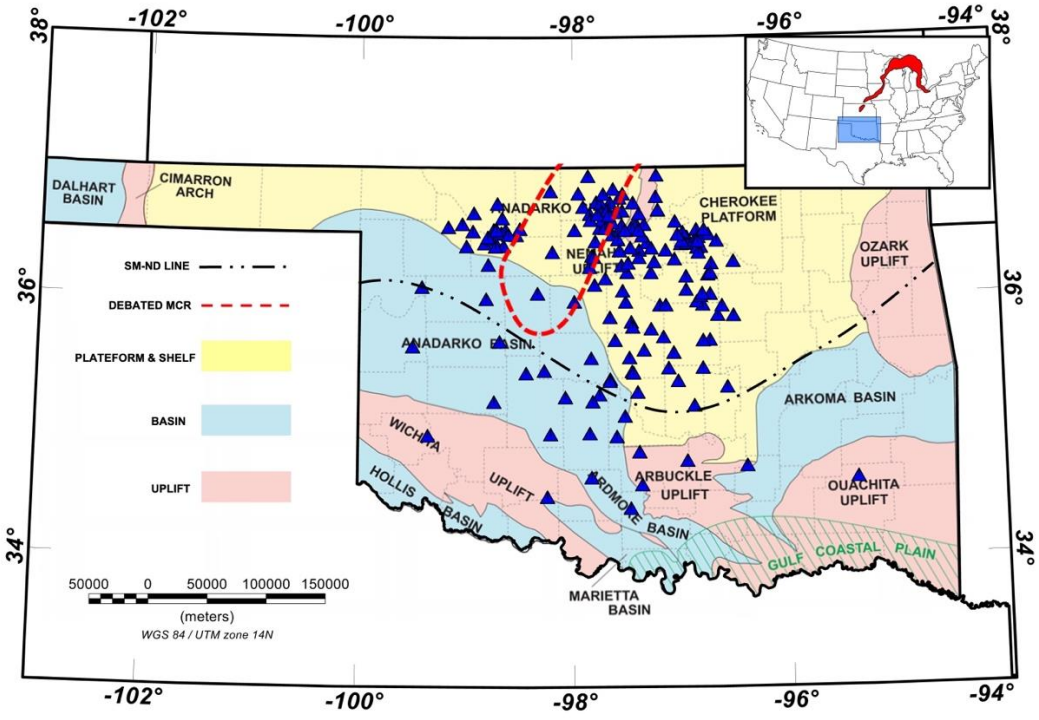


Figure 2.2 Main geologic provinces and major faults in Oklahoma (Oklahoma Geological Provinces [Map] by Oklahoma Geological Survey). Blue triangles show the seismic stations used in this study. Geological features (platform and shelf, basin, and uplift) are shown in different colors.

Seismic investigations at Oklahoma provide crustal structure delineations and rough estimation of Moho depth through various approaches starting in the late 1960s. Early active source seismic studies of the crustal structure beneath Oklahoma using 2D refraction data (Tryggvason and Qualls, 1967; Mitchell and Landisman, 1970) produced a model with a 46 km-deep Moho and an intracrustal layer at around 18 km depth. Following those early seismic models of central Oklahoma, more studies focused on developing velocity models for the Anadarko Basin and Wichita Uplift area (Brewer et al., 1983; Brewer & Oliver, 1980; X. Zhu & McMechan, 1989),

where the Moho depth ranges from 40 to 45 km (Lynn, Hale and Thompson, 1981; Pratt and Haus, 1992). Studies based on passive seismic methods (Toth, 2014; Chen, 2016) provide the seismic velocity of the upper crust through earthquake tomography, while the lower crust and Moho topography of Oklahoma was mainly investigated by receiver functions using US Transportable Array (TA) data (Tave, 2013; McGlannan and Gilbert, 2016). Taking advantage of the broad coverage with equally spaced stations, McGlannan and Gilbert (2016) reported a Moho topography map of the midcontinent, part of which suggests a 30-55 km Moho depth beneath Oklahoma. Integrating Pn tomography with receiver functions, Tave (2013) provided a Moho depth map for Oklahoma, with Moho depth varying from 36 km to 42 km. However, the large station spacing of the USArray does not allow for detailed information on local Moho depth variation or the potential existence of other lithospheric discontinuities. As a result of wastewater injection, intraplate seismicity has increased dramatically since 2009 (Ellsworth, 2013; Keranen et al., 2014). Consequently, a multitude of dense local seismic deployments was initiated to monitor local seismic activity, and most of these data are publicly available through the IRIS DMC (Figure 2.2). Those networks are usually equipped with broadband or short-period instruments and operate on time frames between months and years. Therefore, they are well-suited for recording teleseismic events for receiver function studies.

In our study, we utilize a large data set of teleseismic events from 2013 to 2019 recorded at 163 stations (Figure 2.2) to investigate the lithospheric structure and the Moho depth in Central Oklahoma. We apply P-to-S receiver function analysis to the prescreened teleseismic event data to estimate the crustal thickness and other lithospheric features in Oklahoma. We interpret our results in the context of the Proterozoic evolution of the mid-continent and the hypothesis of MCR extension into Oklahoma. Our work further complements a recently derived 3D crustal P-wave

velocity model (Ratre and Behm, 2021), which also made use of the abundant data recorded on the local networks, and it overall contributes to the understanding of continental evolution in this underexplored part of the North American lithosphere. We present a Moho depth map, identify mid-lithospheric discontinuities and interpret our results together with other relevant geophysical data such as gravity and magnetic anomalies.

2.3 Geologic and Tectonic Setting

The formation of the North American continental crust resulted from episodic accretions of igneous material to Laurentia starting at 1.8 Ga (Whitmeyer and Karlstrom, 2007). The growth of Laurentia at its southeastern margin involved a series of orogenic episodes (Yavapai orogeny, Mazatzal orogeny, Grenville orogeny), which formed the crust of the southeastern half of the core of Laurentia (Bickford et al., 2015; Bright et al., 2014; Whitmeyer and Karlstrom, 2007). The oldest crust of Oklahoma originates from the Mazatzal Orogeny ca. 1.65-1.6 Ga (Anderson & Bender, 1989; Whitmeyer & Karlstrom, 2007; Figure 2.1). The accretionary felsic magmatism (1.5-1.35 Ga) following the Mazatzal Orogeny constituted the Eastern and Southern Granite-Rhyolite Province, constituting most of the basement from northwestern Ohio to Texas (Bickford et al., 2015). The subsequent craton growth began with a major continental event, the Grenville orogeny (1.3-1.0 Ga), along the southeastern margin of Laurentia and led to the final assembly of the supercontinent Rodinia.

Sm-Nd isotopic studies of the basement rocks of the midcontinent provide an estimate of the crystallization time of the Mazatzal and GRP province lithosphere (Bickford et al., 1981, 2015; Nelson and DePaolo, 1985; van Schmus, Bickford and Turek, 1996; Renee Rohs and van Schmus,

2007). Delineated by samples older or younger in age than 1.55 Ga, the Nd-line represents a crustal boundary, separating the midcontinental crust into a Paleoproterozoic craton to the northwest of the line and juvenile Mesoproterozoic crustal accretion to the southeast of the line(Bickford et al., 2015). Inferred from the spatial and temporal distribution of the Nd model samples within GRP, the sharpness of the Nd line that represents a Paleo-Mesoproterozoic boundary is questionable, and suggests a more gradual transition from a 'cratonal' magmatic source to a more juvenile source (Bickford et al., 2015). The Nd line cuts across the Oklahoma crust from the east end of Wichita Uplift, along the Southern Oklahoma Aulacogen, to central Oklahoma, and bends towards the northeast to the Ozark Uplift, but there are no exposed tectonic structures at the surface that are associated with this crustal boundary. The midcontinent rift (MCR) records a major rifting event during the Grenville orogeny at ca. 1.1 Ga (C. A. Stein et al., 2018). As the rifting did not split Laurentia, it left a 3000-km-long U shape band of buried igneous and sedimentary rocks throughout the present US midcontinent. The MCR was initially identified as a midcontinent geophysical anomaly in the 1940s (Woollard, 1943). Following the compilation of more gravity data from the 1950s onward (Lyons, 1950; Black, 1955; Thiel, 1956; Craddock, Thiel and Gross, 1963), the MCR main body was established with two arms. The western arm extends from the western end of Lake Superior to Kansas, and the eastern arm extends from Lake Superior, across Michigan and Ohio, to Tennessee. Some studies proposed a southern extension of the western arm to Oklahoma based on an observed southward-extending linear gravity anomaly (Adams and Keller, 1994; Stein et al., 2014, 2015), but recently developed seismic velocity models (Ratre and Behm, 2021) do not give support for this hypothesis.

With the Proterozoic orogenic structure buried deep in the lower crust and lithosphere, the surface geological provinces of Oklahoma are predominantly shaped by early Phanerozoic tectonism. The

final stage (0.54-0.53 Ga) of the intermittent breakup of Rodinia involved the rifting of southeastern Laurentia, leaving a failed arm of a triple junction that forms the Southern Oklahoma Aulacogen (SOA) (W. J. Perry, 1989). Late Paleozoic extension and magmatism within the SOA ended with thermal subsidence and sediment loading, resulting in the formation of the Anadarko Basin (Brewer et al., 1983). The Ancestral Rockies Orogeny, with intense deformation and erosion during the Pennsylvanian, configured most of the present-day tectonic features of Oklahoma, including the Arbuckle-Wichita-Amarillo uplift belt (Burke, 1977). At the surface, prominent tectonic structures appear at different scales. Among them are the Ouachita, Arbuckle, and Wichita uplifts in the south and the Nemaha uplift in the north (Figure 2.1). Major sedimentary basins such as the Anadarko Basin and Arkoma Basin are located in the south as well. The Anadarko Shelf and Cherokee Platform are the units adjacent to the Anadarko Basin in the north (Robert A Northcutt and Campbell, 1996; Bright et al., 2014).

2.4 Data and Methods

We use data collected from five temporary networks deployed with 169 three-component broadband stations in total: 26 stations from US Geological Survey Networks (GS), 28 stations from the Nanometric Research Network (NX), 56 stations from Oklahoma Consolidated Temporary Seismic Networks (O2), 23 stations from the Oklahoma Seismic Network (OK), and 37 stations from XR network which was temporarily deployed for the Nemaha fault study (Figure 2.2, Appendix A1). The stations are irregularly distributed due to their emphasis on induced seismicity monitoring and other regional studies but cover many of the geologic provinces of central to central-west Oklahoma. Notable exceptions include parts of eastern Oklahoma, such as the Ozark Uplift, the Arkoma Basin, and the Ouachita Uplift. We use FuncLab (Porritt and Miller,

2018), a MATLAB-based receiver function (RF) analysis platform, to perform the pre-processing and calculation of the RFs. As the selected networks were mainly deployed after the onset of induced earthquake activity in the early 2010s (Keranen et al., 2014; Shah & Keller, 2017), the teleseismic data comprise events from June 2013 to August 2019 (Appendix A1). The networks were active for durations lasting from 14 months to 36 months. The data were accessed through the publicly available database of the Incorporated Research Institute for Seismology (IRIS) Data Services. In this study, events with 30° to 90° epicentral distance and moment magnitude (Mw) >5.5 are considered for analysis. A total of 221 events are used for RF computation while most events within the epicentral distance range are located in the Aleutian Trench and Peru-Chile Trench (Figure 2.3).

A bandpass filter of 0.05-1 Hz is applied to the rotated components before deconvolution. Then, the receiver functions are computed using time-domain iterative deconvolution applied to the vertical and radial components (Ligorría and Ammon, 1999b). A low-pass Gaussian filter with parameter 'a' of 2.5, which corresponds to a maximum frequency of ~1.2 Hz, is applied to the receiver functions to eliminate high-frequency noise. A low-velocity sedimentary layer can give rise to strong reverberations and primary conversion amplitude in the seismograms. Common characteristics of the reverberation phase in RF waveforms are delayed P arrival peaks and multiples, which may mask later crustal conversion phases as well as Moho phases depending on the depth of the basement. The sedimentary column in Oklahoma features an average thickness of 1 km on the shelf and platform and over 3 km in deeper basins (Campbell and Weber, 2006). In our dataset, reverberation characteristics are present in many RF waveforms and, in particular, from stations that are located in or close to the Anadarko Basin, where the sedimentary column is significantly thicker than other geological regions. To eliminate the reverberation phase from the

receiver function waveform, we apply a frequency-domain resonance removal filter to individual RF traces (Yu et al., 2015). For quality control, all RF traces with resonance removal filter applied are prescreened for clear and coherent phases corresponding to the P arrival and Moho primary conversion (Figure A1).

To investigate the Moho depth, we implement two distinct approaches: the first approach involves performing depth conversion of prescreened RFs, while the second approach utilizes $H-\kappa$ stacking (Zhu and Kanamori, 2000). In the first approach, the individual receiver functions are move-out corrected according to their event-station epicentral distance and stacked to obtain one representative trace for each station. Those traces then are depth-converted using a recently established Oklahoma crustal P-wave velocity model which was derived from local earthquake tomography at Oklahoma networks (Ratre and Behm, 2021). The time-depth conversion is based on an average 1-D velocity model extracted from the tomography-derived velocity volume. The depth-converted stacked traces form the basis for our structural interpretation. As an additional approach, $H-\kappa$ stacking is applied(Zhu and Kanamori, 2000) to investigate the crustal V_p/V_sratio (κ) and Moho thickness. Through the weighted stacking of the P-to-S Moho conversion phase (Pms) and its multiples in the crustal thickness (H) and V_p/V_sratio (κ) domain, the optimal values of crustal thickness and κ for each station are found by grid-searching the maximum of the stacking amplitude. The results of both approaches are described and discussed in the following sections.

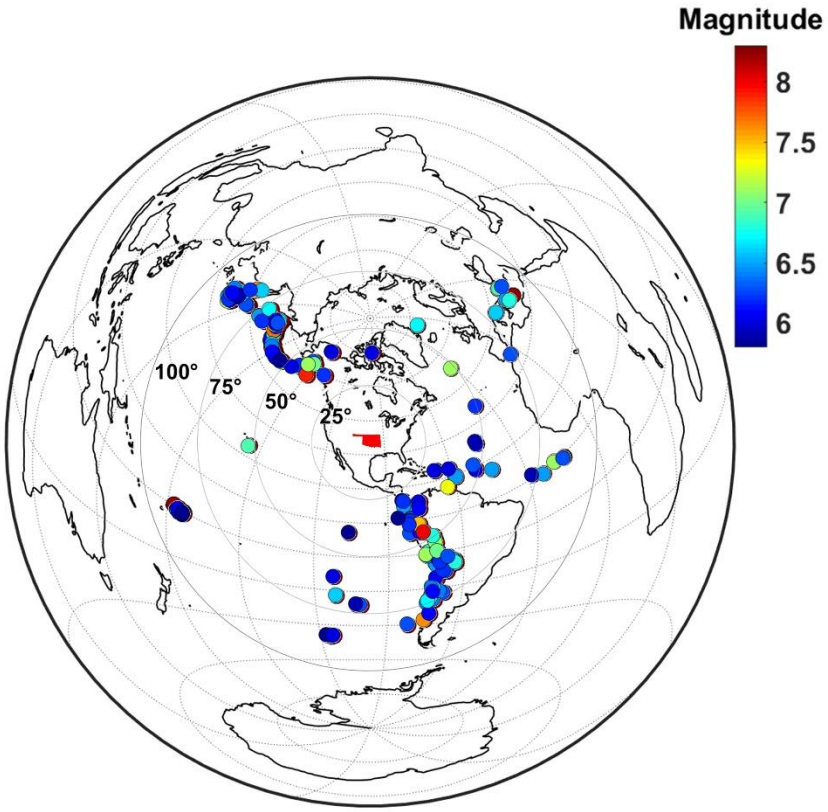


Figure 2.3 The distribution of teleseismic events used in the receiver function analysis. The state of Oklahoma is shown in red in the center of the map. Event magnitudes are indicated with different colors.

2.5 Results

In this study, we mainly focus on the Pms and other prominent conversion phases from the crust and upper mantle. To facilitate the interpretation of coherent phases with confidence, a general practice of receiver function analysis is the common conversion point stack (Frassetto et al., 2011a; Lekić and Fischer, 2014b; Hopper and Fischer, 2015b; Chen et al., 2018) which benefits from regular station spacing and homogenous coverage. Due to the scattered deployment in both space and time and poor back azimuth coverage (Figure 2.3), we instead stack the RFs at each station after move-out correction and assign this stacked RF trace to the station location.

2.5.1 Stacked RF

The stacked RFs show different characteristics across the various geologic provinces in Oklahoma. Due to the irregular distribution of the stations, we firstly present the stacked RFs classified into five groups based on their geographic location as well as on the characteristics of the waveforms (Figure 2.4). Those five subsets are associated with the following geological provinces: (1) The Anadarko shelf, (2) the Northern Cherokee Platform, (3) the Nemaha uplift, (4) the Southern Cherokee Platform, and (5) the Anadarko Basin. Within each region, we show stacked receiver functions arranged equidistantly along the W-E or S-N directions.

The most notable phase throughout the study area is a positive amplitude phase between 5 to 6 s (Figure 2.4), corresponding to the Moho discontinuity (Pms phase). Those delay times represent a Moho depth ranging between 40 and 50 km and correspond to results from previous seismological studies of the midcontinent crust. A clear interpretation of the Pms phase among the stations in the Anadarko Basin (Figure 2.4d) is not possible due to complex waveforms and sparse station coverage. Considering the presence of the thick, low-velocity sedimentary units in the basin, the coherent phases in this region are inferred to be basement reverberations that mask the mid-crustal and Moho conversions and, consequently, complicate the identification of the Pms and later phases. A variation of the Pms amplitude is also observable across other geologic provinces. Low amplitude Pms occurs at the stations located in the Anadarko Shelf, in the western part of the Nemaha Uplift, and in the northern part of the Southern Cherokee Platform, which may indicate a decreased velocity contrast across the Moho discontinuity and/or a high-velocity lower crust (Cassidy, 1992; Frassetto et al., 2011b; Janiszewski and Abers, 2015; Ratre and Behm, 2021).

Other crustal and lithospheric conversion phases are present in our study area as a positive phase at 2 – 4 s, and a negative phase at 8 – 11 s (Figure 2.4). The intracrustal conversion phase is mainly present at the Nemaha Uplift region and Northern Cherokee Platform, indicating a layer potentially caused by velocity or density variation in the mid-crust. Many studies of the mid-continent crust suggest the presence of an intracrustal layer, most of which are associated with inter-terrane deformation and detachment resulting from continental collision (Rivers, 1997; Elling et al., 2020). As the formation of SGRP does not involve an extensive continental collision, we also interpret the intracrustal layer as an indication of inner-terrane deformation. A potential explanation of the intracrustal layer is the intrusive magmatism that is associated with the MCR, which will be further discussed below. We also observe a negative-amplitude phase with varying delay times across the study area which corresponds to a negative velocity gradient (NVG). The coherent NVG is mainly observed in the northern part of the study area with delay times ranging from 8 to 9 s at the Anadarko Shelf and 7 to 11 s at the Nemaha Uplift and Northern Cherokee Platform regions, while an apparent eastward deepening occurs in the Nemaha Uplift region (Figure 2.4a, b, c).

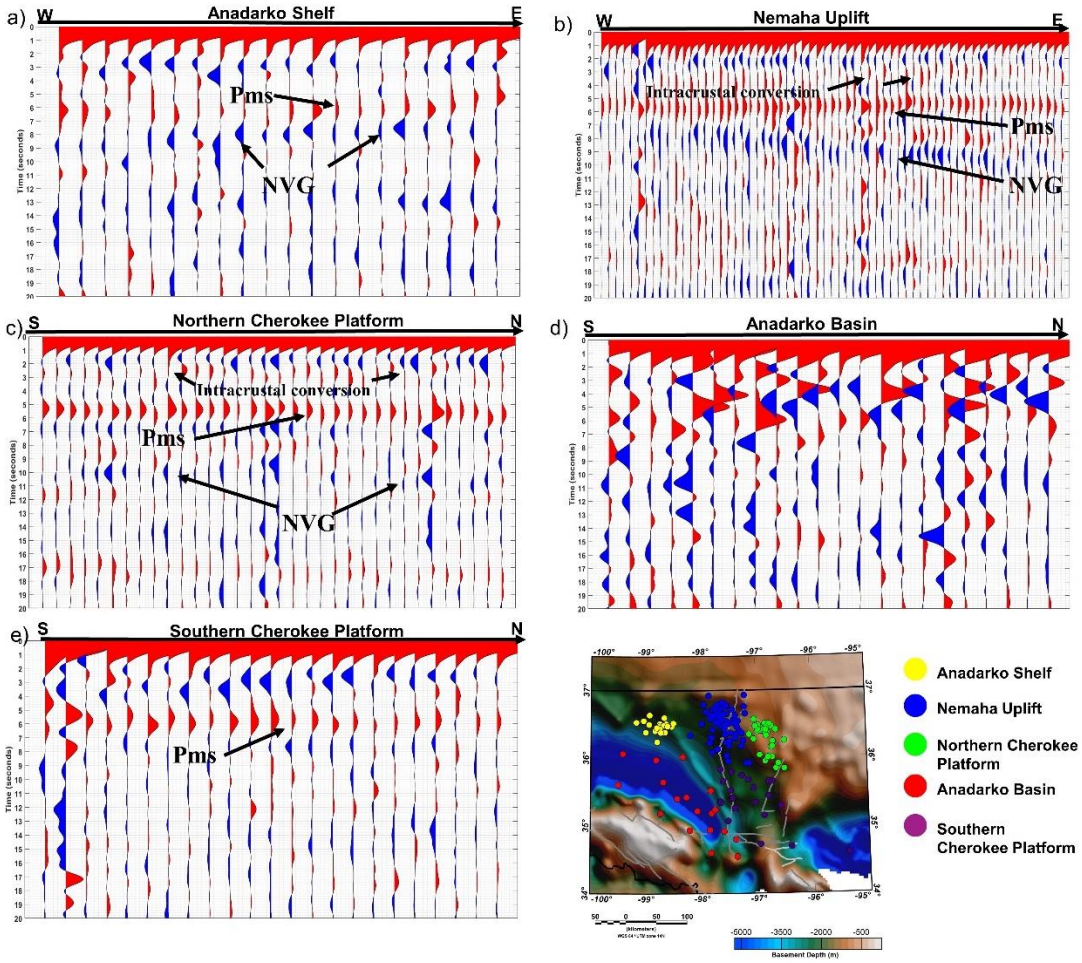


Figure 2.4 Stacked RF traces for each station grouped by geological provinces and waveform characteristics. a) The Anadarko shelf, b) the Nemaha uplift, c) the Northern Cherokee Platform, d) the Anadarko Basin, and e) the Southern Cherokee Platform. The RF traces are plotted by station longitude at the Anadarko shelf and the Nemaha uplift region and by station latitude at the Northern Cherokee Platform, the Southern Cherokee Platform, and the Anadarko Basin. Interpreted intracrustal layer, P-to-S conversion of Moho, and negative velocity gradient (NVG) are marked. The stations of each subset are shown with different colors on top of the basement depth map of the study area (Campbell and Weber, 2006).

2.5.2 Moho Depth Map

$H-\kappa$ stacking of RF amplitudes has been used routinely for estimating the crustal V_p/V_s ratio and Moho depth (Zhu and Kanamori, 2000; Persaud, Pérez-Campos and Clayton, 2007; Zhang et al., 2016). Its suitability and stability vary from case to case due to different data and geologic conditions (McGlannan and Gilbert, 2016; Zhang et al., 2016; Ogden et al., 2019; Wang, Persaud and Behm, 2019; Wang, Behm and Chen, 2021). As our data are derived from different networks with different deployment periods, the number of high-quality events used for receiver function analysis for each station varies substantially throughout the study area (Appendix A2). Although the $H-\kappa$ stacks themselves are mostly distinct and of relatively high quality, the obtained Moho depths and V_p/V_s ratios scatter significantly among neighboring stations (Appendix A2, Figure A2 & A3: Moho depths at stations, and V_p/V_s ratio from $H-\kappa$ stacking). Therefore, we chose a different approach to create a Moho depth map. We determine depths at station locations from depth-converted individual RFs by taking advantage of a recently developed 3D P-wave velocity model (Ratre and Behm, 2021) and using an average V_p/V_s ratio (1.830 ± 0.134) obtained from $H-\kappa$ stacking. As the 3D velocity model shows little lateral variation and considerable differences in depth coverage, we use a 1D velocity-depth function derived from averaging the whole 3D velocity model for all RFs. Due to the irregular station coverage, we prefer this simple and robust depth conversion over a move-out correction approach. Given the lack of pronounced lateral crustal variation (Ratre and Behm, 2021) as well as the overall flat appearance of the Moho as indicated in our RF results (Figure 2.5), we would expect no significant change in Moho depth if migration is applied.

Moho depths are picked semi-automatically at the maximum amplitude of the Pms phase on all individual depth-converted RFs (Appendix A2, Figure A4). We only pick the Pms phase where it is clearly pronounced and where it appears laterally consistent among adjacent stations. For that reason, we lack coverage in large parts of the Anadarko basin (compared with Figure 2.4d). The Moho depth beneath each station is represented by averaging all depth picks at each station. This procedure also allows estimating a relative uncertainty expressed as the standard deviation of the picked depths at each station. The average standard deviation amounts to 2.6 km, and the individual station values are shown in the appendices (Appendix A3, Figure A5). The final Moho depth map is then determined by interpolating the average depths at each station and subsequent smoothing with a Gaussian filter (Figure 2.5). The size of the smoothing filter is 50 km.

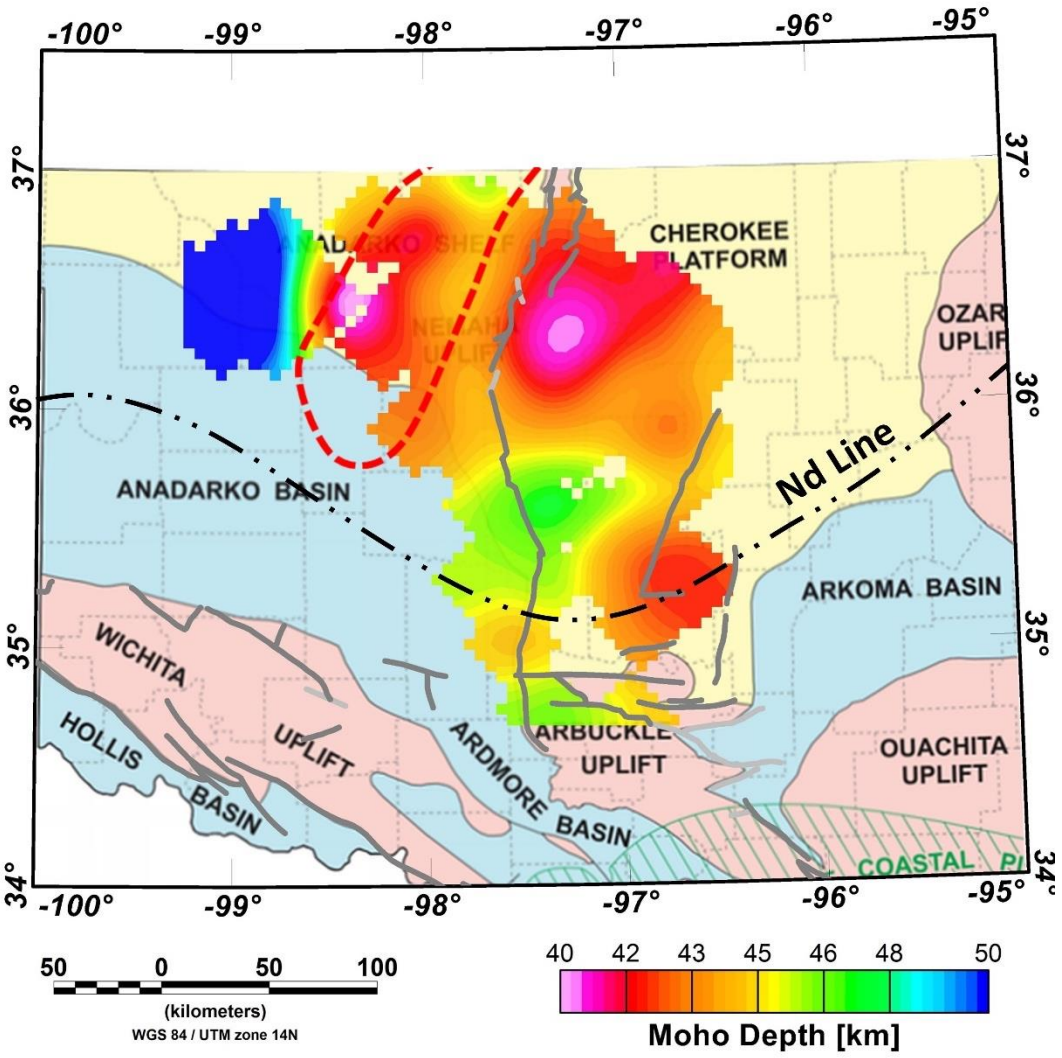


Figure 2.5 The interpolated Moho depth map. Grey lines indicate major basement faults. The red shape encompasses the possible continuation of the MCR into Oklahoma as proposed by C. A. Stein (2014).

2.6 Discussion

2.6.1 Moho Depths

Early crustal-scale seismological investigations in Oklahoma provide crustal thickness estimates ranging from 45 km to 50 km (Tryggvason and Qualls, 1967; Mitchell and Landisman, 1970). The

deployment of the USArray provided a dataset with complete coverage of the midcontinent at a large station spacing (60 km) (Schmandt, Lin and Karlstrom, 2015; McGlannan and Gilbert, 2016; Shen and Ritzwoller, 2016b; Ma and Lowry, 2017). In these data, the Moho in Oklahoma shallows towards the east, which coincides with the large-scale transition from the mountain region to the mid-east continent (Shen and Ritzwoller, 2016b).

In our study, crustal thickness ranges from 40 km to 55 km, which generally agrees with the previously published depth estimates. The new Moho depth map provides a laterally continuous and geologically plausible model of the regional crustal structure, as the depths based on our model are devoid of scatter among adjacent stations as seen in Moho depth compilations based on the USArray data (Schmandt, Lin and Karlstrom, 2015; Shen and Ritzwoller, 2016b; Ma and Lowry, 2017). Moho depths in the Nemaha Uplift region and northern Cherokee Platform region appear relatively shallow (~41 – 44 km) when compared to the Anadarko Shelf to the west and the Cherokee Platform to the south (~44 – 47 km). The crust is significantly thicker (~50 km) in the northwestern part of the Anadarko shelf. This deepening trend toward the west is also found in many studies of the USArray (Schmandt, Lin and Karlstrom, 2015; McGlannan and Gilbert, 2016; Shen and Ritzwoller, 2016b; Ma and Lowry, 2017). Although the station coverage is relatively poor in the southernmost part of our study area, there is no significant shallowing or deepening trend towards the tectonically younger region, where several uplifts and fault zones exist close to the Southern Oklahoma Aulacogen.

A regional shallowing of the Moho discontinuity is observed east of the Nemaha Uplift at the Northern Cherokee Platform. Although the depth extent of the crustal deformation resulting from Nemaha ridge tectonic activity is unknown, the literature suggests that the Nemaha Uplift and fault

zone represent an upper crustal feature only, which was formed in Late Mississippian-Early Pennsylvanian time (McBee Jr, 2003; Shah and Keller, 2017).

The Nd line that goes across both Southern and Eastern Granite-Rhyolite Province is delineated by the spatial distribution of isotopic dating samples, defining the formation age variation between Paleoproterozoic and Mesoproterozoic (Bickford et al., 1981, 2015; Nelson and DePaolo, 1985; van Schmus, Bickford and Turek, 1996; Renee Rohs and van Schmus, 2007). Although the Nd line is not considered a structural boundary, studies of A-type plutons suggest a different origin of the lithospheric units south and north of the Nd line. The crustal thickness does not show significant variation across the Nd line which is consistent with previous RF analysis in the Eastern Granite-Rhyolite Province near the Reelfoot Rift region (Chen et al., 2018). The isotropic and spatial analysis for the basement rock samples of the midcontinent also suggests a transitional zone instead of a sharp boundary between Paleoproterozoic and Mesoproterozoic crust (Bickford et al., 2015), as the structure associated with the boundary might be overprinted by Phanerozoic deformation.

2.6.2 Integration with basement depths, crustal velocities, and potential field datasets

In order to put our results into a broader context and support the interpretation, we combine the stacked RF results with other observables: (1) a recently established 3D crustal P-wave velocity model by Ratre & Behm (2021), (2) the basement depth map of Campbell and Weber (2006), and (3) Bouguer gravity and magnetic reduced-to-pole (RTP) anomalies from the USGS (Magnetic anomaly map of North America [Map], 1987; Gravity anomaly map of North America [Map],

1988). We further superimpose depths from the interpolated and smoothed Moho map as well as the averaged depths and associated uncertainties at the individual stations. These datasets are visualized together with the depth-converted RFs along three vertical ‘pseudo-cross sections’ (Figs. 6 - 8). Along each section, the RFs of adjacent stations are plotted equidistantly. This approach has been chosen due to the highly irregular station spacing, which does not allow a meaningful migration or projection onto a straight line.

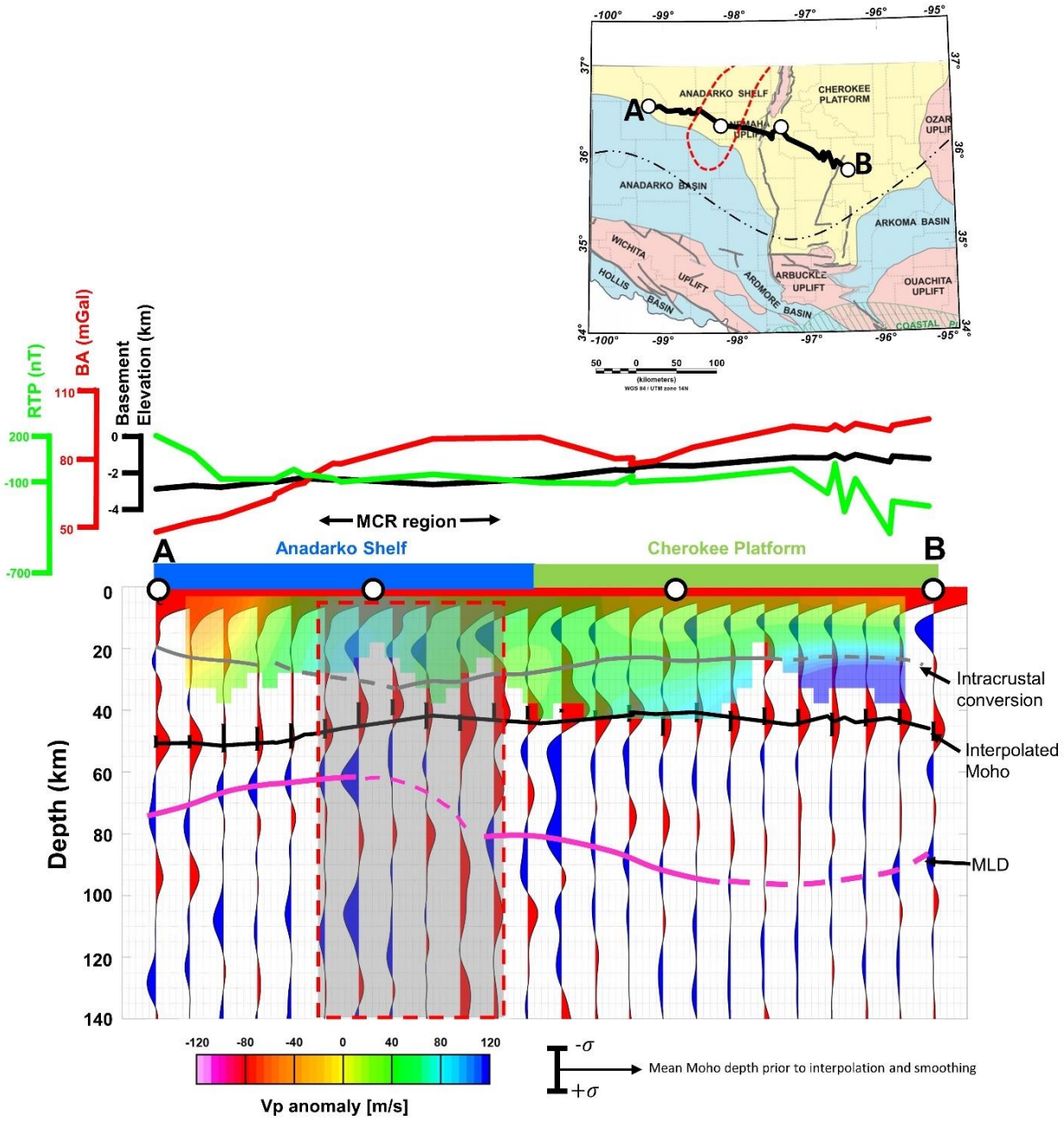


Figure 2.6 RF Pseudo-cross section A-B overlain with crustal P wave velocity anomaly (Ratre and Behm, 2021). The velocity anomaly represents the deviation of an average 1D velocity-depth function. The thick black line is the Moho depth extracted from the interpolated Moho depth map (Figure 2.5). The grey line is the intracrustal discontinuity, and the pink line denotes the MLD (mid-lithospheric discontinuity) of the upper mantle. This profile is from the Anadarko Shelf,

trending southeast, to the Cherokee Platform near central Oklahoma as shown in the inset map. Above the cross-section, the magnetic anomaly (green line), Bouguer gravity anomaly (red line), and basement depths (black line) along the profile are shown. The overlapping region of the proposed MCR with this profile is marked with a shaded rectangle. Note that the equidistant trace spacing does not represent true inter-station distances. Uncertainty of Moho estimation prior to interpolation and smoothing is plotted with blue error bars on top of the Pms phase.

Pseudo-cross section A-B (Figure 2.6) crosses the study area from the NW corner through the Anadarko shelf, the Nemaha Fault zone, and the Central Cherokee Platform. The interpolated Moho depths correlate with the long-wavelength structure of the Bouguer anomaly, indicating a thickening of the crust towards the NW. It is also noted that the shallow crustal velocities are low in this region, while the RTP anomaly suddenly increases. The change of multiple geophysical observables and their associated rock properties may suggest the existence of a different and previously unmapped crustal/lithospheric unit in the NW of the study area, although our data do not strictly require such an explanation. The interpretation of a potential MLD is based on the correlation with adjacent stations along section A-C in the north, although the amplitudes are significantly weaker in section A-B.

Pseudo-cross section A-C (Figure 2.7) starts in the same area as the section A-B but then follows a strictly easterly course and again crosses the northern part of the Nemaha Uplift and Northern Cherokee Platform. The local gravity high close to the Nemaha uplift correlates with a shallow positive velocity anomaly but no significant Moho depth variation. In the Cherokee Platform North, the Moho signature is rather distinct and indicates a depth of 42 km. As opposed to profile A-B, the RTP anomaly is almost constant in the northmost part of the Cherokee Platform, and the velocity model of Ratre and Behm (2021) shows moderate P-wave velocities in the upper crust.

Below the Moho, and in particular, in the central and eastern parts of the section, we find a pronounced negative conversion at depths ranging from 60 to 85 km. This mid-lithospheric discontinuity (MLD) is discussed in section 5.4.

Following Ratre & Behm (2021), we attribute the short-wavelength gravity anomaly close to the Nemaha uplift to a crustal discontinuity which presents positive velocity anomaly. This location also corresponds to the MCR as proposed by Stein et al. (2018), but we find no significant variation in Moho depth or basement depth. The P-wave velocities in the upper crust are significantly increased. It is also noted that the RTP anomalies become more variable here and generally tend to weaken. A possible explanation for the variation of the crustal properties is the intrusive rift-filling volcanics from MCR, which is further discussed in section 2.5.3.

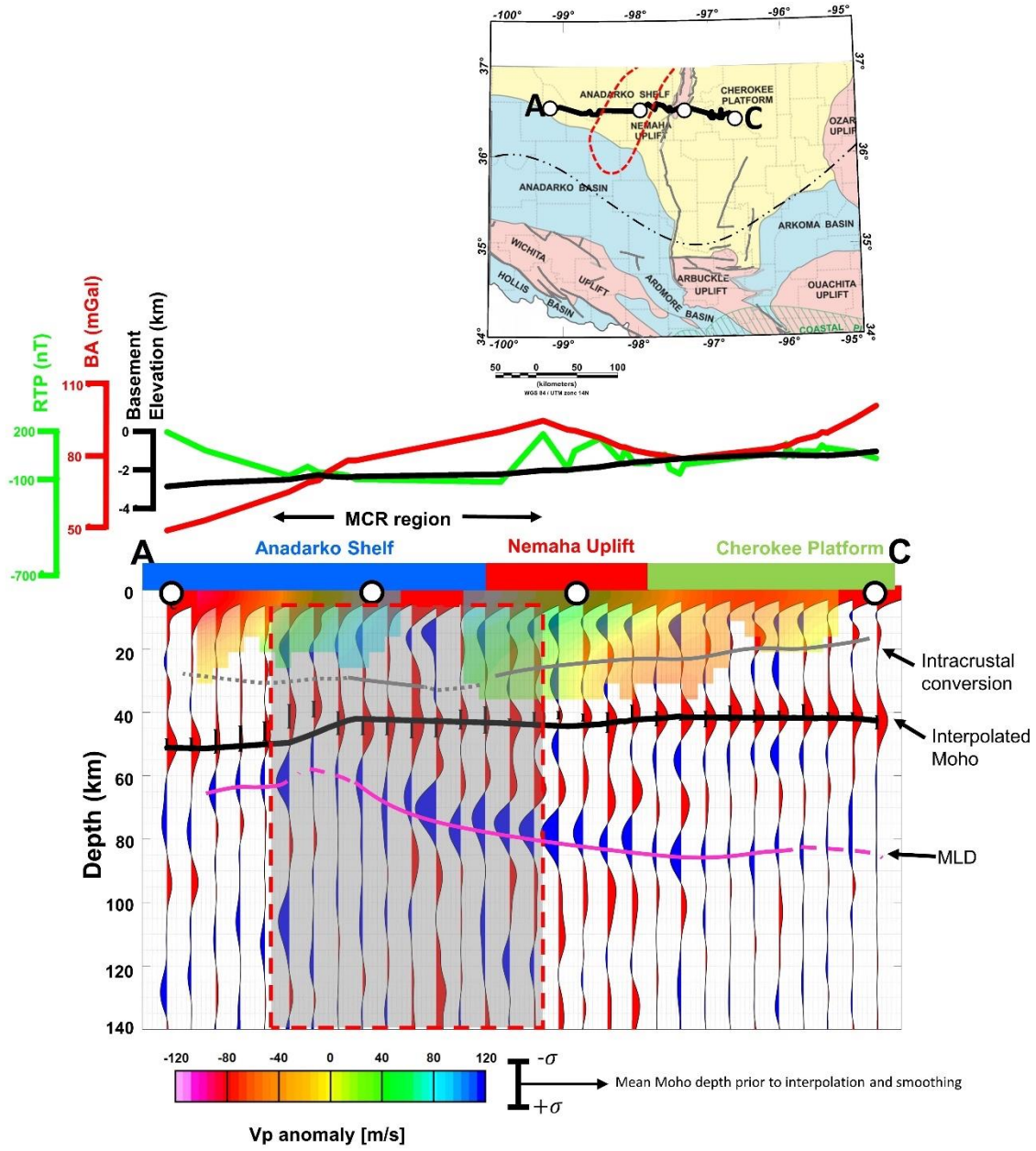


Figure 2.7 RF Pseudo-cross section A-C overlapped with crustal P wave anomaly. This profile is from the Anadarko Shelf, trending east to the northern part of the Cherokee Platform. All lines, symbols and annotations are the same as in Figure 2.6.

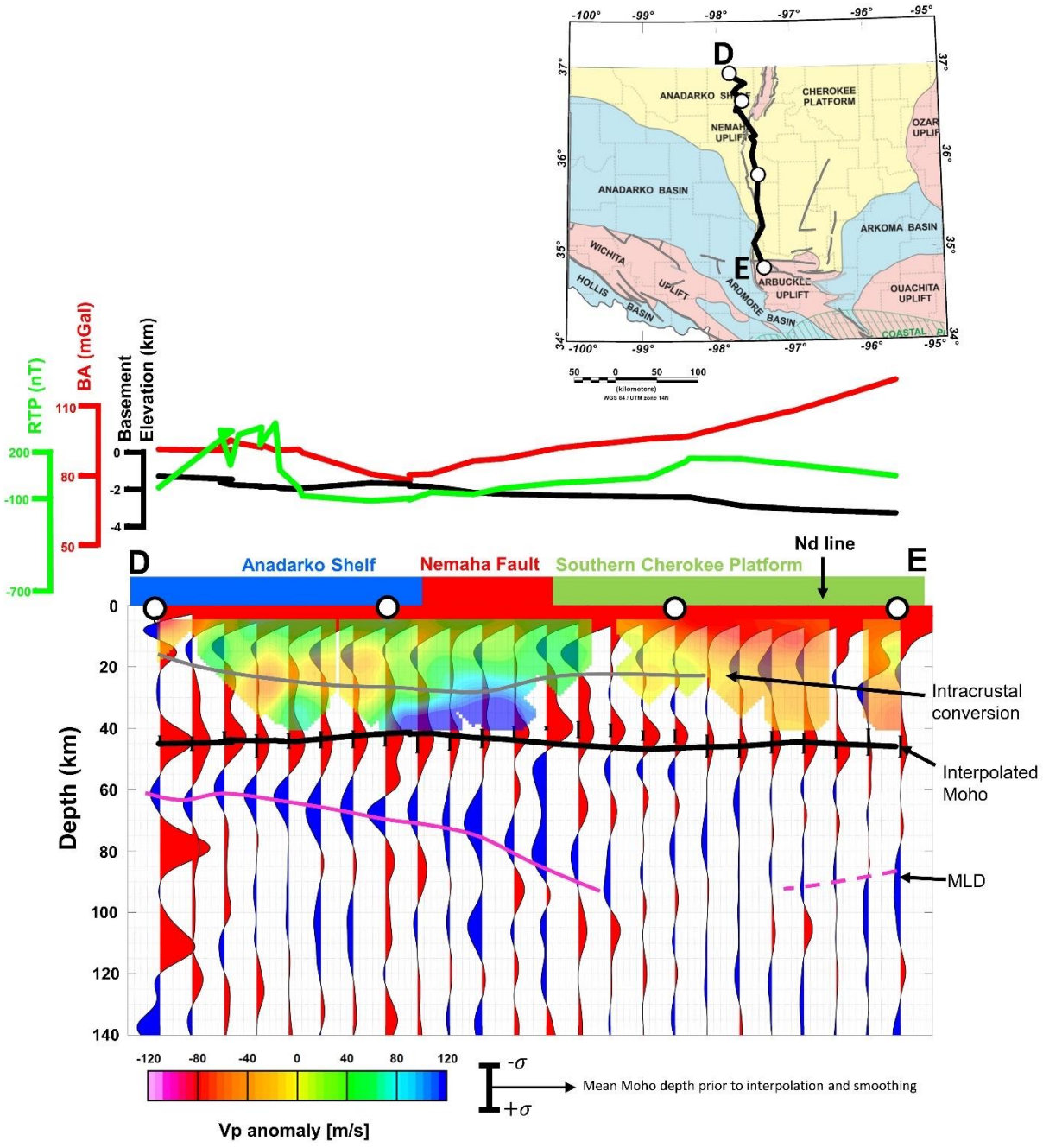


Figure 2.8 RF Pseudo-cross section D-E overlapped with crustal P wave anomaly (Ratre and Behm, 2021). This profile is from the Nemaha Uplift, trending south, to the Arbuckle Uplift near the Southern Oklahoma Aulacogen. All lines, symbols and annotations are the same as in Figure 2.6 while the location of the intersection between this profile and the Nd line is denoted.

Finally, we show a north-south trending pseudo-cross section crossing the entire Cherokee platform from north to south and ending in the Arbuckle uplift (Figure 2.8). The Moho again appears relatively flat in the northern part, and the long-wavelength gravity anomaly can be correlated with the decreased middle and lower crustal velocities. The significant rise of the gravity anomaly at the end of the section is not captured in our RF data due to its location at the edge, but we note that the crustal velocity model indicates a change to higher seismic velocities. Local magnetic anomalies correlate with shallow positive velocity anomalies.

The intracrustal conversion is notable in all three profiles with a depth range from 15 to 30 km, and mainly occurs in the northern regions near the gravity anomaly high that delineates the MCR extension. Cross-sections show the converter dips into the debated MCR region although its occurrence at the west of the MCR region is obscure (Figure 2.6, 2.7, 2.8). We interpret the intracrustal layer to be associated with limited rifting of MCR at the southern end, which is further discussed in the following section.

2.6.3 Mid-Continent Rift

The Mid-Continent Rift System, one of the largest failed rifts in North America, is characterized by prominent gravity and magnetic anomalies as a result of the thickened crust due to syn-rift and post-rift igneous material (Schmus & Hinze, 1985; C. A. Stein et al., 2015; Woelk & Hinze, 1991). Defined by the strong positive gravity anomalies, the southern extension of the MCR western arm into northern Kansas is widely accepted (Stein et al., 2015; S. Stein et al., 2018). Several studies (Adams and Keller, 1994; S. Stein et al., 2018; Kolawole, Simpson Turko and Carpenter, 2020) also proposed a potential MCR extension into north-central Oklahoma (Figure 2.1) based on a significantly weaker gravimetric anomaly. Additionally, the sheet-like mafic intrusions found in

the Oklahoma basement and adjacent regions indicate broad crustal magmatism and an extensional regime origin, which can potentially be explained by the MCR rift-filling (Kolawole, Simpson Turko and Carpenter, 2020). In contrast, the hypothesis of MCR extension to Oklahoma and even down to Texas and New Mexico is questioned due to the absence of supporting magnetic anomalies and rift basin fillings from drill holes (Hinze and Chandler, 2020). The crustal velocity model of Oklahoma from local earthquake tomography does not suggest a significant velocity variation across the linear gravity anomaly (Ratre and Behm, 2021).

Elling et al. (2020) proposed a structural model for each arm of the MCR by integrating the estimation of magma volume, seismic studies, and gravity models. These models delineate prominent crustal deformations due to the initiation and termination of rifting, including a symmetrical deepening of Moho with underplated mafic material overlaid, and a rift-filling volcanic package at mid-crustal levels. In the northern part of the MCR, these structures are confirmed by seismic surveys, in which two converted phases occur at the depth of 40-60 km, corresponding to the Moho discontinuity and underplate materials, and intracrustal discontinuities, corresponding to the mafic rift-filling (Zhang et al., 2016).

The Moho depth map in our study does not show the pronounced symmetrical to semi-symmetrical deepening across the gravity anomaly region which is prominent in the northern part of the MCR. Although an eastward shallowing is present across the 'MCR' region (Figure 2.6 and 2.7), we interpret the Moho depth variation to be associated with continental-scale shallowing from the US mountain area to the mid-east continent rather than being MCR magmatism induced (Schmandt, Lin and Karlstrom, 2015; McGlannan and Gilbert, 2016; Shen and Ritzwoller, 2016b; Ma and Lowry, 2017). However, the intracrustal discontinuity that deepens from the Cherokee Platform to the west of the Nemaha Uplift may indicate rift-filling volcanic rock. The intracrustal layer

conversion phase is pronounced at the Nemaha Uplift region and Northern Cherokee Platform and the deepest occurrence of the conversion phase falls into the gravity anomaly region (Figure 2.7, 2.8), whose depth agrees with the rift-basin volcanic filling of the MCR western arm model proposed (Elling et al., 2020). Underlaid by a relatively flat Moho, the mafic intrusion delineated by the deepened intracrustal discontinuity may produce the regional gravity anomaly high.

Merino et al. 2013 proposed models of MCR along the rift axis based on intrusion volcanic volume and gravity anomaly, indicating a varied thickness of underplate and rift-filling volcanics from the Lake Superior Hotspot to the southern end of the west and eastern arm: the volume of volcanics intruded into the crust decrease from Lake Superior region at the north. Consequently, the decreased intrusive volcanic volume may correspond to less Moho deformation as the in-rift and out-rift Moho topography differences reduce from Lake Superior to Iowa and Kansas (Woelk and Hinze, 1991b; Moidaki et al., 2013; Zhang et al., 2016). It is reasonable to assume, as the rifting ceased, the extensional regime from Lake Superior failed to reach the southern end of the rifting, leaving undeformed Moho. Therefore, our observation of a relatively flat Moho and the existence of an intracrustal conversion may imply a configuration where the extensional regime ceased, leading to only minor deformation to the Precambrian crust.

2.6.4 Mid-lithospheric discontinuity (MLD)

The most striking feature in cross sections A-C and D-E is a NW-SE-dipping converter with negative polarity in the upper mantle in a depth range from 60 to 90 km and centered at the Nemaha uplift (Figure 2.7, 2.8), which represents upper mantle negative velocity gradients. While the dip resembles a subduction feature, the direction is opposed to the commonly accepted evolutional

model for the mid-continent where accretion occurred through SE-to-NW oriented subduction (Whitmeyer and Karlstrom, 2007).

Upper mantle negative velocity gradients are reported in several seismological studies targeting the lithosphere (Plomerová, Kouba and Babuška, 2002; Kind, Yuan and Kumar, 2012b). In the North American plate, negative velocity gradients are also documented in USArray data (Kind, Yuan and Kumar, 2012b; Lekić and Fischer, 2014a; Hansen, Dueker and Schmandt, 2015; Hopper and Fischer, 2015a; Chen et al., 2018) and previous studies from more sparsely distributed stations across the continent (Abt et al., 2010; Yuan and Romanowicz, 2010). The negative velocity gradient in our data is right beneath the Moho at the Anadarko Shelf region (~ 60 km) and deepens towards the SE to around 85 km at the Cherokee Platform (Figure 2.7, 2.8), while its expression in the Southern Cherokee platform and in the eastern part of the study area is less pronounced. The negative velocity gradient likely represents a mid-lithospheric discontinuity (MLD) across the midcontinent. The depth of the conversion agrees with the continental-scale lithospheric structure studies (Yuan and Romanowicz, 2010; Kind, Yuan and Kumar, 2012b; Lekić and Fischer, 2014a) which show a similar upper-mantle MLD at 60-120 km, shallowing towards young provinces from the oldest part of the craton.

There are multiple explanations for the MLD. The lithosphere-asthenosphere boundary (LAB) is a potential candidate. While multiple geophysical and geomechanical studies (Gung, Panning and Romanowicz, 2003; Griffin et al., 2004; Mareschal, 2004; Carlson, Pearson and James, 2005) suggest the LAB depth of the North American plate is between 200 and 250 km, some tomographic and receiver function studies indicate considerably thinner lithosphere according to a shallow negative velocity gradient (100-140 km) (Kumar et al., 2012). The LAB is assumed to represent a more gradual velocity decrease with depth and is usually well visible on S-to-P receiver functions.

Kumar et al. (2012) established a LAB depth map for the US-TA data and obtained depths of around 90 km for this region, which roughly agrees with the depth shown here. They also discuss the ambiguity of the definition and identification of the LAB and refer to other studies which find well-defined mid-lithospheric discontinuities (MLD) in continental settings (Abt et al., 2010; Yuan and Romanowicz, 2010).

Another possible explanation for the MLD is related to ancient cratons. Based on variable anisotropy signature, some studies of the upper mantle structure of North America propose a stratified uppermost mantle (Yuan and Romanowicz, 2010; Kind et al., 2015), which corresponds to different ancient cratons (Kind et al., 2015; Yuan & Romanowicz, 2010). The configuration of the stratified upper mantle may record an alternation of the cratonic lithosphere melt, and the MLD could reflect a lower boundary of ancient lithosphere that collided with the Laurentia plate.

2.7 Conclusions

Our RF analysis provides the first image of the Moho discontinuity in Oklahoma using teleseismic data recorded on multiple dense monitoring networks. It presents an update to previous studies that provide either local information along 2D lines or low-resolution models based on a large station spacing. Revealed by the depth-converted RFs, the Moho depth of central to central-north Oklahoma ranges from 40 km to 55 km, where the deepest Moho occurs at Anadarko Shelf to the northwest and shallows to the east, agreeing with the continental-scale crustal studies that present shallowing Moho from mountain region to the mid-east continent (Ma & Lowry, 2017; McGlannan & Gilbert, 2016; Schmandt et al., 2015; Shen & Ritzwoller, 2016). The Moho topography does not exhibit significant variation nor intrusive underplate across the debated MCR region, but an

intracrustal conversion that dips towards the linear gravity anomaly may suggest rift-filling volcanism in the upper crust. A mid-lithosphere discontinuity, presenting a coherent negative phase in the RF traces, is found beneath the Oklahoma crust with a range of depth from 60 km to 100 km, in agreement with the depth of the upper mantle discontinuity suggested by continental-wide seismic studies (Abt et al., 2010; Chen et al., 2018; Hansen et al., 2015; Hopper & Fischer, 2015a; Kind et al., 2012; Lekić & Fischer, 2014a; Yuan & Romanowicz, 2010)

Overall, our study also highlights the potential of local and regional seismic monitoring networks for investigating crustal and mantle structures. Further research should include analysis of potential anisotropic effects in the RFs as well as application of other methods such as teleseismic tomography and shear wave splitting.

2.8 References

Abt, D. L., Fischer, K. M., French, S. W., Ford, H. A., Yuan, H., & Romanowicz, B. (2010). North American lithospheric discontinuity structure imaged by Ps and Sp receiver functions. Journal of Geophysical Research, 115(B9), B09301. https://doi.org/10.1029/2009JB006914

Adams, D. C., & Keller, G. R. (1994). Possible extension of the Midcontinent Rift in west Texas and eastern New Mexico. Canadian Journal of Earth Sciences, 31(4), 709–720. https://doi.org/10.1139/e94-063

Adams, D. C., & Keller, R. (1996). Precambrian Basement Geology of the Permian Basin Region of West Texas and Eastern New Mexico: A Geophysical Perspective. AAPG Bulletin, 80. https://doi.org/10.1306/64ED87FA-1724-11D7-8645000102C1865D

Anderson, J. L. (1999). Paleo- and Mesoproterozoic granite plutonism of Colorado and Wyoming. Rocky Mountain Geology, 34(2), 149–164. https://doi.org/10.2113/34.2.149

Anderson, J. L., & Bender, E. E. (1989a). Nature and origin of Proterozoic A-type granitic magmatism in the southwestern United States of America. Lithos, 23(1–2), 19–52. https://doi.org/10.1016/0024-4937(89)90021-2

Anderson, J. L., & Bender, E. E. (1989b). Nature and origin of Proterozoic A-type granitic magmatism in the southwestern United States of America. Lithos, 23(1–2), 19–52. https://doi.org/10.1016/0024-4937(89)90021-2

Anderson, J. L., & Morrison, J. (1992). Chapter 7 The Role of Anorogenic Granites in the Proterozoic Crustal Development Of North America (pp. 263–299). https://doi.org/10.1016/S0166-2635(08)70121-X

Anderson, J. L., & Morrison, J. (2005). Ilmenite, magnetite, and peraluminous Mesoproterozoic anorogenic granites of Laurentia and Baltica. Lithos, 80(1–4), 45–60. https://doi.org/10.1016/j.lithos.2004.05.008

Bickford, M. E., HARROWER, K. L., HOPPE, W. J., NELSON, B. K., NUSBAUM, R. L., & THOMAS, J. J. (1981). Rb-Sr and U-Pb geochronology and distribution of rock types in the Precambrian basement of Missouri and Kansas. Geological Society of America Bulletin, 92(6), 323. https://doi.org/10.1130/0016-7606(1981)92<323:RAUGAD>2.0.CO;2

Bickford, M. E., & Lewis, R. D. (1979). U-Pb geochronology of exposed basement rocks in Oklahoma. Geological Society of America Bulletin, 90(6), 540. https://doi.org/10.1130/0016-7606(1979)90<540:UGOEBR>2.0.CO;2

Bickford, M. E., van Schmus, W. R., Karlstrom, K. E., Mueller, P. A., & Kamenov, G. D. (2015). Mesoproterozoic-trans-Laurentian magmatism: A synthesis of continent-wide age distributions, new SIMS U–Pb ages, zircon saturation temperatures, and Hf and Nd isotopic compositions. Precambrian Research, 265, 286–312. https://doi.org/10.1016/j.precamres.2014.11.024

Bickford, M. E., Van, W. R., & Zietz, I. (1986a). Proterozoic history of the midcontinent region of North America. Geology, 14(6), 492. https://doi.org/10.1130/0091-7613(1986)14<492:PHOTMR>2.0.CO;2

Bickford, M. E., Van, W. R., & Zietz, I. (1986b). Proterozoic history of the midcontinent region of North America. Geology, 14(6), 492. https://doi.org/10.1130/0091-7613(1986)14<492:PHOTMR>2.0.CO;2

Black, W. (1955). Study of the marked positive gravity anomaly in the northern midcontinent region of the United States. Geol. Soc. Am. Bull, 66(1531).

Brewer, J. A., Good, R., Oliver, J. E., Brown, L. D., & Kaufman, S. (1983). COCORP profiling across the Southern Oklahoma aulacogen: Overthrusting of the Wichita Mountains and compression within the Anadarko Basin. Geology, 11(2), 109. https://doi.org/10.1130/0091-7613(1983)11<109:CPATSO>2.0.CO;2

Brewer, J. A., & Oliver, J. E. (1980). Seismic Reflection Studies of Deep Crustal Structure. Annual Review of Earth and Planetary Sciences, 8(1), 205–230. https://doi.org/10.1146/annurev.ea.08.050180.001225

Bright, R. M., Amato, J. M., Denyszyn, S. W., & Ernst, R. E. (2014). U-Pb geochronology of 1.1 Ga diabase in the southwestern United States: Testing models for the origin of a post-Grenville large igneous province. Lithosphere, 6(3), 135–156. https://doi.org/10.1130/L335.1

Burke, K. (1977). Aulacogens and Continental Breakup. Annual Review of Earth and Planetary Sciences, 5(1), 371–396. https://doi.org/10.1146/annurev.ea.05.050177.002103

Campbell, J. A., & Weber, J. L. (2006). Wells drilled to basement in Oklahoma. Oklahoma Geological Survey Special Publication, 1. https://www.ou.edu/ogs/data/oil-gas

Carlson, R. W., Pearson, D. G., & James, D. E. (2005). Physical, chemical, and chronological characteristics of continental mantle. Reviews of Geophysics, 43(1). https://doi.org/10.1029/2004RG000156

Cassidy, J. F. (1992). Numerical experiments in broadband receiver function analysis. Bulletin of the Seismological Society of America, 82(3), 1453–1474. https://doi.org/10.1785/BSSA0820031453

Cawood, P. A., & Pisarevsky, S. A. (2017). Laurentia-Baltica-Amazonia relations during Rodinia assembly. Precambrian Research, 292, 386–397. https://doi.org/10.1016/j.precamres.2017.01.031

Chen, C. (2016). Comprehensive analysis of Oklahoma earthquakes: From earthquake monitoring to 3D tomography and relocation.

Chen, C., Gilbert, H., Fischer, K. M., Andronicos, C. L., Pavlis, G. L., Hamburger, M. W., Marshak, S., Larson, T., & Yang, X. (2018). Lithospheric discontinuities beneath the U.S. Midcontinent – signatures of Proterozoic terrane accretion and failed rifting. Earth and Planetary Science Letters, 481, 223–235. https://doi.org/10.1016/j.epsl.2017.10.033

Craddock, C., Thiel, E. C., & Gross, B. (1963). A gravity investigation of the Precambrian of southeastern Minnesota and western Wisconsin. Journal of Geophysical Research, 68(21), 6015–6032. https://doi.org/10.1029/JZ068i021p06015

Elling, R. P., Stein, S., Stein, C. A., & Keller, G. R. (2020). Tectonic implications of the gravity signatures of the Midcontinent Rift and Grenville Front. Tectonophysics, 778, 228369. https://doi.org/10.1016/j.tecto.2020.228369

Frassetto, A. M., Zandt, G., Gilbert, H., Owens, T. J., & Jones, C. H. (2011a). Structure of the Sierra Nevada from receiver functions and implications for lithospheric foundering. Geosphere, 7(4), 898–921. https://doi.org/10.1130/GES00570.1

Frassetto, A. M., Zandt, G., Gilbert, H., Owens, T. J., & Jones, C. H. (2011b). Structure of the Sierra Nevada from receiver functions and implications for lithospheric foundering. Geosphere, 7(4), 898–921. https://doi.org/10.1130/GES00570.1

Goodge, J. W., & Vervoort, J. D. (2006). Origin of Mesoproterozoic A-type granites in Laurentia: Hf isotope evidence. Earth and Planetary Science Letters, 243(3–4), 711–731. https://doi.org/10.1016/j.epsl.2006.01.040

Gravity anomaly map of North America [Map]. (1988). https://guides.lib.utexas.edu/geo/d-nag

Griffin, W. L., O'Reilly, S. Y., Doyle, B. J., Pearson, N. J., Coopersmith, H., Kivi, K., Malkovets, V., & Pokhilenko, N. (2004). Lithosphere mapping beneath the North American plate. Lithos, 77(1–4), 873–922. https://doi.org/10.1016/j.lithos.2004.03.034

Gung, Y., Panning, M., & Romanowicz, B. (2003). Global anisotropy and the thickness of continents. Nature, 422(6933), 707–711. https://doi.org/10.1038/nature01559

Hansen, S. M., Dueker, K., & Schmandt, B. (2015). Thermal classification of lithospheric discontinuities beneath USArray. Earth and Planetary Science Letters, 431, 36–47. https://doi.org/10.1016/j.epsl.2015.09.009

Hinze, W. J., & Chandler, V. W. (2020). Reviewing the configuration and extent of the Midcontinent rift system. Precambrian Research, 342, 105688. https://doi.org/10.1016/j.precamres.2020.105688

Hopper, E., & Fischer, K. M. (2015a). The meaning of midlithospheric discontinuities: A case study in the northern U.S. craton. Geochemistry, Geophysics, Geosystems, 16(12), 4057–4083. https://doi.org/10.1002/2015GC006030

Hopper, E., & Fischer, K. M. (2015b). The meaning of midlithospheric discontinuities: A case study in the northern U.S. craton. Geochemistry, Geophysics, Geosystems, 16(12), 4057–4083. https://doi.org/10.1002/2015GC006030

Janiszewski, H. A., & Abers, G. A. (2015). Imaging the Plate Interface in the Cascadia Seismogenic Zone: New Constraints from Offshore Receiver Functions. Seismological Research Letters, 86(5), 1261–1269. https://doi.org/10.1785/0220150104

Karlstrom, K. E., Åhäll, K.-I., Harlan, S. S., Williams, M. L., McLelland, J., & Geissman, J. W. (2001). Long-lived (1.8–1.0 Ga) convergent orogen in southern Laurentia, its extensions to Australia and Baltica, and implications for refining Rodinia. Precambrian Research, 111(1–4), 5–30. https://doi.org/10.1016/S0301-9268(01)00154-1

Karlstrom, K. E., & Humphreys, E. D. (1998). Persistent influence of Proterozoic accretionary boundaries in the tectonic evolution of southwestern North America: Interaction of cratonic grain and mantle modification events. Rocky Mountain Geology, 33(2), 161–179. https://doi.org/10.2113/33.2.161

Keranen, K. M., Weingarten, M., Abers, G. A., Bekins, B. A., & Ge, S. (2014). Sharp increase in central Oklahoma seismicity since 2008 induced by massive wastewater injection. Science, 345(6195), 448–451. https://doi.org/10.1126/science.1255802

Kind, R., Yuan, X., & Kumar, P. (2012). Seismic receiver functions and the lithosphere–asthenosphere boundary. Tectonophysics, 536–537, 25–43. https://doi.org/10.1016/j.tecto.2012.03.005

Kind, R., Yuan, X., Mechie, J., & Sodoudi, F. (2015). Structure of the upper mantle in the north-western and central United States from USArray S-receiver functions. Solid Earth, 6(3), 957–970. https://doi.org/10.5194/se-6-957-2015

Kolawole, F., Simpson Turko, M., & Carpenter, B. M. (2020). Basement-controlled deformation of sedimentary sequences, Anadarko Shelf, Oklahoma. Basin Research, 32(6), 1365–1387. https://doi.org/10.1111/bre.12433

Kumar, P., Kind, R., Yuan, X., & Mechie, J. (2012). USArray Receiver Function Images of the Lithosphere-Asthenosphere Boundary. Seismological Research Letters, 83(3), 486–491. https://doi.org/10.1785/gssrl.83.3.486

Lekić, V., & Fischer, K. M. (2014a). Contrasting lithospheric signatures across the western United States revealed by Sp receiver functions. Earth and Planetary Science Letters, 402, 90–98. https://doi.org/10.1016/j.epsl.2013.11.026

Lekić, V., & Fischer, K. M. (2014b). Contrasting lithospheric signatures across the western United States revealed by Sp receiver functions. Earth and Planetary Science Letters, 402, 90–98. https://doi.org/10.1016/j.epsl.2013.11.026

Ligorría, J. P., & Ammon, C. J. (1999). Iterative deconvolution and receiver-function estimation. Bulletin of the Seismological Society of America, 89(5), 1395–1400. https://doi.org/10.1785/BSSA0890051395

Lynn, H. B., Hale, L. D., & Thompson, G. A. (1981). Seismic reflections from the basal contacts of batholiths. Journal of Geophysical Research: Solid Earth, 86(B11), 10633–10638. https://doi.org/10.1029/JB086iB11p10633

Lyons, P. L. (1950). A gravity map of the United States.

Ma, X., & Lowry, A. R. (2017). USArray Imaging of Continental Crust in the Conterminous United States. Tectonics, 36(12), 2882–2902. https://doi.org/10.1002/2017TC004540

Magnetic anomaly map of North America [Map]. (1987). https://guides.lib.utexas.edu/geo/d-nag

Mareschal, J. (2004). Variations of surface heat flow and lithospheric thermal structure beneath the North American craton. Earth and Planetary Science Letters, 223(1–2), 65–77. https://doi.org/10.1016/j.epsl.2004.04.002

McBee Jr, W. (2003). Nemaha strike-slip fault zone. AAPG Mid-Continent Section Meeting, 13.

McGlannan, A. J., & Gilbert, H. (2016). Crustal signatures of the tectonic development of the North American midcontinent. Earth and Planetary Science Letters, 433, 339–349. https://doi.org/10.1016/j.epsl.2015.10.048

Menuge, J. F., Brewer, T. S., & Seeger, C. M. (2002). Petrogenesis of metaluminous A-type rhyolites from the St Francois Mountains, Missouri and the Mesoproterozoic evolution of the southern Laurentian margin. Precambrian Research, 113(3–4), 269–291. https://doi.org/10.1016/S0301-9268(01)00211-X

Mitchell, B. J., & Landisman, M. (1970). Interpretation of a crustal section across Oklahoma. Geological Society of America Bulletin, 81(9), 2647-28=656.

Moidaki, M., Gao, S. S., Liu, K. H., & Atekwana, E. (2013). Crustal thickness and Moho sharpness beneath the Midcontinent rift from receiver functions. Research in Geophysics, 3(1), 1. https://doi.org/10.4081/rg.2013.e1

Nelson, B. K., & DePaolo, D. J. (1985). Rapid production of continental crust 1.7 to 1.9 b.y. ago: Nd isotopic evidence from the basement of the North American mid-continent. Geological Society of America Bulletin, 96(6), 746. https://doi.org/10.1130/0016-7606(1985)96<746:RPOCCT>2.0.CO;2

Northcutt, R. A., & Campbell, J. A. (1996). Geologic provinces of Oklahoma.

Nyman, M. W., Karlstrom, K. E., Kirby, E., & Graubard, C. M. (1994). Mesoproterozoic contractional orogeny in western North America: Evidence from ca. 1.4 Ga plutons. Geology, 22(10), 901. https://doi.org/10.1130/0091-7613(1994)022<0901:MCOIWN>2.3.CO;2

Ogden, C. S., Bastow, I. D., Gilligan, A., & Rondenay, S. (2019). A reappraisal of the H–κ stacking technique: implications for global crustal structure. Geophysical Journal International, 219(3), 1491–1513. https://doi.org/10.1093/gji/ggz364

Ojakangas, R. W., Morey, G. B., & Green, J. C. (2001). The Mesoproterozoic Midcontinent Rift System, Lake Superior Region, USA. Sedimentary Geology, 141–142, 421–442. https://doi.org/10.1016/S0037-0738(01)00085-9

Oklahoma Geological Provinces [Map]. (n.d.). Retrieved February 7, 2022, from http://ogs.ou.edu/docs/maps/map-oklahoma_geologic_provinces.pdf

Perry, W. J. (1989). Tectonic evolution of the Anadarko Basin region, Oklahoma. Department of the Interior, US Geological Survey.

Persaud, P., Pérez-Campos, X., & Clayton, R. W. (2007). Crustal thickness variations in the margins of the Gulf of California from receiver functions. Geophysical Journal International, 170(2), 687–699. https://doi.org/10.1111/j.1365-246X.2007.03412.x

Plomerová, J., Kouba, D., & Babuška, V. (2002). Mapping the lithosphere–asthenosphere boundary through changes in surface-wave anisotropy. Tectonophysics, 358(1–4), 175–185. https://doi.org/10.1016/S0040-1951(02)00423-7

Porritt, R. W., & Miller, M. S. (2018). Updates to FuncLab, a Matlab based GUI for handling receiver functions. Computers & Geosciences, 111, 260–271. https://doi.org/10.1016/j.cageo.2017.11.022

Pratt, T. L., & Haus, E. C. (1992). Widespread Buried Precambrian Layered Sequences in the U.S. Mid-Continent: Evidence for Large Proterozoic Depositional Basins (1). AAPG Bulletin, 76. https://doi.org/10.1306/BDFF89FC-1718-11D7-8645000102C1865D

Ratre, P., & Behm, M. (2021). Imaging the Deep Crustal Structure of Central Oklahoma Using Stacking and Inversion of Local Earthquake Waveforms. Journal of Geophysical Research: Solid Earth, 126(5). https://doi.org/10.1029/2020JB021368

Renee Rohs, C., & van Schmus, W. R. (2007). Isotopic connections between basement rocks exposed in the St. Francois Mountains and the Arbuckle Mountains, southern mid-continent, North America. International Journal of Earth Sciences, 96(4), 599–611. https://doi.org/10.1007/s00531-006-0123-5

Rivers, T. (1997). Lithotectonic elements of the Grenville Province: review and tectonic implications. Precambrian Research, 86(3–4), 117–154. https://doi.org/10.1016/S0301-9268(97)00038-7

Rivers, T., & Corrigan, D. (2000). Convergent margin on southeastern Laurentia during the Mesoproterozoic: tectonic implications. Canadian Journal of Earth Sciences, 37(2–3), 359–383. https://doi.org/10.1139/e99-067

Ruppel, C. (1995). Extensional processes in continental lithosphere. Journal of Geophysical Research: Solid Earth, 100(B12), 24187–24215. https://doi.org/10.1029/95JB02955

Schmandt, B., Lin, F., & Karlstrom, K. E. (2015). Distinct crustal isostasy trends east and west of the Rocky Mountain Front. Geophysical Research Letters, 42(23). https://doi.org/10.1002/2015GL066593

Schmus, W. R. van, & Hinze, W. J. (1985). The midcontinent rift system. Annual Review of Earth and Planetary Sciences, 13(1), 345–383.

Shah, A. K., & Keller, G. R. (2017). Geologic influence on induced seismicity: Constraints from potential field data in Oklahoma. Geophysical Research Letters, 44(1), 152–161. https://doi.org/10.1002/2016GL071808

Shen, W., & Ritzwoller, M. H. (2016). Crustal and uppermost mantle structure beneath the United States. Journal of Geophysical Research: Solid Earth, 121(6), 4306–4342. https://doi.org/10.1002/2016JB012887

Slagstad, T., Culshaw, N. G., Daly, J. S., & Jamieson, R. A. (2009). Western Grenville Province holds key to midcontinental Granite-Rhyolite Province enigma. Terra Nova, 21(3), 181–187. https://doi.org/10.1111/j.1365-3121.2009.00871.x

Stein, C. A., Kley, J., Stein, S., Hindle, D., & Keller, G. R. (2015). North America's Midcontinent Rift: When rift met LIP. Geosphere, 11(5), 1607–1616. https://doi.org/10.1130/GES01183.1

Stein, C. A., Stein, S., Elling, R., Keller, G. R., & Kley, J. (2018). Is the "Grenville Front" in the central United States really the Midcontinent Rift? GSA Today, 4–10. https://doi.org/10.1130/GSATG357A.1

Stein, C. A., Stein, S., Merino, M., Randy Keller, G., Flesch, L. M., & Jurdy, D. M. (2014). Was the Midcontinent Rift part of a successful seafloor-spreading episode? Geophysical Research Letters, 41(5), 1465–1470. https://doi.org/10.1002/2013GL059176

Stein, S., Stein, C. A., Elling, R., Kley, J., Keller, G. R., Wysession, M., Rooney, T., Frederiksen, A., & Moucha, R. (2018). Insights from North America's failed Midcontinent Rift into the evolution of continental rifts and passive continental margins. Tectonophysics, 744, 403–421. https://doi.org/10.1016/j.tecto.2018.07.021

Tave, M. A. (2013). Imaging of the crust and Moho beneath Oklahoma using receiver functions and Pn tomography; with emphasis on the Southern Oklahoma Aulacogen .

Thiel, E. (1956). Correlation of gravity anomalies with the Keweenawan geology of Wisconsin and Minnesota. Geological Society of America Bulletin, 67(8), 1079–1100.

Toth, C. R. (2014). Separation of the Earthquake Tomography Inverse Problem to Refine Hypocenter Locations and Tomographic Models: A Case Study from Central Oklahoma. University of Oklahoma.

Tryggvason, E., & Qualls, B. R. (1967). Seismic refraction measurements of crustal structure in Oklahoma. Journal of Geophysical Research, 72(14), 3738–3740. https://doi.org/10.1029/JZ072i014p03738

van Schmus, W. R., Bickford, M. E., & Turek, A. (1996). Proterozoic geology of the east-central Midcontinent basement. In Basement and basins of eastern North America. Geological Society of America. https://doi.org/10.1130/0-8137-2308-6.7

Wang, Z., Behm, M., & Chen, X. (2021). Oklahoma crustal deep-to-shallow structure from multiscale P-wave receiver function analysis. In AGU Fall Meeting 2021. AGU.

Wang, Z., Persaud, P., & Behm, M. (2019). Investigation of the Crust in Oklahoma from Broadband Teleseismic Receiver Functions. AGU Fall Meeting Abstracts, 2019, T21F-0401.

Whitmeyer, S., & Karlstrom, K. (2007). Tectonic model for the Proterozoic growth of North America. Geosphere, 3(4), 220. https://doi.org/10.1130/GES00055.1

Woelk, T. S., & Hinze, W. J. (1991a). Model of the midcontinent rift system in northeastern Kansas. Geology, 19(3), 277. https://doi.org/10.1130/0091-7613(1991)019<0277:MOTMRS>2.3.CO;2

Woelk, T. S., & Hinze, W. J. (1991b). Model of the midcontinent rift system in northeastern Kansas. Geology, 19(3), 277. https://doi.org/10.1130/0091-7613(1991)019<0277:MOTMRS>2.3.CO;2

Woollard, G. P. (1943). Transcontinental gravitational and magnetic profile of North America and its relation to geologic structure. Geological Society of America Bulletin, 54(6), 747–790. https://doi.org/10.1130/GSAB-54-747

Yu, Y., Song, J., Liu, K. H., & Gao, S. S. (2015). Determining crustal structure beneath seismic stations overlying a low-velocity sedimentary layer using receiver functions. Journal of Geophysical Research: Solid Earth, 120(5), 3208–3218. https://doi.org/10.1002/2014JB011610

Yuan, H., & Romanowicz, B. (2010). Lithospheric layering in the North American craton. Nature, 466(7310), 1063–1068. https://doi.org/10.1038/nature09332

Zhang, H., Lee, S., Wolin, E., Bollmann, T. A., Revenaugh, J., Wiens, D. A., Frederiksen, A. W., Darbyshire, F. A., Aleqabi, G. I., Wysession, M. E., Stein, S., & Jurdy, D. M. (2016). Distinct crustal structure of the North American Midcontinent Rift from P wave receiver functions. Journal of Geophysical Research: Solid Earth, 121(11), 8136–8153. https://doi.org/10.1002/2016JB013244

Zhu, L., & Kanamori, H. (2000). Moho depth variation in southern California from teleseismic receiver functions. Journal of Geophysical Research: Solid Earth, 105(B2), 2969–2980. https://doi.org/10.1029/1999JB900322

Zhu, X., & McMechan, G. A. (1989). 2-D tomographic imaging of velocities in the Wichita uplift-Anadarko basin region of southwestern Oklahoma. Bulletin of the Seismological Society of America, 79(3), 873–887. https://doi.org/10.1785/BSSA0790030873

Chapter 3

3 High-resolution Receiver Function Imaging Using Local Earthquakes and a Multi-channel Inversion Routine

3.1 Abstract

Receiver-side converted earthquake waves, commonly known as receiver functions (RFs), have long been employed for deep earth structure investigations. However, challenges persist when attempting to achieve high-resolution imaging of shallow (e.g., basin-scale) subsurface features using teleseismic RFs. In this study, we present a novel multi-channel blind deconvolution for computing RFs based on local and regional earthquake data from multi-station data. The proposed deconvolution method considers both the RFs and source wavelet of all local earthquakes in the dataset as unknowns and derives them by linearizing an overdetermined equation system in the frequency domain. This algorithm can reduce the instability of deconvolution for local earthquake receiver functions. Then, we apply the multichannel blind deconvolution to a local earthquake dataset from the nodal array deployed above the 2016 M5 Cushing earthquake sequence. The resulting RF profiles clearly depict the conversion of basement top interface at around 1.2 km depth, showing a remarkable correlation with the existing basement topography map. Notably, the

RF profiles reveal minimal displacement of the fault at the basement top interface, confirming the Cushing fault as a sharply delineated vertical strike-slip fault.

3.2 Introduction

P-wave Receiver Function (RF) is an established technique in seismology for studying crustal and mantle structures. Through deconvolving the vertical component recording of a sub-vertically arriving earthquake wave from the horizontal component, the computation of P-wave RF extracts the P-to-S conversions of the receiver-side impedance contrast. This generates a seismogram-like time series whose phase delays and amplitudes approximate the seismic subsurface structure below the receiver. P-wave RF is regularly applied on teleseismic events for imaging impedance boundaries of deep structures, from the upper mantle to mid-crust, such as Moho, subduction zones, and intracrustal layers (Zhu and Kanamori, 2000; Li et al., 2003; Persaud, Pérez-Campos and Clayton, 2007; Gans et al., 2011; McGlannan and Gilbert, 2016; Zhang et al., 2016; Liu, Persaud and Clayton, 2018; Wang et al., 2023).

While conventional RF studies mainly focus on deep structures, approaches for regional-scale imaging using RF have emerged over the past decade (Leahy, Saltzer and Schmedes, 2012; Licciardi and Agostinetti, 2017; Ward, Lin and Schmandt, 2018; Subašić, Agostinetti and Bean, 2019; Zhong and Zhan, 2020). Imaging small-scale structures in the shallow crust requires higher resolution RF with the capability of clearly recognizing geologic information from noise. To enhance the signal-to-noise ratio, stacking RFs from multiple events is a common practice, which suppresses the noise and strengthens the coherent phases. However, the non-uniqueness and data overfitting has been the main reason for impeding further improvement in RF resolution (Subaši´c, Agostinetti and Bean, 2019). Additional to stacking, efforts are made both in the acquisition and processing stages. The general approaches can be summarized as follows:

1) Exploiting high-frequency content from teleseismic events:

   Although the dominant frequency of teleseismic body waves is between 0.1 and ~1 Hz, some studies have proved that a higher frequency component in the teleseismic waveform can be applied to the receiver function (Leahy, Saltzer and Schmedes, 2012; Zhong and Zhan, 2020). Sophisticated ambient and background noise analysis in favor of enhancing the signal-to-noise ratio (SNR) can amplify the signal with the high-frequency component that is usually masked by noise (Liu, Persaud and Clayton, 2018). Harmonic decomposition is another recent technique to get transverse signals considered in some high-resolution receiver function studies (Bianchi et al., 2010).

2) Implement the receiver function analysis on dense-spaced arrays:

   While RF analysis can include a great number of teleseismic events to emphasize the coherent phase, adopting a dense-spaced array for data acquisition can further enhance the S/N ratio of low-energy arrivals in the higher frequency band. This can be achieved by temporally deployed seismic nodes (Cheng et al., 2021; Leahy et al., 2012; Schmandt & Clayton, 2013; X. Wang et al., 2021; Ward et al., 2018; Zhong & Zhan, 2020). Additionally, dense array data can facilitate regional structure studies as small-scale variations can be characterized across the array(Cheng et al., 2021; Leahy et al., 2012; Schmandt & Clayton, 2013; X. Wang et al., 2021; Ward et al., 2018; Zhong & Zhan, 2020).

3) New algorithms:

   The most frequently used deconvolution methods in receiver function (water-level deconvolution, multi-taper frequency-domain deconvolution, time-domain iterative

deconvolution) introduced different processing steps to facilitate the deconvolution in time and frequency domain (Clayton and Wiggins, 1976b; Ligorría and Ammon, 1999b; Park and Levin, 2001). However, the side effects of these processes are also introduced in the receiver function waveform. For example, introduction of water-level generates side lobes and multitaper would decrease spectral resolution (Kolb and Leki, 2014). To avoid these algorithm-related uncertainties in traditional deconvolution methods, novel algorithms integrate statistics-based inversion into receiver function analysis to retrieve coherent conversion phases that associate with impedance boundaries (Kolb and Leki, 2014; Zhong and Zhan, 2020).

Local and regional earthquakes that rupture at shallow crust are widely used for shallow crust imaging through tomographic methods. The converted phases of local and regional earthquake generated at shallow discontinuities have been observed in the earthquake recordings since 1990s, in which the attenuation properties of P-wave and S-wave can be estimated through spectral ratio of S wave and converted P-wave (Clouser and Langston, 1991; Chen, Chiu and Yang, 1994). Additionally, the arrival time differences between direct wave and converted wave is used to study basin structures (Umino, Hasegawa and Matsuzawa, 1995; Chen, Chiu and Yang, 1996; Bao et al., 2021; Stone, Wirth and Frankel, 2021). However, there are only a few attempts on calculating receiver function from local and regional events. Local earthquake receiver functions are confronted with two main challenges: the restricted investigation depth caused by the shallow propagation path, and the uncertainties associated with deconvolution when working with wider bandwidth local earthquake P-wave coda.

In this study, by taking advantage of a densely spaced receiver network geometry, we exploit seismic signals from local events and adapt a multichannel blind deconvolution method (Behm and Shekar, 2014) for calculating high-resolution RF for basin-scale imaging (< 2 km depth) from converted waves. The multichannel blind deconvolution can effectively enhance the coherent phases and suppress the noise by solving an overdetermined set of deconvolution equations. We introduce the multi-channel blind deconvolution for RF in the methodology section. We then demonstrate the feasibility of exploiting local events data in receiver function to image the ultra-shallow basin-scale structures. Synthetic modelling is used to understand the pattern of P-wave related surface multiples and S-waves conversion of regional earthquakes on the vertical and horizontal components. Finally, we will present the result of applying the multichannel blind deconvolution to a real data set at Cushing Oklahoma, in which 22 prescreened local events were recorded over the one-month node deployment period.

3.3 Method

A P-wave RF rf(t) is a time series representing the receiver-side subsurface structure in terms of P-to-S-wave conversion coefficients. The basic notation in time domain is usually given as

$$s(t) = w(t) * rf(t) \qquad \text{Eq. 1}$$

where the * sign indicates convolution. In equation (1), w is the P-wave source wavelet and s is the converted S-wave.

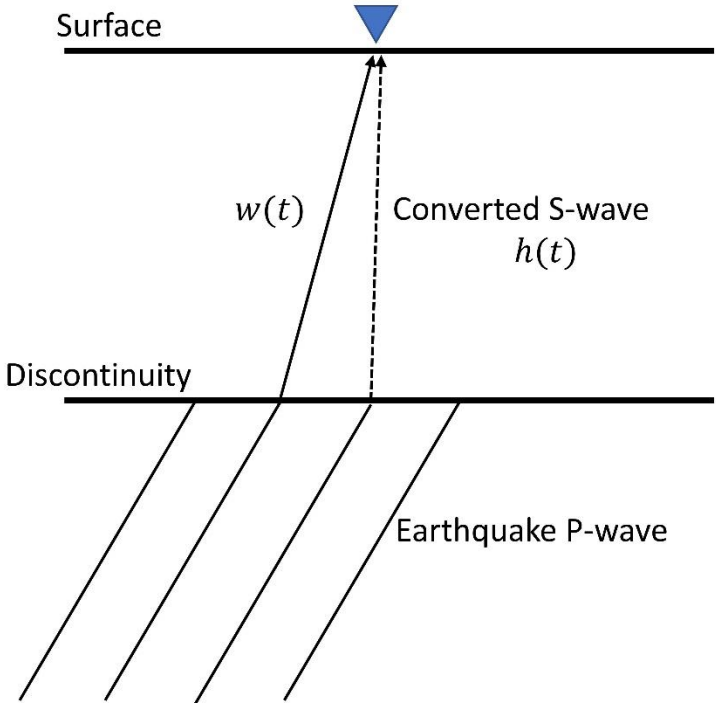


Figure 3.1 Wave propagation diagram of receiver function and b) blind deconvolution scheme. Note the dashed line represents converted S-wave.

The conventional deconvolution approach for receiver function analysis approximates the source wavelet (w) from the observed vertical component recording (z) of the recorded event P-wave arrival, while the observed S-wave is taken from the horizontal components recording (h) of the event (Figure 3.1) such that equation (1) changes to

$$h(t) = z(t) * rf(t) \qquad \text{Eq. 2}$$

This approximation is usually valid for teleseismic receiver function since the source events are teleseismic events with subvertical ray path at the receiver side such that P-waves dominate the vertical component and S-waves dominate the horizontal components. In equation (2), both h(t)

and $z(t)$ are now considered as observations (known data), while $rf(t)$ is the unknown model parameter. The receiver function (rf) is then simply calculated by deconvolving $z(t)$ from $h(t)$.

However, the noise at both vertical and radial components may destabilize the deconvolution. The presence of noise and deviation from perfect vertical incidence are also the reasons why, in a strict sense, $w(t)$ and $s(t)$ in equation (1) have to be considered as unknowns.

An intermediate form between equations (1) and (2) might be written as

$$h(t) = w(t) * rf(t) \qquad \text{Eq. 3}$$

When deconvolving the wavelet term $w(t)$ from the horizontal component $h(t)$ to obtain the receiver function $rf(t)$ following the formulation in equation (3), the task transforms into a typical challenge of blind deconvolution, where two unknowns (w, rf) need to be recovered from one observation (h)(Stockham, Cannon and Ingebretsen, 1975).

For the methodologically similar problem of imaging the receiver-side P-wave reflection series from surface-related multiples of teleseismic events, Behm and Shekar (2014) proposed a multichannel blind deconvolution method for data recorded at the vertical component of closely spaced receiver arrays. In the following, we show how we adapted this approach to the deconvolution in receiver function analysis. In their approach, Behm and Shekar (2014) depict the observed vertical component data as the superposition of a near-vertical plane wave (e.g., the wavefront of a teleseismic arrival) and its associated surface-related multiples (Figure 3.2):

$$z(t) = w(t) - w(t) * r(t) \qquad \text{Eq. 4}$$

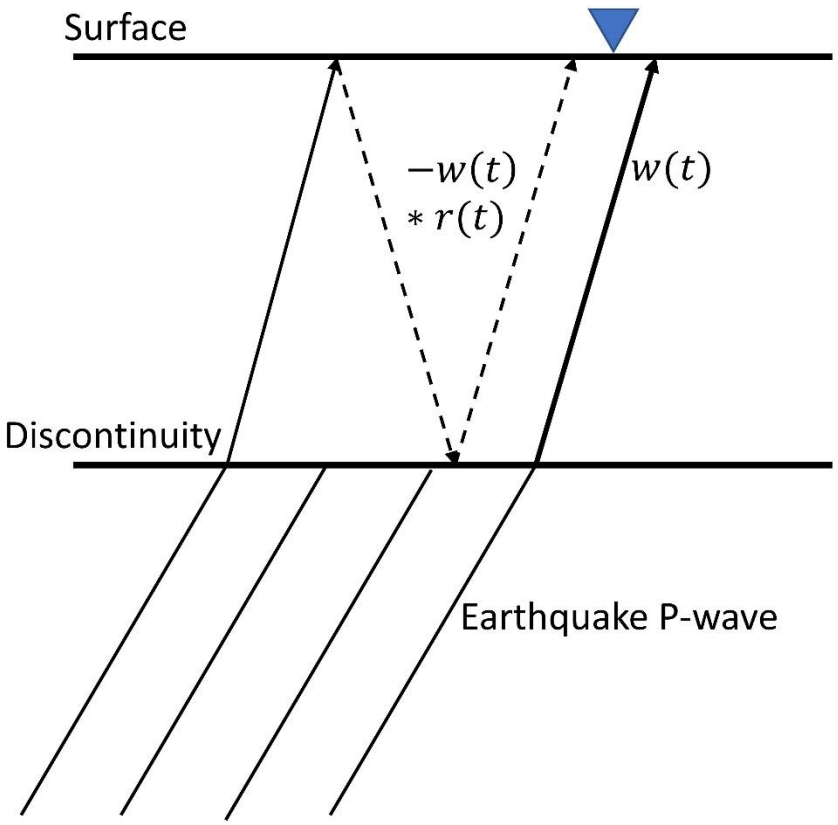


Figure 3.2 Wave propagation diagram of direct P wave and surface multiples. Note the dashed line represents surface reflected wave in the blind deconvolution scheme.

where z(t) represents vertical component data, w(t) represents a plane wavefront of the earthquake P-wave source wavelet, and r(t) characterizes the shallow two-way zero-offset reflectivity series, which captures the desired image of the subsurface structure. In their case, the superposition approach is required because they use low-frequency source wavelets (0.5 - 2 Hz) to model shallow (0.5 - 2 s two-way-travel time) subsurface structures. This also leads to the problem of blind deconvolution since w(t) cannot be extracted from the recorded data and therefore needs to be considered as a second unknown. Behm and Shekar (2014) rely on a dense receiver network with a recording aperture which is small compared to the wavelength of teleseismic events. Consequently, for each event, the source wavelet w(t) is assumed stationary

across the array while the subsurface structure beneath each recording station is characterized by an unknown reflectivity series $r(t)$. In a given recording system with station number of M and event number of N, eq. 4 can be written as

$$z_{nm}(t) = w_n(t) - w_n(t) * r_m(t) \quad \begin{matrix} n=1,2,3.....N \\ m=1,2,3.....M \end{matrix} \qquad \text{Eq. 5}$$

where N equals the total number of recorded events, and M equals the total number of stations. For the recording system that satisfies $N \times M > N + M$, the equation 5 system becomes overdetermined. Therefore, rather than calculating the individual reflectivity structure $r(t)$ of each station from single-station-based observation, the multichannel deconvolution resolves the reflectivity series through an inversion approach by establishing an overdetermined inverse problem regarding observation (vertical component z) and unknown elements (source wavelet w and reflectivity series r). The primary assumption of setting up this inverse problem is the stationary source wavelet respect to the receiver aperture. This assumption can be fulfilled under a small array aperture against the wavelength of the teleseismic events when the body wave of teleseismic event can be considered as plane wave. However, the size of Fresnel zone and the magnitude of the impedance discontinuities would affect the wavelet invariance assumption.

Comparing equations (1) and (4), we note a similar structure of the mathematical description of the models in terms of unknown subsurface structure and approximated source wavelets. We therefore adapt the multichannel deconvolution approach to the deconvolution calculation of receiver function traces. Unlike the common practice of receiver function deconvolution, the source wavelet is treated as an unknown element in this blind deconvolution system. Specifically, for a dense array with M stations, $N \times M$ observations of horizontal component data are produced

when a number of N events are recorded by this array. Then, the equation of the wavelet, receiver function and observations can be expressed in time and frequency domain (Eq. 6 & 7).

$$\mathrm{h_{nm}(t)} = \mathrm{w_n(t)} * \mathrm{rf_m(t)} \quad \text{Eq. 6}$$

$$\mathrm{H_{nm}(f)} = \mathrm{W_n(f)} \cdot \mathrm{RF_m(f)} \quad \text{Eq. 7}$$

The inversion of the multichannel blind deconvolution equation system is performed in frequency domain with respect to real and imaginary parts. The theoretical model S of a receiver function can be, then, explicitly rewritten into real (superscripting with R) part and imaginary (superscripting with I) part (Eq. 8 & 9).

$$S^R(W_n, R_m) = W_n^R \cdot RF_m^R - W_n^I \cdot RF_m^I \quad \text{Eq. 8}$$

$$S^I(W_n, R_m) = W_n^R \cdot RF_m^I + W_n^I \cdot RF_m^R \quad \text{Eq. 9}$$

The equation system is overdetermined when either N or M is greater than 2, and, accordingly, can be solved through linearization regarding unknowns. The differences between the theoretical model S and the observation H are described by Eq. 10 & 11. For each frequency component of the unknowns ($\mathrm{W_n}$, $\mathrm{R_m}$), the real part and imaginary part of the spectrum are linearized, respectively (Eq. 12 & 13).

$$\Delta S_{nm}^R = H_{nm}^R - S^R(W_{n0}^R, W_{n0}^I, RF_{m0}^R, RF_{m0}^I) \quad \text{Eq. 10}$$

$$\Delta S_{nm}^I = H_{nm}^I - S^I(W_{n0}^R, W_{n0}^I, RF_{m0}^R, RF_{m0}^I) \quad \text{Eq. 11}$$

$$\Delta S_{nm}^R = \frac{\partial S^R}{\partial W_n^R} \cdot \Delta W_n^R + \frac{\partial S^R}{\partial W_n^I} \cdot \Delta W_n^I + \frac{\partial S^R}{\partial RF_m^R} \cdot \Delta RF_m^R + \frac{\partial S^R}{\partial RF_m^I} \cdot \Delta RF_m^I \quad \text{Eq. 12}$$

$$\Delta S_{nm}^I = \frac{\partial S^I}{\partial W_n^R} \cdot \Delta W_n^R + \frac{\partial S^I}{\partial W_n^I} \cdot \Delta W_n^I + \frac{\partial S^I}{\partial RF_m^R} \cdot \Delta RF_m^R + \frac{\partial S^I}{\partial RF_m^I} \cdot \Delta RF_m^I \quad \text{Eq. 13}$$

The partial derivatives are given by differentiation of Equation 8 and 9

$$\frac{\partial S^R}{\partial W_n^R} = RF_m^R \quad \text{Eq. 14}$$

$$\frac{\partial S^R}{\partial W_n^I} = -RF_m^I \quad \text{Eq. 15}$$

$$\frac{\partial S^R}{\partial RF_m^R} = W_n^R \quad \text{Eq. 16}$$

$$\frac{\partial S^R}{\partial RF_m^I} = -W_n^I \quad \text{Eq. 17}$$

$$\frac{\partial S^I}{\partial W_n^R} = RF_m^I \quad \text{Eq. 18}$$

$$\frac{\partial S^I}{\partial W_n^I} = RF_m^R \quad \text{Eq. 19}$$

$$\frac{\partial S^I}{\partial RF_m^R} = W_n^I \quad \text{Eq. 20}$$

$$\frac{\partial S^I}{\partial RF_m^I} = W_n^R \qquad \text{Eq. 21}$$

Accordingly, the linearized equations (Eq. 12 & 13) can be formulated in matrix notation:

$$\mathbf{B} \cdot \mathbf{x} = \mathbf{y} \qquad \text{Eq. 22}$$

where $\mathbf{x}$ is the vector of model parameter updates ($\Delta W_n^R, \Delta W_n^I, \Delta RF_m^R, \Delta RF_m^I$), $\mathbf{y}$ contains the reduced observations ($\Delta S_{nm}^R, \Delta S_{nm}^I$), and $\mathbf{B}$ consists of the partial derivatives.

To exploit the coherency of dense-array RF and to stabilize the inversion, continuity constraints on the amplitude and phase of the RFs are added to the equation system. Amplitude and phase are considered as invariant among adjacent stations. The continuity equations (Eq. 23 & 24) are appended to the Equation 22, in form of a matrix $\mathbf{C}$ and misfits $\boldsymbol{\tau}$, $\boldsymbol{\varphi}$ (Eq. 25) in the exact same form as in Behm & Shekar (2014). The relative weight of the continuity constraints and their exact spatial behavior can be specified by weighting factors.

$$\Delta\tau_{AB} = \tau_A - \tau_B = \sqrt{(R_A^R + R_A^I)^2} - \sqrt{(R_B^R + R_B^I)^2} = 0 \qquad \text{Eq. 23}$$

$$\Delta\varphi_{AB} = \varphi_A - \varphi_B = tan^{-1}\left(\frac{R_B^I}{R_B^R}\right) - tan^{-1}\left(\frac{R_A^I}{R_A^R}\right) = 0 \qquad \text{Eq. 24}$$

$$\begin{bmatrix} \boldsymbol{B} \\ \boldsymbol{C} \end{bmatrix} \cdot \boldsymbol{x} = \begin{bmatrix} \boldsymbol{y} \\ -\Delta\boldsymbol{\tau} \\ -\Delta\boldsymbol{\varphi} \end{bmatrix} = \boldsymbol{D} \cdot \boldsymbol{x} = \boldsymbol{y'} \qquad \text{Eq. 25}$$

Finally, the Eq. 25 is solved for $\mathbf{x}$ by the least-squares solution:

$$\boldsymbol{x} = (\boldsymbol{D^T} \cdot \boldsymbol{D})^{-1} \cdot \boldsymbol{D^T} \cdot \boldsymbol{y'} \qquad \text{Eq. 26}$$

The initial model of source wavelet (W_{n0}^{R}, W_{n0}^{I}) is assumed as stacking average of vertical component and the initial model of receiver function (RF_{m0}^{R}, RF_{m0}^{I}) is assumed as zero conversions. Starting from this initial model, the least-square solution of the unknowns is, then, obtained through iterations of deriving model updates. Details of inversion parameters are introduced in the following sections.

3.4 Forward modeling of local earthquakes

Local earthquake data are commonly utilized for subsurface imaging through either tomography methods or reflection imaging methods (Calkins et al., 2006; Bao et al., 2021; Dangwal and Behm, 2021; Ratre and Behm, 2021). However, there are significant challenges associated with receiver function analysis using local events. One of the challenges of local earthquake receiver function is the masking of the primary conversion phase by reverberations in the sedimentary rocks. Another concern about identification of the conversion phase is that the converted S-wave from shallow discontinuity may be obscured by the direct P-wave arrival.

To assess the feasibility of local earthquake receiver function, synthetic local earthquake data (waveform) is applied using raytracing with the ANRAY modelling package (Figure 3.3; Gajewski & Pencik, 1987). The synthetic ray-tracing amplitudes of the radial and vertical components were calculated for receivers with varying epicentral distance from the source. The source is located at a depth of 5 km on a two-layer velocity model (Figure 3.3c). The depth of the discontinuity interface in the two-layer model is set at 2 km, with reference to the average basement depth in Oklahoma. The epicentral distance from the receivers to the source ranges between 100 – 300 km with 50 km spacing. As the dominant frequency of local earthquakes ranges between 2-10 Hz

(Archuleta and Ji, 2016), the synthetic waveform at five receivers was derived from the convolution of the ray-tracing amplitude and an 8 Hz minimum-phase Gabor wavelet. The velocity model is based on recently derived seismic models of Oklahoma (Ratre and Behm, 2021), assuming Vp/Vs ratio as 2.5 (Ratre, 2021) for the sedimentary section, while the sedimentary velocities follow a gradient function that represent an average velocity model of Oklahoma sediment column (Darold et al., 2015).

We present the synthetic waveform for 2.5 s after the direct P arrival on vertical and radial component, which contains primary conversion Ps and reverberation phase (surface-related multiple P-reflection) PpP associated with the sedimentary column and sediment-basement impedance contrast. Our results show the presence of a converted S-wave at both vertical and radial components, occurring at approximately 0.5 seconds after the P-arrival. Notably, the radial component exhibits a substantially larger amplitude for the conversion phase compared to the subsequent reverberations, indicative of a robust conversion occurring at the sediment-basement interface. Also, the conversion phase is well-isolated both from the direct P wave arrival and reverberation phases.

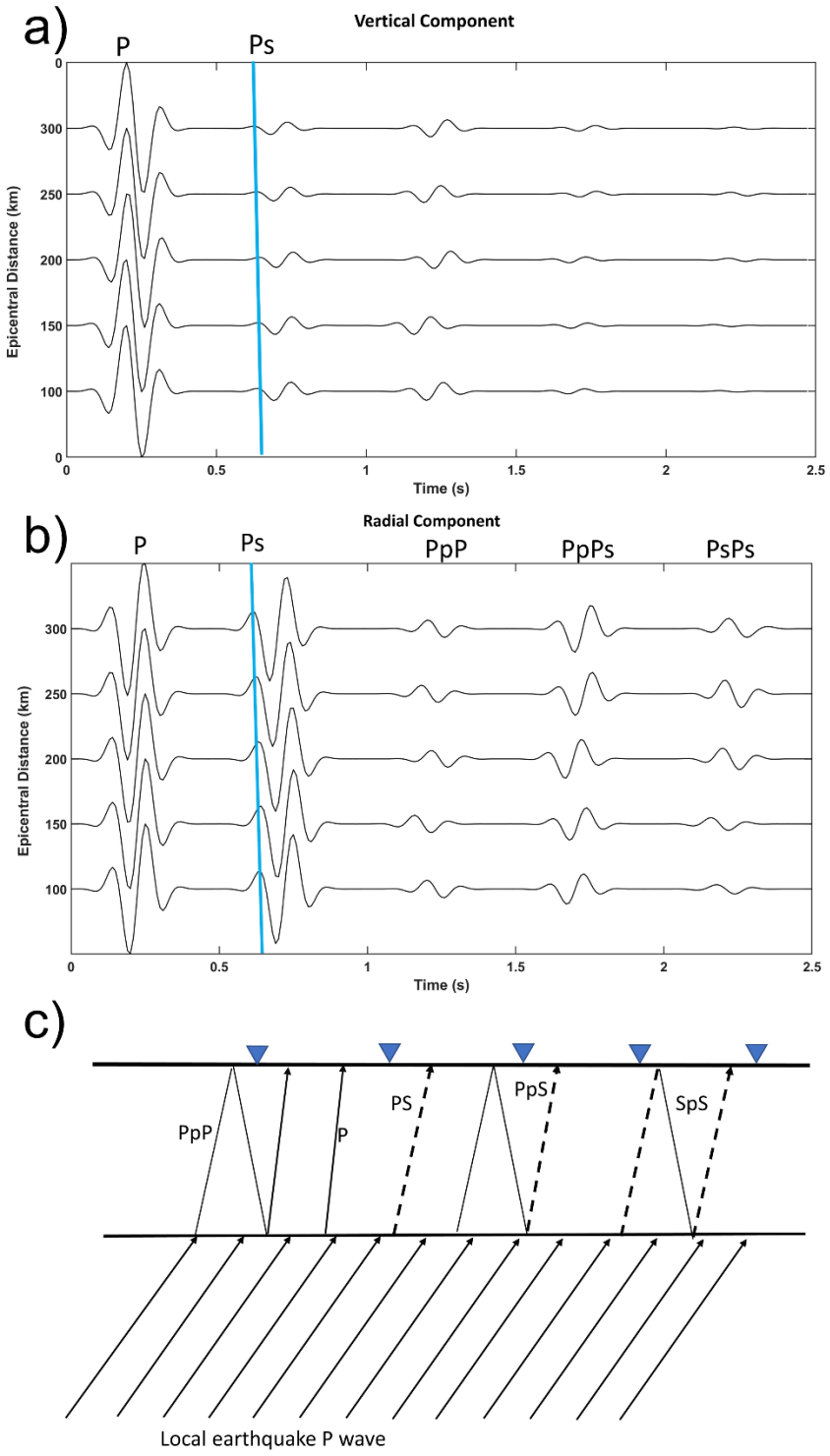


Figure 3.3 Synthetic waveform of local earthquakes and diagram of wave propagation at receiver side. a) Synthetic vertical component of local earthquakes at five receivers with different epicentral

distance b) Synthetic radial component of local earthquakes at five receivers with different epicentral distance c) Wave propagation diagram with phases that are considered in the synthetic waves. Note that the dashed line represents converted S-wave.

3.5 Application of the blind receiver function methodology to real data

In this study, we apply the blind multichannel deconvolution to a dataset collected by a dense-spaced nodal array at Cushing, Oklahoma to image the basement-sediment interface in a fault zone. In 2015, more than 100 shallow earthquakes ruptured in a basement fault system several kilometers west of Cushing, a historically low-seismicity area in central Oklahoma(Deng, Liu and Chen, 2020). The seismicity sequence reveals a previously undetected N60E striking fault, which, following the 2015 sequence, ruptured the Mw 5.0 earthquake on November 7th, 2016, and its aftershocks(Deng, Liu and Chen, 2020; Qin et al., 2022). We deployed a nodal array in 2021 at East Cushing to investigate the fault structure and local induced seismicity (Wang & Behm, 2020). Local and regional small to moderate earthquake events recorded by this nodal array are used for receiver function analysis to image the basement interface and fault displacement at the basement using blind multichannel deconvolution.

3.5.1 Area and geology

Cushing, located at central north Oklahoma, is a major hub of U.S. crude oil and gas storage and transportation where multiple pipelines intersect (McNamara et al., 2015). Though situated at a tectonically quiet area, Cushing has received attention from seismological community after the

occurrence of Mw 4.0 and Mw 4.3 earthquake in 2014, which reactivated a complex conjugate fault system in the shallow subsurface of Pawnee County(McNamara et al., 2015; Qin et al., 2022). Another fault system is revealed by a sequence of basement earthquakes at the west of Cushing town in 2015. The earthquake sequence originated at a depth of approximately 3.8 km, where ruptured the M5.0 event in 2016 as well as some earliest seismicity of this sequence (Qin et al., 2022). The current understanding of the fault zone is largely based on relocated earthquake hypocenters, showing a narrow vertical fault zone trending N60°E, with few secondary faults (Deng, Liu and Chen, 2020; Qin et al., 2022). Studies of the earthquake source mechanism with injection records suggest a correlation between the earthquake rupturing and fluid injected into the Arbuckle formation (McGarr and Barbour, 2017; Yeck et al., 2017; Ratre, 2021; Qin et al., 2022).

The crust of the US midcontinent formed through a series of accretion from 1.5 Ga to 1 Ga, while the basement of Oklahoma was generated by Mazatzal Orogeny 1.65-1.6 Ga, composed of highly crystalized Granite and Rhyolite(Bickford et al., 2015; Wang et al., 2023). While exposed at southern Oklahoma, the crystalline basement is broadly overlain by sedimentary rocks deposited from Cambrian to Pennsylvanian with the post-Pennsylvanian rocks eroded (Kolawole, Simpson Turko and Carpenter, 2020; Caf, 2022). Particularly, the Arbuckle group, deposited during the Cambrian and Ordovician periods, is situated atop the Precambrian basement(Elebiju et al., 2011; Ansari, Bidgoli and Hollenbach, 2019; Deng et al., 2021). The basement depth to surface varies substantially from the Anadarko basin to shelf-to-platform geological provinces in northeast Oklahoma while the depth to basement top at Cushing is around 1.1 km (Crain and Chang, 2018).

3.5.2 Data

In this study, the data used for multichannel blind deconvolution is from a dense spaced nodal array deployed at west Cushing, right above the fault that ruptured the Mw 5.0 earthquake in Dec 2016 (Figure 3.4). The array is composed of 130 3C ZLAND nodes, deployed in a grid pattern along roads, with 200m and 250m station spacing. The nodes have a corner frequency of 5 Hz but were shown to be sensitive down to 0.2 Hz (Ringler et al., 2018). The deployment provided a continuous data set from Nov 5th, 2019, to Dec 16th, 2019.

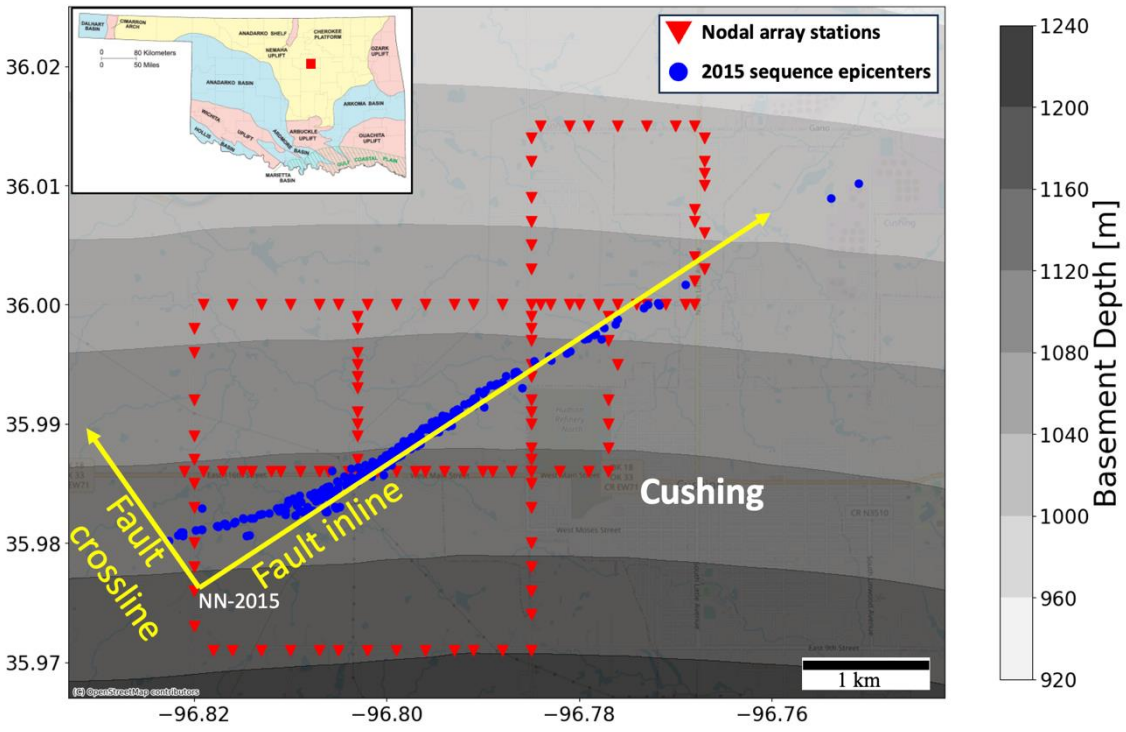


Figure 3.4 Map view of Cushing nodal array and 2015 earthquake sequence overlaid by basement depth. The background is the basement depth map derived from basement penetrating wells (Northcutt and Campbell, 1996). Two coordinate axes (inline, crossline) used in the following figures are plotted in yellow arrows.

Following the Oklahoma Geological Survey catalog, we prescreened the waveform of small to medium magnitude (Mw 2.0 to Mw 5.0) earthquake events whose epicenter distance to the nodal array is in range of 100 km to 500 km. The main criteria for event selection are that the P-wave and converted S-wave phases have a high signal-to-noise ratio. Following this criterium, 23 regional and local earthquakes are selected for receiver function analysis (Figure 3.5, Table. 3-1).

Table 3-1 Local and regional events information

Longitude	Latitude	Depth (km)	Magnitude (Mw)	Date	Time	Distance (km)	Back-Azimuth
-97.406	34.381	5.2	2.7	11/9/2019	10:22:17	185.2475405	197
-95.376	35.136	5.9	2.8	11/10/2019	11:00:32	157.8058264	125
-95.373	35.14	4.7	2.6	11/10/2019	19:58:31	157.7637823	125
-98.161	36.307	6.1	2.7	11/10/2019	20:50:46	129.3359003	287
-96.902	38.395	5	3	11/10/2019	23:21:11	269.2186977	357
-97.64	36.274	7.2	2.6	11/12/2019	6:35:15	83.99274668	293
-95.37	35.138	5.9	2.8	11/13/2019	20:35:31	158.115445	125
-97.708	36.369	8.8	3.6	11/21/2019	5:44:36	94.05441079	298
-95.354	35.133	6.6	2.7	11/21/2019	16:04:08	159.6204301	125
-98.191	36.294	6.2	3.7	11/21/2019	21:54:05	131.5333346	286
-98.188	36.291	6	3.6	11/21/2019	21:54:49	131.1853681	286
-98.068	35.852	6	2.8	11/26/2019	15:43:07	116.5585316	263
-96.181	34.472	5	2.6	11/27/2019	11:39:42	175.1600874	161
-95.385	35.109	6.8	2.6	11/28/2019	13:43:06	158.9471979	126
-97.797	37.502	2.2	2.9	11/29/2019	7:34:06	192.4439556	332
-97.802	37.508	5	2.5	11/29/2019	9:50:31	193.2399175	332
-97.813	37.511	5	2.6	11/29/2019	18:20:07	193.9959751	332
-95.367	35.135	6.2	2.7	11/29/2019	23:38:49	158.5326431	125
-95.412	35.165	20.2	2.6	11/30/2019	21:56:36	153.2582246	125
-95.327	35.14	6.8	3.1	12/2/2019	21:36:15	161.166355	124
-98.176	36.291	5.6	2.8	12/2/2019	22:22:03	130.1458746	286

-98.152	36.363	6.1	2.8	12/4/2019	14:30:22	130.4567665	289
-98.15	36.359	6.3	3	12/4/2019	14:31:16	130.1425786	289

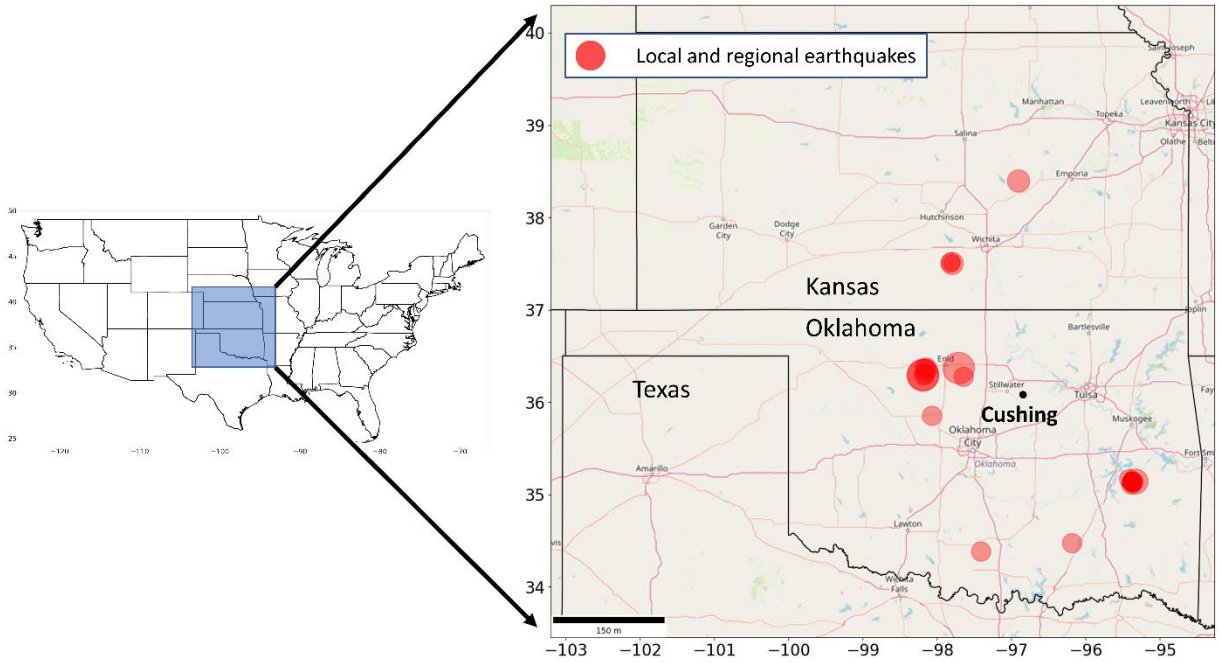


Figure 3.5 Map view of local and regional events used in this study. Earthquake events are plotted in red circles in different sizes which represent the relative magnitude of each event.

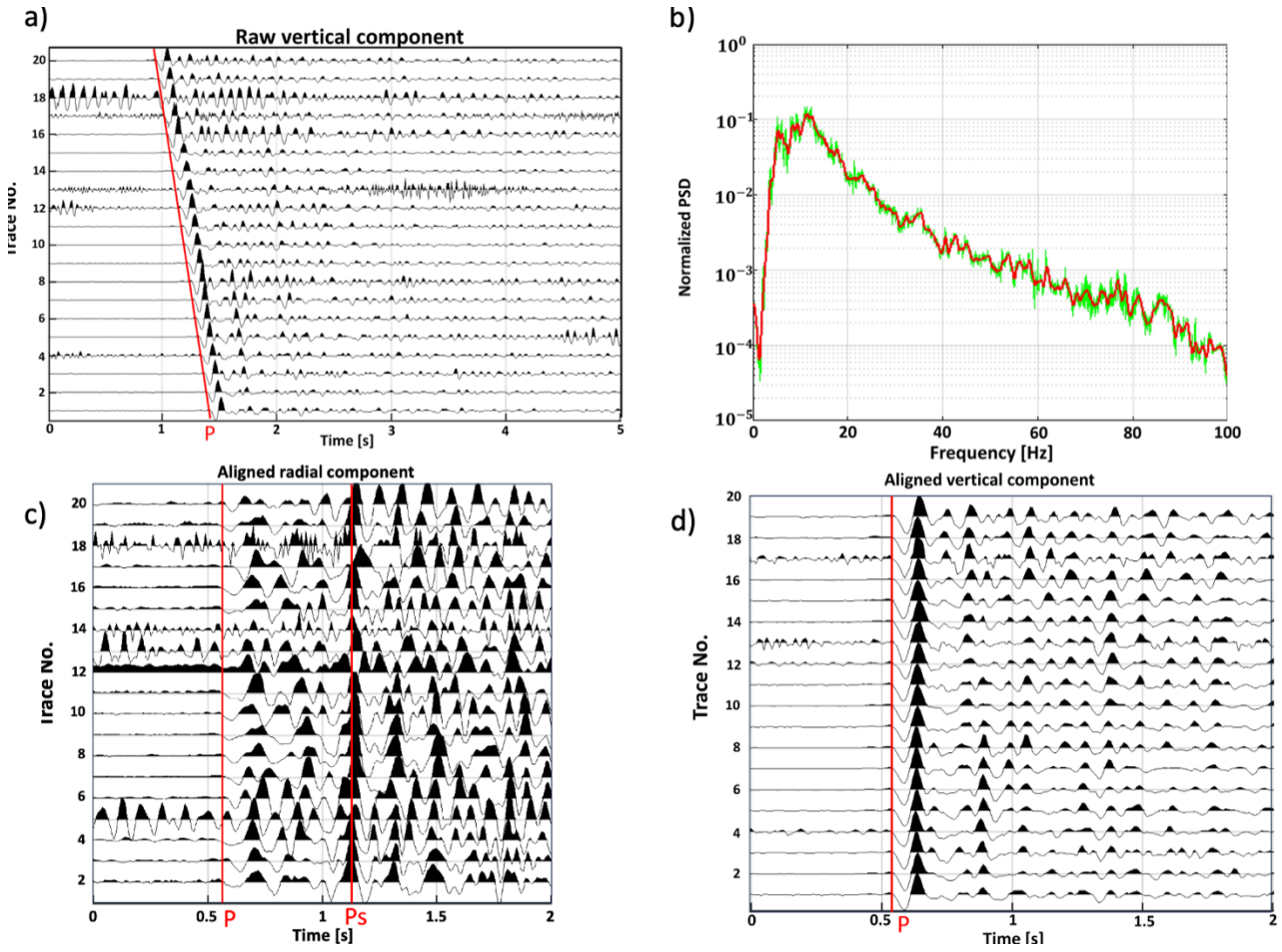


Figure 3.6 An example of a local earthquake recorded by selected stations of the Cushing array. Event information: epicentral distance: 1.01 degrees; Magnitude: 2.8 (Mw) a) Raw vertical component of this event. b) Normalized power spectral density of this event. The power spectral density of each single trace in a) present green lines while the red line indicates average power spectral density of all selected traces c) Aligned radial component of this event raw vertical component of this event. D) Aligned vertical component of this event.

3.5.3 Application and results

Using the local earthquake data recorded by the Cushing Array, we applied the multichannel blind deconvolution approach to obtain the receiver functions below each node to provide insight into the basement structures of the Cushing fault zone.

To ensure the performance of multichannel blind deconvolution on regional and local earthquakes, the events underwent a series of pre-processing procedures: 1) The north and east component of each event is rotated to radial component with the back azimuth. 2) A Butterworth bandpass filter (1-15 Hz) is applied to the vertical and radial component as the dominant frequency of the local and regional earthquake body waves is 2-10 Hz. 3) Vertical and radial components are aligned with respect to the arrival time of the direct P arrival, e.g., the P-wave onset is picked on all traces, and within each event gather all traces are shifted by the time difference of the pick and the earliest arrival time in the gather.

The inversion process for wavelet and receiver function entails deriving the least square solution of Eq 24, wherein the parameters of the real and imaginary components of the wavelet and receiver function are represented in the **x** vector. The inversion process for the receiver function begins with a zero-conversion model. The inversion applies singular value decomposition to the matrix **D**, where only eigenvectors are used where the ratio of the associated singular value to the largest singular value is larger than 0.1. The inversion process comprises 30 iterations, with the model being updated at each iteration. Prior to adding an update to the previous model, a damping factor of 0.2 is applied to the update at each step. The weight assigned to the source wavelet model is 0.1, while the conversion model has a weight of 1. Additionally, assuming little variation of the

basement structure across the short distance covered by the array, a conversion continuity constraint is imposed, with an amplitude weight of 0.1 and a phase weight of 1.

The multichannel blind deconvolution inversion produces a single receiver function at each node which represents a conversion model beneath this station. As the Cushing nodal array is deployed in grid configuration above the earthquake sequence cluster, we present the receiver function results of all stations in relation to the fault strike (Figure 3.7 & Figure 3.8). Given the indications from previous investigations on the relocated hypocenters of the Cushing fault sequence, which suggest a sub-vertical fault plane with strike-slip motion, we proceed to approximate the fault trace as a linear path depicting the hypocenters cluster on the map view (Figure 3.4). We mainly examine the receiver function results in pseudo-cross-sectional plots, specifically with respect to the relative positioning of the stations and the fault strike. For every node, an in-line distance is determined by projecting the node onto a vertical plane parallel to the fault strike, which is represented as a linear path. The start of this "fault inline axis" is chosen to coincide with the node station NN-2015 in the southwestern corner of the array (Figure 3.4). Accordingly, a crossline distance is calculated as the perpendicular distance from the node to the inline axis, where positive crossline distances are north of the fault and negative distances correspond to the southern side of the fault.

Figure 3.7 shows the pseudo-cross-section with receiver function time series sorted by crossline distance. Negative values correspond to nodes located on the northwestern side of the fault trace, while positive values indicate nodes situated on the southeastern side of the fault. The RF traces at crossline distance 0 around the center of the cross-section are situated at the fault. The dominant feature is characterized by a phase with positive amplitude at an average delay time of 0.5s. Figure 3.8 shows the pseudo-cross-section with RF sorted by in-line distance. The clear positive

conversion phase with delay time of ~0.5s implies the presence of an impedance contrast with higher impedance beneath it.

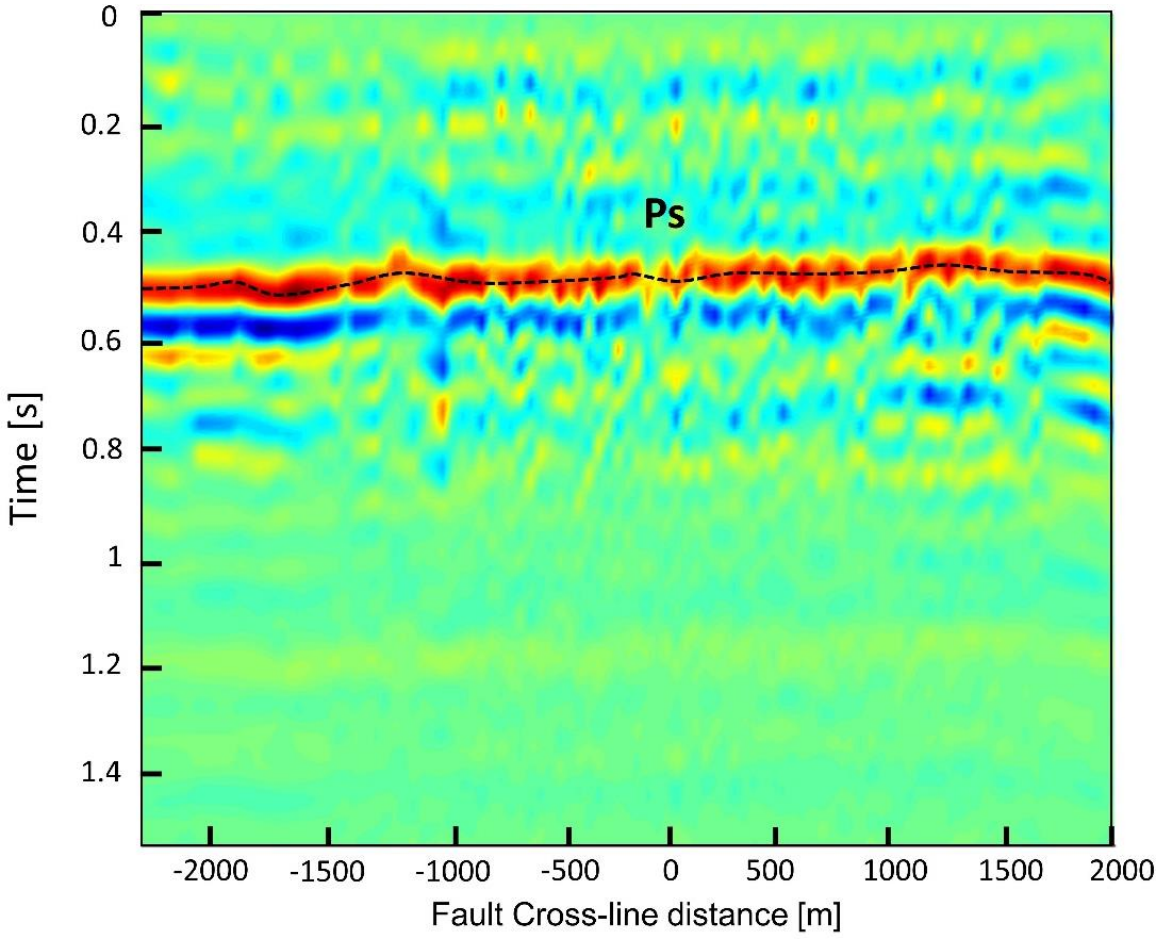


Figure 3.7 Projection of all blind RFs on a vertical plane perpendicular to the fault strike (see yellow axes in Figure 3.4). Note the prominent P-to-S conversion that is marked by dashed line.

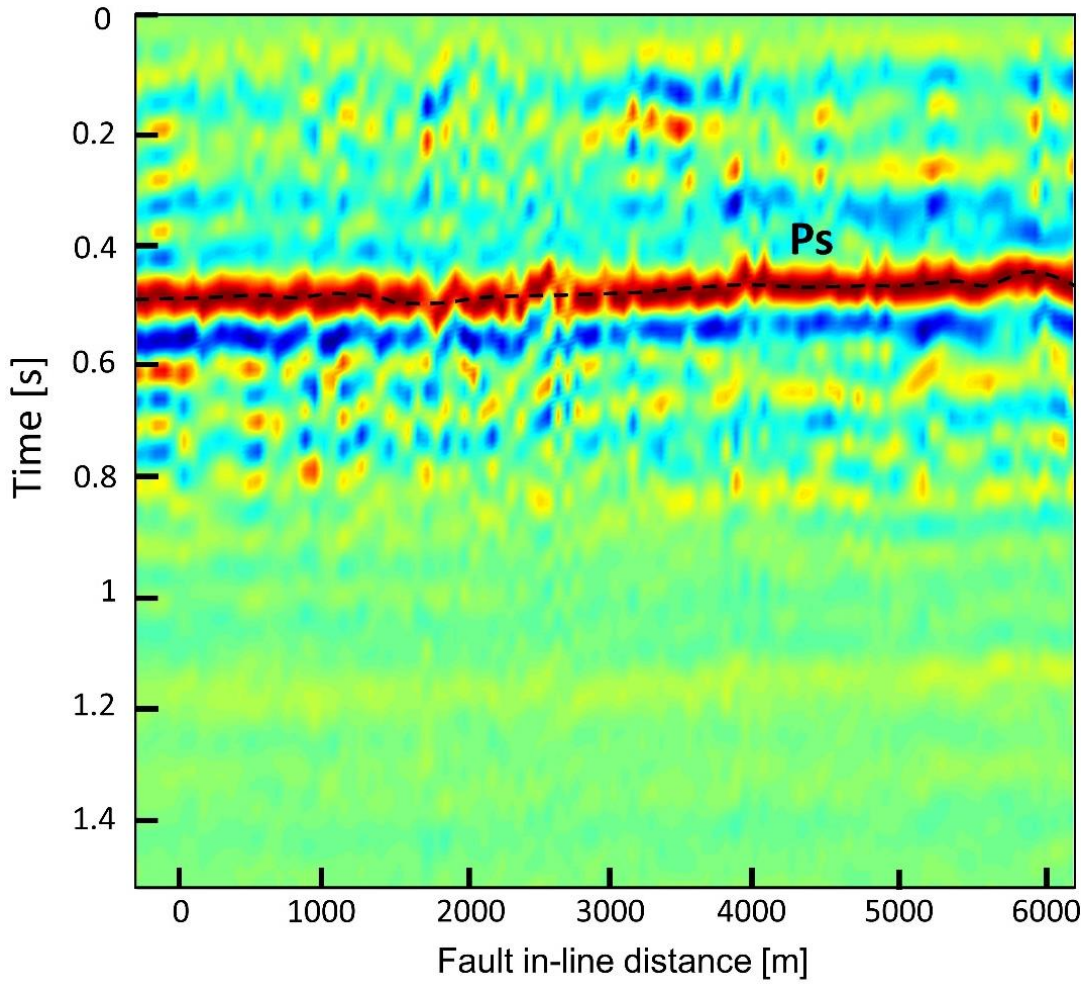


Figure 3.8 Projection of all blind RFs on a vertical plane parallel to the fault strike (see yellow axes in Figure 3.4). Note the prominent P-to-S conversion that is marked by dashed line.

Oklahoma Geological Survey provides a regional depth map of the pre-Cambrian basement mainly derived from well data (Crain and Chang, 2018). There is no basement-penetrating well in the Cushing area, and the basement depth contour presented in Figure 3.4 is based on interpolation of nearby wells. According to this regional basement depth map, the thickness of the Cambrian to Pennsylvanian sedimentary sequence amounts to ca. 1.2 km in the Cushing area. Studies on earthquake relocation (Qin et al., 2022) suggests a high Vp/Vs ratio (2.5 for sedimentary layer) for

the sedimentary stack at central Oklahoma (Ratre, 2021). Using this Vp/Vs ratio, we convert the conversion times according to Eq. 27.

$$H = t_{ps} * \left(\frac{1}{\sqrt{\frac{1}{{V_p}^2} - rayp^2}} - \frac{1}{\sqrt{\frac{1}{{V_s}^2} - rayp^2}}\right) \quad \text{Eq. 27}$$

Where rayp stands for the ray parameter of direct P wave and H represents the conversion depth. A raw estimation of the conversion depth can be derived from the Eq. 27 by taking ray parameter 0.00216 s/deg for an average crustal model and average epicentral distance of 180.2 km and sedimentary Vp of 3.5 km/s with 2.5 Vp/Vs ratio(Ratre, 2021; Tan, Langston and Ni, 2021). According to this velocity model, a RF conversion phase at 0.5 seconds corresponds to a depth of 1.18 km, which fits remarkably well with the basement depth map by OGS(Figure 3.9; Crain and Chang, 2018). Also, the shallowing trend towards the north in the basement depth map is reflected in the RF inline section. Therefore, we interpret the dominant positive conversion phase as the top of the pre-Cambrian basement.

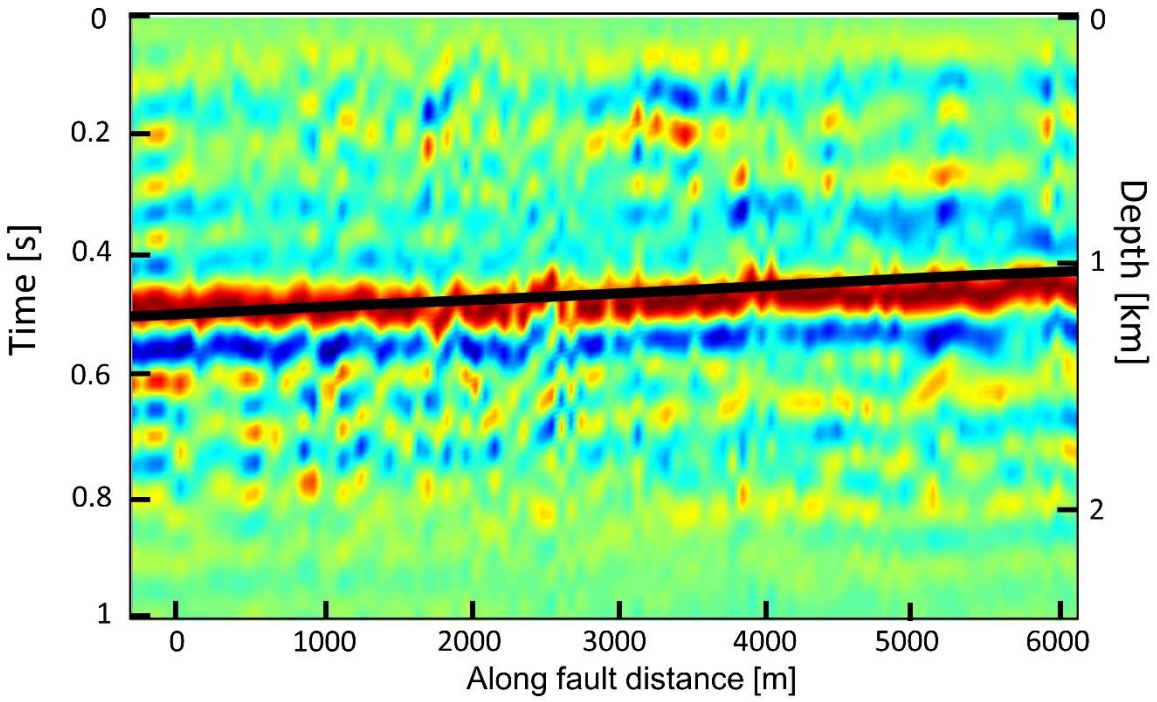


Figure 3.9 Zoomed projection of all RFs by in-line fault distance with extracted basement depth (solid black line) from OGS basement map (Figure 3.4). Depth derived from the velocity model mentioned in the text is labeled on the ride side of this pseudo-cross-section.

3.6 Discussion

3.6.1 Shallow RF imaging with local earthquakes

The results obtained from the blind receiver function analysis clearly show a distinct primary P-to-s conversion phase. Based on synthetic modelling and regional basement depth maps, we interpret this conversion as the upper boundary of the Pre-Cambrian crystalline basement. Previous RF studies on high-resolution imaging using receiver function have investigated different approaches to identify the shallow high-frequency conversion from the teleseismic low-frequency

P-wave coda (Leahy, Saltzer and Schmedes, 2012; Licciardi and Agostinetti, 2017; Liu, Persaud and Clayton, 2018; Subašić, Agostinetti and Bean, 2019; Subašić, Piana Agostinetti and Bean, 2020). These approaches push the capability of imaging shallow crust using teleseismic receiver functions. However, the lack of high-frequency components remains an inherent issue in teleseismic receiver function analysis.

The converted teleseismic body wave generated from shallow crustal impedance discontinuities is typically concealed within the P-wave coda (Wang et al., 2023). Consequently, the associated conversion phase can be masked by the P arrival peak in conventional receiver function waveforms. Furthermore, compared to the conversion of prominent discontinuities (e.g., Moho, midcrustal discontinuity), the primary conversion generated from shallow impedance discontinuity in RF exhibits lower amplitude due to minor impedance contrasts, making it susceptible to interference with noise (Cassidy, 1992).

While regional and local earthquake events are commonly employed in other seismological methods like seismic tomography and surface wave tomography, there have been few attempts to utilize non-teleseismic events in receiver function studies. The exception is found in some studies focused on subduction zones(Phillips et al., 2012; Phillips and Clayton, 2014; Ryan et al., 2016), where local events at sufficient depth (50-100 km) can generate near-vertical incident conversion waves at the Moho and subduction zone.

Under general conditions, there are three concerns regarding the use of local events in receiver function studies. Firstly, local events usually rupture at shallow depths, resulting in ray paths that do not penetrate deep into the mid-to-lower crust. Therefore, the local or regional P-wave coda does not capture deeper conversions. Additionally, the relatively large incident angle associated with local events raises concerns, as receiver functions are presumed to represent structures

beneath the receiver when up-coming P-wave follows a near-vertical ray path. Thirdly, the inclusion of the high-frequency component of local and regional earthquake events results in increased levels of uncertainty within the deconvolution algorithm, as it incorporates the combined response of the local geology heterogeneity and the high-frequency noise. The uncertainties, which cannot be contained simply by frequency-based filter, introduce instability to the algorithm and, hence, lead to confusions for interpretation. The first two concerns related to the ray path geometry and depth coverage of receiver function analysis can be significantly mitigated when investigating basin-scale structures near the surface and basement upper boundary, as the incident wave from local and regional event can be considered subvertical in the upper most basement. The third concern can be well resolved using multichannel blind deconvolution, as the unknown source wavelets and RF are inverted simultaneously with a model approach which effectively projects random noise to a larger data misfit. Additionally, random-noise-induced spurious phases are suppressed by the horizontal continuity constraint in this dense-spaced network geometry. Consequently, the basement top interface of the study area is well depicted by the multichannel blind deconvolution approach applied to local and regional earthquakes.

3.6.2 Cushing Fault structure

The most common application of teleseismic receiver function is to investigate horizontally layered subsurface discontinuities. Subvertical-faults may only be clearly seen in RFs if the fault zone is broad or associated with a significant vertical fault offset. Few receiver function studies can infer the geometry of the fault with vertical displacement by examining the amplitude and phase variation of horizontal conversions across the fault (Wilson et al., 2004; Lucente et al., 2005;

Liu, Persaud and Clayton, 2018). However, the geometry of large-scale low-angle shear zones, such as subduction zone and thrust, which give rise to notable impedance contrast, can be inferred through the analysis of direct conversion signals generated at the interface(Li et al., 2003; Schulte-Pelkum and Mahan, 2014; Park and Levin, 2016; Cheng et al., 2017; Ward, Lin and Schmandt, 2018).

The depth of relocated hypocenters of the Cushing M5 earthquake sequence ranges from 5 km – 3 km, indicating failures in the pre-Cambrian crystalline basement (Deng, Liu and Chen, 2020). The focal mechanism analysis suggests a N60°E left-lateral strike-slip pattern which agrees with the near-East-West maximum horizontal stress at this area(Qin et al., 2019, 2022). However, a segment at the northeast part of the main fault exhibits more normal faulting components (Qin et al., 2022). Figures 3.10, 3.11, and 3.12 illustrate the receiver functions obtained from two east-west paths and a north-south path that intersect the fault surface projection at an oblique angle. With an assumed P-wave velocity of 3000m/s in the sedimentary layers, the multichannel blind RF technique can achieve an estimated vertical resolution of approximately 30 meters. This resolution is achieved when utilizing local earthquakes with a dominant frequency of 10 Hz. This observation implies that there is no substantial vertical displacement occurring on the top of the basement across the fault zone under the current resolution of blind RFs.

Figure 3.13 shows the relative location between the relocated hypocenters and the crossline blind RF pseudo-cross-section, which is labeled with estimated depth, assuming an average Vp/Vs ratio of 2.5 (Ratre, 2021) and an average Vp of 3.5 km/s (Tan, Langston and Ni, 2021). It is noted that this depth conversion is only valid for the section above the converter, as the higher basement velocities are not incorporated due to the lack of converted energy below the interpreted basement converter. The sub-vertical strike-slip fault is depicted by the sequence cluster. The conversion

phase corresponding to the basement top shows a similar delay time across the array, suggesting that there is no significant displacement of the shallow part of the fault system at the basement. Nonetheless, it is worth noting that the conversion phase directly above the fault displays weaker continuity than the conversion phase further away from the fault zone. This anomaly may indicate the presence of a shear zone extending upward from the ruptured area.

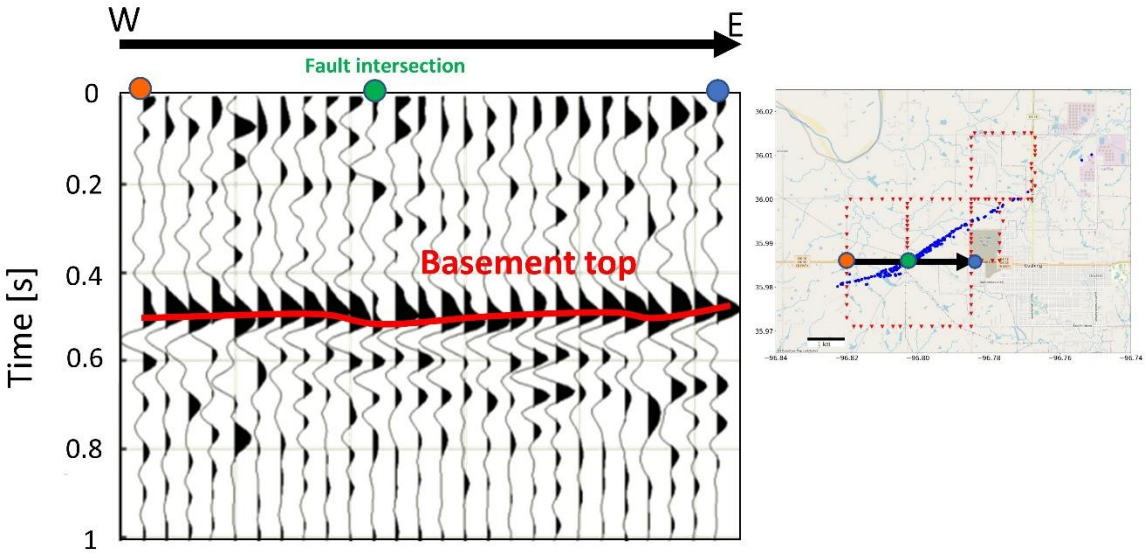


Figure 3.10 Left: RF cross-section of an east-west path in the array. Red line: interpreted basement top conversion. Right: Map view of the array geometry, with black line denoting the cross-section array shown in the left. The red, green and blue circles mark the start station, intersection with the fault strike and end station of the cross-section, respectively.

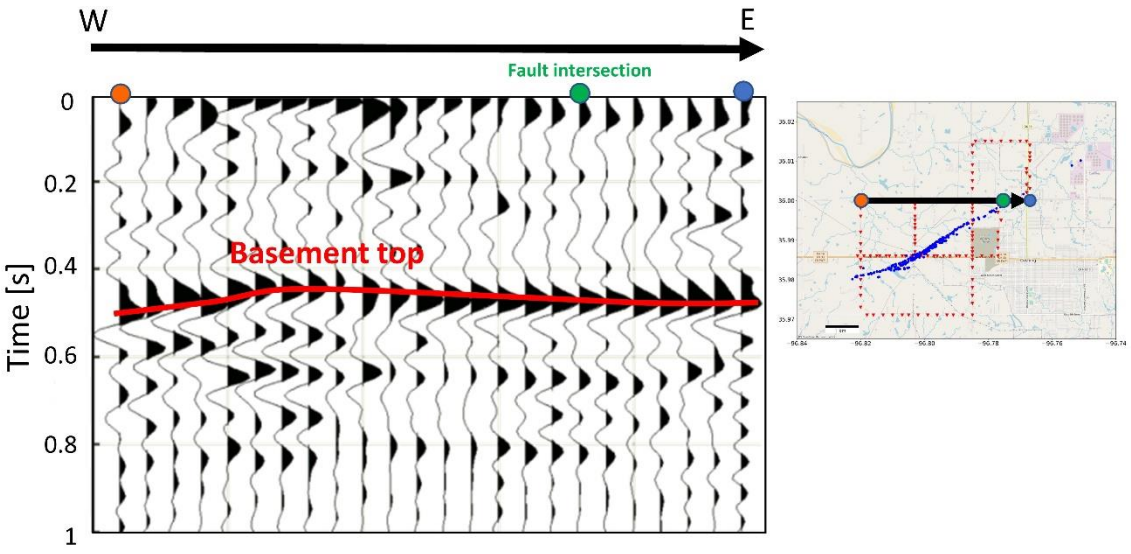


Figure 3.11 Left: RF cross-section of an east-west path in the array. Red line: interpreted basement top conversion. Right: Map view of the array geometry, with black line denoting the cross-section array shown in the left. The red, green and blue circles mark the start station, intersection with the fault strike and end station of the cross-section, respectively.

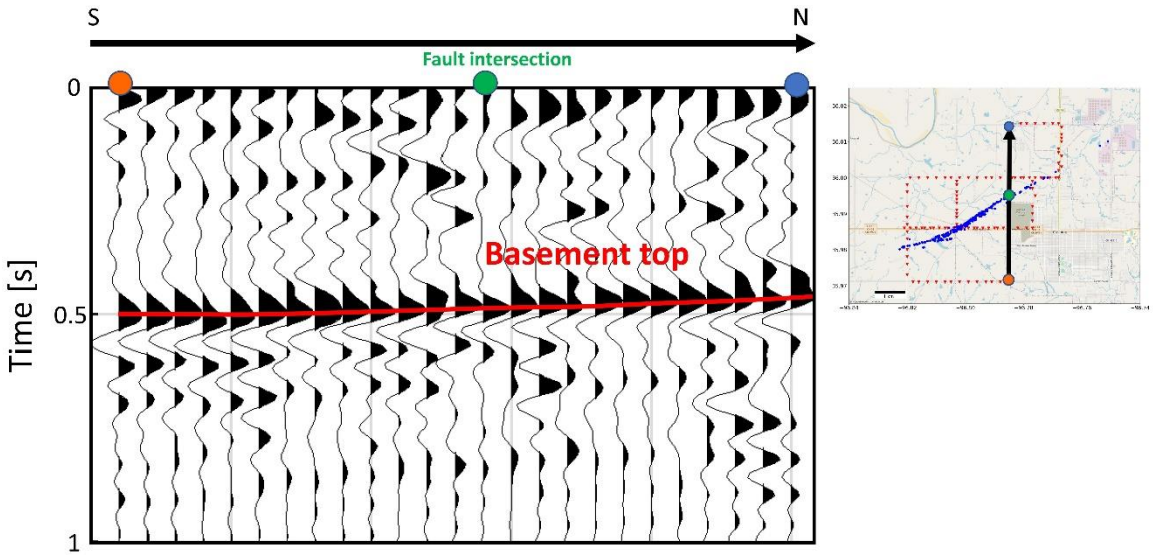


Figure 3.12 Left: RF cross-section of an north-south path in the array. Red line: interpreted basement top conversion. Right: Map view of the array geometry, with black line denoting the cross-section array shown in the left. The red, green and blue circles mark the start station, intersection with the fault strike and end station of the cross-section, respectively.

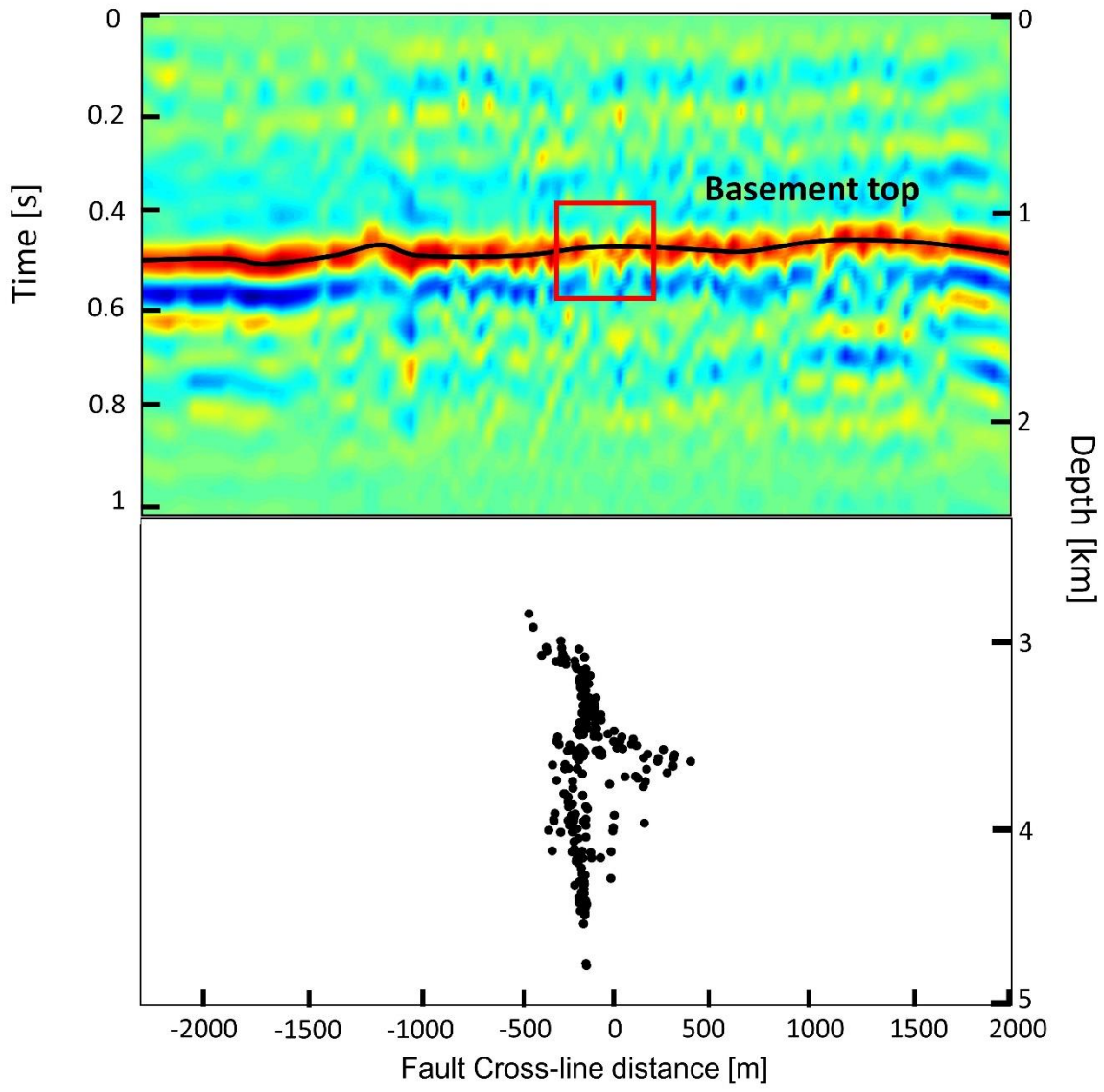


Figure 3.13 Projection of RFs and M5 Cushing sequence hypocenters (black circles) perpendicular to the fault following the diagram in Figure 3.3. Black line: interpreted basement top conversion. Red square box: area of basement conversion right above the vertical fault geometry. Depth derived from the velocity model mentioned in the text is labeled on the ride side of this pseudo-cross-section.

3.7 Conclusion

We developed a multi-channel blind deconvolution routine to calculate the receiver function from the local and regional earthquake. Through synthetic modelling of local and regional earthquakes, we show that the conversion and multiple phases are distinctive in the P-wave coda on both vertical and horizontal components and therefore are feasible for RF analysis. By applying the multichannel blind deconvolution to Cushing nodal array data, we present the resulting RFs by the relative positions of the array nodes in relation to the fault surface projection trace. The RF profiles clearly depict the basement top at around 1.1 km, remarkably matching the previously published basement topography map. Upon analyzing the basement top conversion above the Cushing fault plane, we found that near the upward extension of the fault zone, there is minimal displacement on the conversion phase. This finding indicates that the fault either has negligible vertical displacement or does not extend into the sedimentary layers.

3.8 References

Ansari, E., Bidgoli, T. S., & Hollenbach, A. (2019). Accelerated Fill-Up of the Arbuckle Group Aquifer and Links to U.S. Midcontinent Seismicity. Journal of Geophysical Research: Solid Earth, 124(3), 2670–2683. https://doi.org/10.1029/2018JB016926

Archuleta, R. J., & Ji, C. (2016). Moment rate scaling for earthquakes $3.3 \leq M \leq 5.3$ with implications for stress drop. Geophysical Research Letters, 43(23). https://doi.org/10.1002/2016GL071433

Bao, F., Li, Z., Shi, Y., Tian, B., Chong, J., & Rong, W. (2021). Sediment Structures Constrained by Converted Waves From Local Earthquakes Recorded by a Dense Seismic Array in the Tangshan Earthquake Region. Pure and Applied Geophysics, 178(2), 379–397. https://doi.org/10.1007/s00024-021-02667-5

Bianchi, I., Park, J., Piana Agostinetti, N., & Levin, V. (2010). Mapping seismic anisotropy using harmonic decomposition of receiver functions: An application to Northern Apennines, Italy. Journal of Geophysical Research, 115(B12), B12317. https://doi.org/10.1029/2009JB007061

Bickford, M. E., Van Schmus, W. R., Karlstrom, K. E., Mueller, P. A., & Kamenov, G. D. (2015). Mesoproterozoic-trans-Laurentian magmatism: A synthesis of continent-wide age distributions, new SIMS U–Pb ages, zircon saturation temperatures, and Hf and Nd isotopic compositions. Precambrian Research, 265, 286–312. https://doi.org/10.1016/j.precamres.2014.11.024

Caf, A. (2022). Quantitative seismic interpretation and machine learning applications for subsurface characterization and modeling.

Calkins, J. A., Zandt, G., Gilbert, H. J., & Beck, S. L. (2006). Crustal images from San Juan, Argentina, obtained using high frequency local event receiver functions. Geophysical Research Letters, 33(7), L07309. https://doi.org/10.1029/2005GL025516

Cassidy, J. F. (1992). Numerical experiments in broadband receiver function analysis. Bulletin of the Seismological Society of America, 82(3), 1453–1474. https://doi.org/10.1785/BSSA0820031453

Chen, K.-C., Chiu, J.-M., & Yang, Y.-T. (1994). Qp-Qs relations in the sedimentary basin of the upper Mississippi Embayment using converted phases. Bulletin of the Seismological Society of America, 84(6), 1861–1868. https://doi.org/10.1785/BSSA0840061861

Chen, K.-C., Chiu, J.-M., & Yang, Y.-T. (1996). Shear-wave velocity of the sedimentary basin in the upper Mississippi embayment using S -to- P converted waves. Bulletin of the Seismological Society of America, 86(3), 848–856. https://doi.org/10.1785/BSSA0860030848

Cheng, C., Bodin, T., Tauzin, B., & Allen, R. M. (2017). Cascadia subduction slab heterogeneity revealed by three-dimensional receiver function Kirchhoff migration. Geophysical Research Letters, 44(2), 694–701. https://doi.org/10.1002/2016GL072142

Cheng, F., Xia, J., Ajo-Franklin, J. B., Behm, M., Zhou, C., Dai, T., Xi, C., Pang, J., & Zhou, C. (2021). High-Resolution Ambient Noise Imaging of Geothermal Reservoir Using 3C Dense Seismic Nodal Array and Ultra-Short Observation. Journal of Geophysical Research: Solid Earth, 126(8). https://doi.org/10.1029/2021JB021827

Clayton, R. W., & Wiggins, R. A. (1976). Source shape estimation and deconvolution of teleseismic bodywaves. Geophysical Journal International, 47(1), 151–177. https://doi.org/10.1111/j.1365-246X.1976.tb01267.x

Clouser, R. H., & Langston, C. A. (1991). QP-QS relations in a sedimentary basin using converted phases. Bulletin of the Seismological Society of America, 81(3), 733–750.

Crain, K. D., & Chang, J. C. (2018). Elevation map of the top of the crystalline basement in Oklahoma and surrounding states. Oklahoma Geological Survey Open-File Report.

Dangwal, D., & Behm, M. (2021). Interferometric body-wave retrieval from ambient noise after polarization filtering: Application to shallow reflectivity imaging. GEOPHYSICS, 86(6), Q47–Q58. https://doi.org/10.1190/geo2020-0768.1

Darold, A. P., Holland, A. A., Morris, J. K., & Gibson, A. R. (2015). Oklahoma earthquake summary report 2014. http://ogs.ou.edu/docs/openfile/OF1-2015.pdf

Deng, K., Liu, Y., & Chen, X. (2020). Correlation Between Poroelastic Stress Perturbation and Multidisposal Wells Induced Earthquake Sequence in Cushing, Oklahoma. Geophysical Research Letters, 47(20). https://doi.org/10.1029/2020GL089366

Deng, T., Xu, C., Lang, X., & Doveton, J. (2021). Diagenetic Facies Classification in the Arbuckle Formation Using Deep Neural Networks. Mathematical Geosciences, 53(7), 1491–1512. https://doi.org/10.1007/s11004-021-09918-0

Elebiju, O. O., Matson, S., Keller, G. R., & Marfurt, K. J. (2011). Integrated geophysical studies of the basement structures, the Mississippi chert, and the Arbuckle Group of Osage County region, Oklahoma. AAPG Bulletin, 95(3), 371–393. https://doi.org/10.1306/08241009154

Gajewski, D., & P encik, I. (1987). Computation of high-frequency seismic wavefields in 3-D laterally inhomogeneous anisotropic media. Geophysical Journal International, 91(2), 383–411. https://doi.org/10.1111/j.1365-246X.1987.tb05234.x

Gans, C. R., Beck, S. L., Zandt, G., Gilbert, H., Alvarado, P., Anderson, M., & Linkimer, L. (2011). Continental and oceanic crustal structure of the Pampean flat slab region, western Argentina, using receiver function analysis: new high-resolution results. Geophysical Journal International, 186(1), 45–58. https://doi.org/10.1111/J.1365-246X.2011.05023.X

Kolawole, F., Simpson Turko, M., & Carpenter, B. M. (2020). Basement-controlled deformation of sedimentary sequences, Anadarko Shelf, Oklahoma. Basin Research, 32(6), 1365–1387. https://doi.org/10.1111/bre.12433

Kolb, J. M., & Leki, V. (2014). Receiver function deconvolution using transdimensional hierarchical Bayesian inference. Geophysical Journal International, 197(3), 1719–1735. https://doi.org/10.1093/gji/ggu079

Leahy, G. M., Saltzer, R. L., & Schmedes, J. (2012). Imaging the shallow crust with teleseismic receiver functions. Geophysical Journal International, 191(2), 627–636. https://doi.org/10.1111/j.1365-246X.2012.05615.x

Li, X., Bock, G., Vafidis, A., Kind, R., Harjes, H.-P., Hanka, W., Wylegalla, K., van der Meijde, M., & Yuan, X. (2003). Receiver function study of the Hellenic subduction zone: imaging crustal thickness variations and the oceanic Moho of the descending African lithosphere. Geophysical Journal International, 155(2), 733–748. https://doi.org/10.1046/j.1365-246X.2003.02100.x

Licciardi, A., & Agostinetti, N. P. (2017). Sedimentary basin exploration with receiver functions: Seismic structure and anisotropy of the Dublin Basin (Ireland). Geophysics, 82(4), KS41–KS55. https://doi.org/10.1190/GEO2016-0471.1/SUPPL_FILE/S10.PDF

Ligorría, J. P., & Ammon, C. J. (1999). Iterative deconvolution and receiver-function estimation. Bulletin of the Seismological Society of America, 89(5), 1395–1400. https://doi.org/10.1785/BSSA0890051395

Liu, G., Persaud, P., & Clayton, R. W. (2018). Structure of the Northern Los Angeles Basins Revealed in Teleseismic Receiver Functions from Short-Term Nodal Seismic Arrays. Seismological Research Letters, 89(5), 1680–1689. https://doi.org/10.1785/0220180071

Lucente, F. P., Piana Agostinetti, N., Moro, M., Selvaggi, G., & Di Bona, M. (2005). Possible fault plane in a seismic gap area of the southern Apennines (Italy) revealed by receiver function analysis. Journal of Geophysical Research: Solid Earth, 110(B4). https://doi.org/10.1029/2004JB003187

McGarr, A., & Barbour, A. J. (2017). Wastewater Disposal and the Earthquake Sequences During 2016 Near Fairview, Pawnee, and Cushing, Oklahoma. Geophysical Research Letters, 44(18), 9330–9336. https://doi.org/10.1002/2017GL075258

McGlannan, A. J., & Gilbert, H. (2016). Crustal signatures of the tectonic development of the North American midcontinent. Earth and Planetary Science Letters, 433, 339–349. https://doi.org/10.1016/j.epsl.2015.10.048

McNamara, D. E., Hayes, G. P., Benz, H. M., Williams, R. A., McMahon, N. D., Aster, R. C., Holland, A., Sickbert, T., Herrmann, R., Briggs, R., Smoczyk, G., Bergman, E., & Earle, P. (2015). Reactivated faulting near Cushing, Oklahoma: Increased potential for a triggered

earthquake in an area of United States strategic infrastructure. Geophysical Research Letters, 42(20), 8328–8332. https://doi.org/10.1002/2015GL064669

Park, J., & Levin, V. (2001). Receiver functions from regional P waves. Geophysical Journal International, 147(1), 1–11. https://doi.org/10.1046/J.1365-246X.2001.00523.X/2/147-1-1-FIG017.JPEG

Park, J., & Levin, V. (2016). Anisotropic shear zones revealed by backazimuthal harmonics of teleseismic receiver functions. Geophysical Journal International, 207(2), 1216–1243. https://doi.org/10.1093/gji/ggw323

Persaud, P., Pérez-Campos, X., & Clayton, R. W. (2007). Crustal thickness variations in the margins of the Gulf of California from receiver functions. Geophysical Journal International, 170(2), 687–699. https://doi.org/10.1111/j.1365-246X.2007.03412.x

Phillips, K., & Clayton, R. W. (2014). Structure of the subduction transition region from seismic array data in southern Peru. Geophysical Journal International, 196(3), 1889–1905. https://doi.org/10.1093/gji/ggt504

Phillips, K., Clayton, R. W., Davis, P., Tavera, H., Guy, R., Skinner, S., Stubailo, I., Audin, L., & Aguilar, V. (2012). Structure of the subduction system in southern Peru from seismic array data. Journal of Geophysical Research: Solid Earth, 117(B11), n/a-n/a. https://doi.org/10.1029/2012JB009540

Qin, Y., Chen, X., Chen, T., & Abercrombie, R. E. (2022). Influence of Fault Architecture on Induced Earthquake Sequence Evolution Revealed by High-Resolution Focal Mechanism Solutions. Journal of Geophysical Research: Solid Earth, 127(11). https://doi.org/10.1029/2022JB025040

Qin, Y., Chen, X., Walter, J. I., Haffener, J., Trugman, D. T., Carpenter, B. M., Weingarten, M., & Kolawole, F. (2019). Deciphering the Stress State of Seismogenic Faults in Oklahoma and Southern Kansas Based on an Improved Stress Map. Journal of Geophysical Research: Solid Earth, 124(12), 12920–12934. https://doi.org/10.1029/2019JB018377

Ratre, P. (2021). Investigating the regional and local structure of Oklahoma's crust using induced earthquakes.

Ratre, P., & Behm, M. (2021). Imaging the Deep Crustal Structure of Central Oklahoma Using Stacking and Inversion of Local Earthquake Waveforms. Journal of Geophysical Research: Solid Earth, 126(5). https://doi.org/10.1029/2020JB021368

Ringler, A. T., Anthony, R. E., Karplus, M. S., Holland, A. A., & Wilson, D. C. (2018). Laboratory Tests of Three Z-Land Fairfield Nodal 5-Hz, Three-Component Sensors. Seismological Research Letters, 89(5), 1601–1608. https://doi.org/10.1785/0220170236

Ryan, J., Beck, S., Zandt, G., Wagner, L., Minaya, E., & Tavera, H. (2016). Central Andean crustal structure from receiver function analysis. Tectonophysics, 682, 120–133. https://doi.org/10.1016/j.tecto.2016.04.048

Schmandt, B., & Clayton, R. W. (2013). Analysis of teleseismic P waves with a 5200-station array in Long Beach, California: Evidence for an abrupt boundary to Inner Borderland rifting. Journal of Geophysical Research: Solid Earth, 118(10), 5320–5338. https://doi.org/10.1002/jgrb.50370

Schulte-Pelkum, V., & Mahan, K. H. (2014). Imaging Faults and Shear Zones Using Receiver Functions. Pure and Applied Geophysics, 171(11), 2967–2991. https://doi.org/10.1007/s00024-014-0853-4

Stockham, T. G., Cannon, T. M., & Ingebretsen, R. B. (1975). Blind deconvolution through digital signal processing. Proceedings of the IEEE, 63(4), 678–692. https://doi.org/10.1109/PROC.1975.9800

Stone, I., Wirth, E. A., & Frankel, A. D. (2021). Structure and QP–QS Relations in the Seattle and Tualatin Basins from Converted Seismic Phases. Bulletin of the Seismological Society of America, 111(3), 1221–1233. https://doi.org/10.1785/0120200390

Subaši´c, S. S., Agostinetti, N. P., & Bean, C. J. (2019). Estimating lateral and vertical resolution in receiver function data for shallow crust exploration. Geophys. J. Int, 218, 2045–2053. https://doi.org/10.1093/gji/ggz262

Subašić, S., Agostinetti, N. P., & Bean, C. J. (2019). Estimating lateral and vertical resolution in receiver function data for shallow crust exploration. Geophysical Journal International, 218(3), 2045–2053. https://doi.org/10.1093/GJI/GGZ262

Subašić, S., Piana Agostinetti, N., & Bean, C. J. (2020). Assessing the potential of passive seismic receiver functions for ore body exploration. Geophysical Prospecting, 68(7), 2094–2103. https://doi.org/10.1111/1365-2478.12992

Tan, J., Langston, C. A., & Ni, S. (2021). Shallow Shear-Wave Velocity Structure in Oklahoma Based on the Joint Inversion of Ambient Noise Dispersion and Teleseismic P-Wave Receiver Functions. Bulletin of the Seismological Society of America, 111(2), 654–670. https://doi.org/10.1785/0120200246

Umino, N., Hasegawa, A., & Matsuzawa, T. (1995). sP depth phase at small epicentral distances and estimated subducting plate boundary. Geophysical Journal International, 120(2), 356–366. https://doi.org/10.1111/j.1365-246X.1995.tb01824.x

Wang, X., Zhan, Z., Zhong, M., Persaud, P., & Clayton, R. W. (2021). Urban Basin Structure Imaging Based on Dense Arrays and Bayesian Array-Based Coherent Receiver Functions. Journal of Geophysical Research: Solid Earth, 126(9). https://doi.org/10.1029/2021JB022279

Wang, Z., & Behm, M. (2020). Receiver function analysis from a dense nodal array: Delineating shallow crustal structure from local and teleseismic receiver function analysis. AGU Fall Meeting Abstracts, 2020, S069-04.

Wang, Z., Behm, M., Persaud, P., Chen, X., & Carpenter, B. M. (2023). New insights on Moho depth and regional lithospheric structure of central Oklahoma based on receiver function analysis from dense seismic networks. Tectonophysics, 854, 229818. https://doi.org/10.1016/j.tecto.2023.229818

Ward, K. M., Lin, F., & Schmandt, B. (2018). High-Resolution Receiver Function Imaging Across the Cascadia Subduction Zone Using a Dense Nodal Array. Geophysical Research Letters, 45(22), 12,218-12,225. https://doi.org/10.1029/2018GL079903

Wilson, C. K., Jones, C. H., Molnar, P., Sheehan, A. F., & Boyd, O. S. (2004). Distributed deformation in the lower crust and upper mantle beneath a continental strike-slip fault zone: Marlborough fault system, South Island, New Zealand. Geology, 32(10), 837. https://doi.org/10.1130/G20657.1

Yeck, W. L., Hayes, G. P., McNamara, D. E., Rubinstein, J. L., Barnhart, W. D., Earle, P. S., & Benz, H. M. (2017). Oklahoma experiences largest earthquake during ongoing regional wastewater injection hazard mitigation efforts. Geophysical Research Letters, 44(2), 711–717. https://doi.org/10.1002/2016GL071685

Zhang, H., Lee, S., Wolin, E., Bollmann, T. A., Revenaugh, J., Wiens, D. A., Frederiksen, A. W., Darbyshire, F. A., Aleqabi, G. I., Wysession, M. E., Stein, S., & Jurdy, D. M. (2016). Distinct crustal structure of the North American Midcontinent Rift from P wave receiver functions. Journal of Geophysical Research: Solid Earth, 121(11), 8136–8153. https://doi.org/10.1002/2016JB013244

Zhong, M., & Zhan, Z. (2020). An array-based receiver function deconvolution method: methodology and application. Geophysical Journal International, 222(1), 1–14. https://doi.org/10.1093/gji/ggaa113

Zhu, L., & Kanamori, H. (2000). Moho depth variation in southern California from teleseismic receiver functions. Journal of Geophysical Research: Solid Earth, 105(B2), 2969–2980. https://doi.org/10.1029/1999JB900322

Chapter 4

4 Comparative Analysis of the Teleseismic Event Record by Multiple Distributed Acoustic Sensing Arrays

4.1 Abstract

Distributed Acoustic Sensing (DAS) is an emerging technique which records the relative strain variation along an optical fiber. Unlike the traditional standardized seismometer, a DAS array, especially established via dark fiber, may exhibit distinct responses to the ground motion along the fiber due to the variations in fiber coupling, surrounding noise level, array geometry and interrogator type. In this study, we present a comprehensive analysis of the 2021 Mw8.2 Alaska earthquake recorded by three DAS arrays located at Enid, OK, Ridgecrest, CA, and State College, PA, and comparison with nearby broadband seismic stations. We begin by reviewing the bandpass filtered DAS data from each array during the teleseismic wave incident period, which reveals distinct signal-to-noise ratios among the three datasets and within the internal sections of each array. We further stack the DAS waveform by individual segments defined according to the array geometry and compare them with waveforms from nearby broadband seismometers after rotating the horizontal components to the fiber segment orientation. Notably, all three DAS arrays exhibit the capability to capture low-frequency signals with variable signal-to-noise ratio, such as surface waves. Finally, we apply receiver function analysis to a segment of the Enid DAS array and find

comparable conversion phases to those obtained from nearby broadband stations, demonstrating applicability of DAS array on deep structures.

4.2 Introduction

Over the past decade, distributed acoustic sensing (DAS) has gained recognition as a promising ground motion monitoring method within the field of geophysics. With the advances of optical time-domain and frequency-domain reflectometry in distributed optical fiber sensing in 1980s, dynamic strain variation monitoring has become possible for DAS (Aoyama, Nakagawa and Itoh, 1981; Jousset et al., 2018; Lindsey and Martin, 2021). By installing an interrogation system at one end of the optical fiber, lasers are sent into the fiber and subtle phase shifts on the Rayleigh back-scattered light can be recorded, conveying the strain perturbation along the fiber (Mateeva et al., 2012; Li, 2021). Strain or strain rate is calculated based on a spatial increment of the fiber, termed gauge, whose length is determined by the wavelet length of interrogated laser and sample rate. With continuously recorded strain or strain rate at each gauge, DAS repurposed the optical fiber as a seismic array with thousands of single-component channels (Jousset et al., 2018; Zhan, 2020; Li, 2021; Lindsey and Martin, 2021).

Extensive research and practical implementations of DAS have emerged, particularly in seismology and the oil and gas industry. Within the energy sector, DAS finds predominant utilization in downhole environments, enabling in-situ monitoring for injection and hydraulic fracturing operations (Jin and Roy, 2017; Byerley et al., 2018; Sun et al., 2021). DAS-based Vertical Seismic Profiles (VSP) have widely supplemented traditional downhole geophones, facilitating comprehensive cross-well characterization (Mateeva et al., 2012). Continuous data

recording at the interrogation system simplifies real-time monitoring of downhole DAS deployments compared to wireline crews. This advantage allows for time-lapse observations throughout various stages of hydraulic fracturing (Byerley et al., 2018). Additionally, downhole DAS applied for microseismic event monitoring and characterization provides significantly higher data fold compared to conventional downhole geophone arrays (typically 10-50 geophones) (Verdon et al., 2020).

In the seismological community, DAS data supplements the conventional collection of seismology data, which primarily consists of data from broadband stations, short-period seismometers, and temporarily deployed nodes (Zhan, 2020; Lindsey and Martin, 2021). Dark fiber, referring to unused telecommunication cables, provides readily available optical fiber for seismology studies in urban areas where dense installation of traditional seismometers is challenging. This enables studies that incorporate ground motion and urban areas surveillance, including factors such as traffic and regional events (Chambers, 2020; Zhan, 2020). Additionally, DAS data obtained from existing submarine telecommunication cables fills the data gaps in the oceans, where seismic instrumentation is limited (Williams et al., 2019). DAS studies utilizing submarine cables contribute valuable insights into submarine earthquake monitoring, surface gravity waves, and the oceanic environment (Cantono et al., 2021; Castellanos et al., 2022; Williams et al., 2019).

Over the past five years, seismological studies have focused on characterizing waveforms of DAS data (Lindsey et al., 2017; Ajo-Franklin et al., 2019; Yu et al., 2019; Lindsey, Rademacher and Ajo-Franklin, 2020; Muir and Zhan, 2021), which has led to the integration of seismological imaging techniques such as ambient noise interferometry, tomography, and receiver function analysis with DAS (Lancelle, 2016; Jousset et al., 2018; Ajo-Franklin et al., 2019; Yu et al., 2019; Lindsey, Rademacher and Ajo-Franklin, 2020). Although numerous studies have demonstrated the

ability of DAS to capture waveforms comparable to those recorded by traditional seismometers (broadband, short period, and nodes), the utilization of DAS data in earthquake seismology is still in its early stages. Linsey et al. (2017) conducted a comparison between DAS data and precisely calibrated seismometer data below 1Hz, specifically teleseismic and ocean microseismic events, and found a highly correlated waveform between DAS and the co-located seismometer. Ajo-Franklin et al. (2019) reviewed regional and teleseismic DAS waveforms, analyzing the observable phases and waveform differences across different fiber installation geometries. Yu et al. (2019) investigated the potential of DAS in teleseismic studies by analyzing receiver functions derived from DAS data, and vertical component of a broadband seismometer. Their analysis showed highly correlated phases between the DAS receiver functions and those derived from a seismometer.

While there have been numerous earthquake seismology studies conducted using DAS data, the comparison of DAS waveforms across different DAS arrays remains limited. Due to the fact that dark fiber is typically deployed by telecommunication companies, seismologists do not have access to the specific deployment details of the fiber arrays. Variations in deployment factors such as burial depth, coupling, installation geometry, and surrounding noise levels among different DAS arrays can lead to discrepancies in data quality and earthquake responses. In this study, we present an analysis of waveform comparisons across multiple DAS arrays (Ridgecrest, CA, Enid, OK, and FORESEE-urban array at State College, PA) for a mega earthquake event (Mw8.2 Alaska Peninsula, July 29, 2021). We examined the strain/strain rate waveform of the DAS arrays in the aspects of body wave phases and the spectral component. For comparison, we convert the DAS strain/strain rate to particle velocity and utilize the waveforms obtained from nearby broadband seismometers. Additionally, we provide the results of the DAS receiver function derived from a

segment of the Enid DAS array, demonstrating comparable conversion phases to the receiver functions obtained from broadband receivers.

4.3 Array and Data information

On 29 July 2021, a great earthquake (Mw 8.2) ruptured at the plate boundary along the Alaska Peninsula, which is clearly detected by networks across the US (Liu, Lay and Xiong, 2022; Ye et al., 2022; Liu et al., 2023). By accessing the data from three DAS arrays (Figure 4.1) regarding the approximate local arrival time of this event, we obtained the raw DAS data from each array that fully recorded the incident waves.

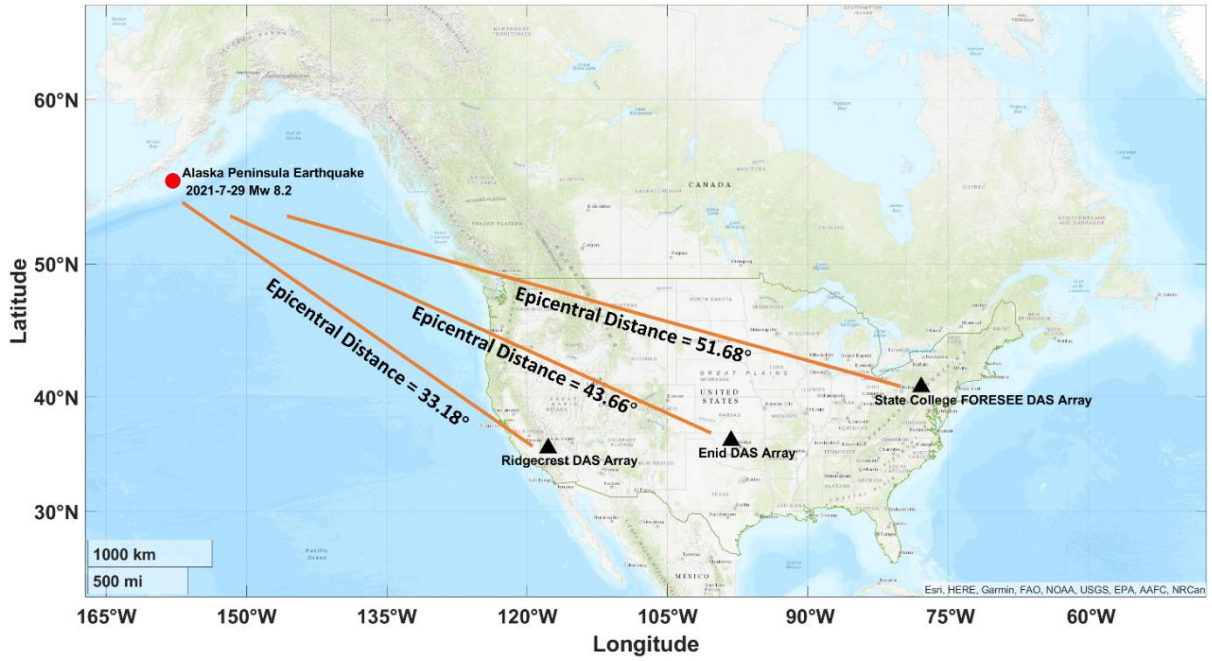


Figure 4.1 Map view of the Alaska Peninsula Mw 8.2 earthquake and Ridgecrest, Enid, and State College DAS array. The epicenter of the earthquake is marked by a red circle and DAS array location is marked by black triangles. Epicentral distance is marked in the figure for each array.

During the summer of 2021, we installed a Silixa Intelligence Distributed Acoustic Sensing (iDAS v2.0) system on a subterranean dark fiber located in Enid, Oklahoma. The iDAS measures the temporal strain rate via phase shift analysis of Rayleigh backscattering with a gauge length of 10m. This installation allowed us to gather DAS data from April 2021 to August 2021 intermittently, as shown in Figure 4.2. The dark fiber extends across the town of Enid in an east-west direction. To establish the DAS array, the network hub located at the Northwestern Oklahoma State University is utilized as a connection point of the iDAS. This division created an east section, which was active from April to June, and a west section, which was active from July to August. The DAS data for the 2021 Alaska Peninsula mega-earthquake is recorded by the west section, which contains 9792 channels with 2-meter spacing at 1000 Hz. The raw data is downsampled to 50 Hz for the teleseismic event waveform.

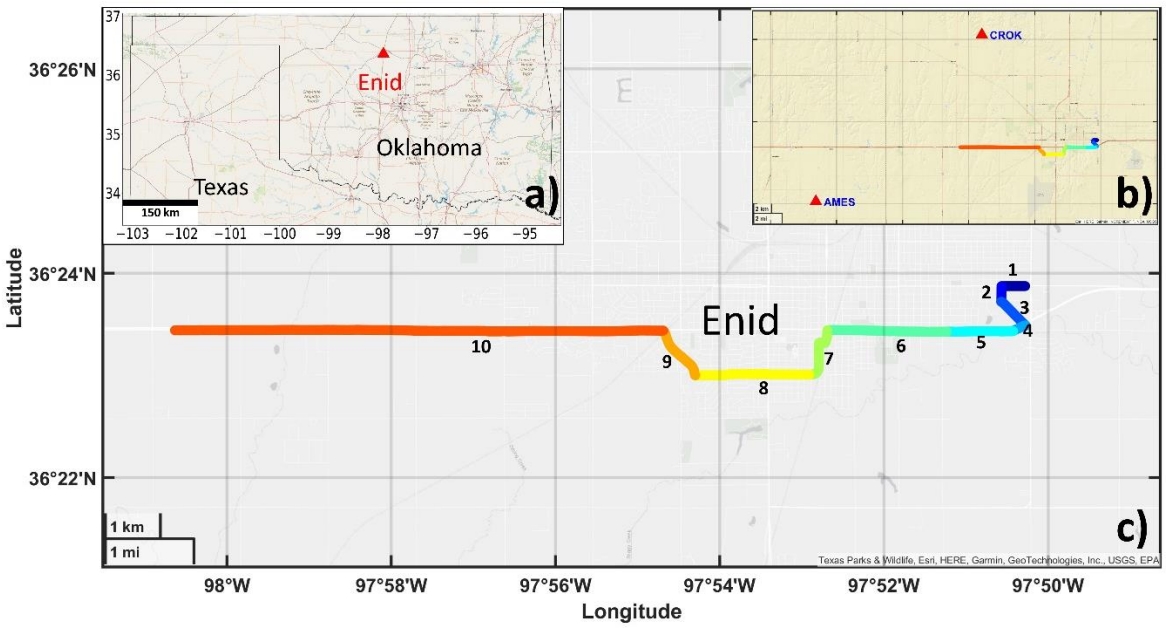


Figure 4.2 Local map view of a) Enid town location in northwest Oklahoma, b) relative position between Enid DAS array (color path) and nearby broadband station (OK-AMES, OK-CROK), and c) Enid DAS array that goes through Enid town. Note the DAS array is plotted in different colors with numbers that represent segments assigned by cable geometry.

The Ridgecrest DAS array was deployed shortly after the mainshock of 2019 Mw 7.1 Ridgecrest Earthquake sequence at the north edge of the Ridgecrest town (Z. Li et al., 2021, Figure 4.3). The Ridgecrest DAS array was installed with an OptaSense ODH3 interrogation system with a gauge length of 10 m, sampling the relative stain along the array at 250 Hz rate and downsampled to 50 Hz for analysis. The dark fiber employed in this setup stretches across a distance of 10 km, following a straight east-west path. Within this dark fiber, there are a total of 1250 channels with an interval of 8 meters between each channel.

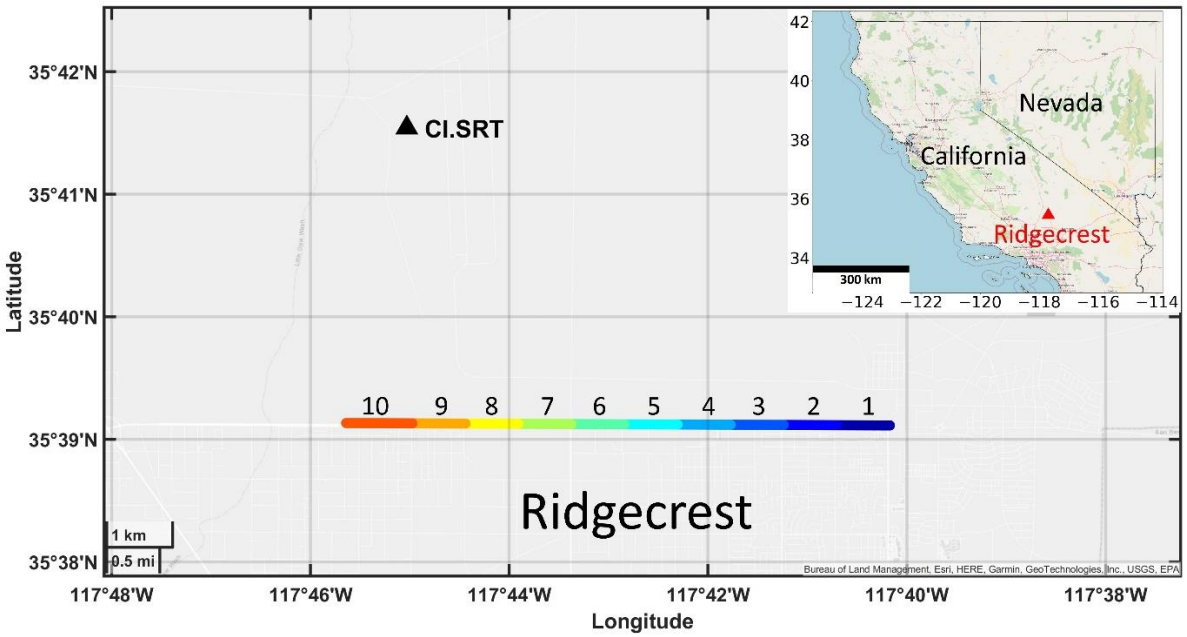


Figure 4.3 Local map view of Ridgecrest location in south California and relative position between Ridgecrest DAS array with segment number and nearby broadband station (CI-SRT).

The Environmental Geophysics Group of Pennsylvania State University, through its FORESEE-urban project, established a DAS observation array along a dark fiber that traverses the town of State College in 2019 (Figure 4.4; Zhu, Shen and Martin, 2021). The fiber-optic cable of this DAS array was buried in the conduit at Penn State University with total length of 5 km. The DAS strain rate along the fiber was recorded by a Silixa iDAS v2 interrogation system at 500 Hz sampling rate with a gauge length of 10 m. Within the dataset, a total of 2137 channels are included, each with a channel spacing of 2 meters.

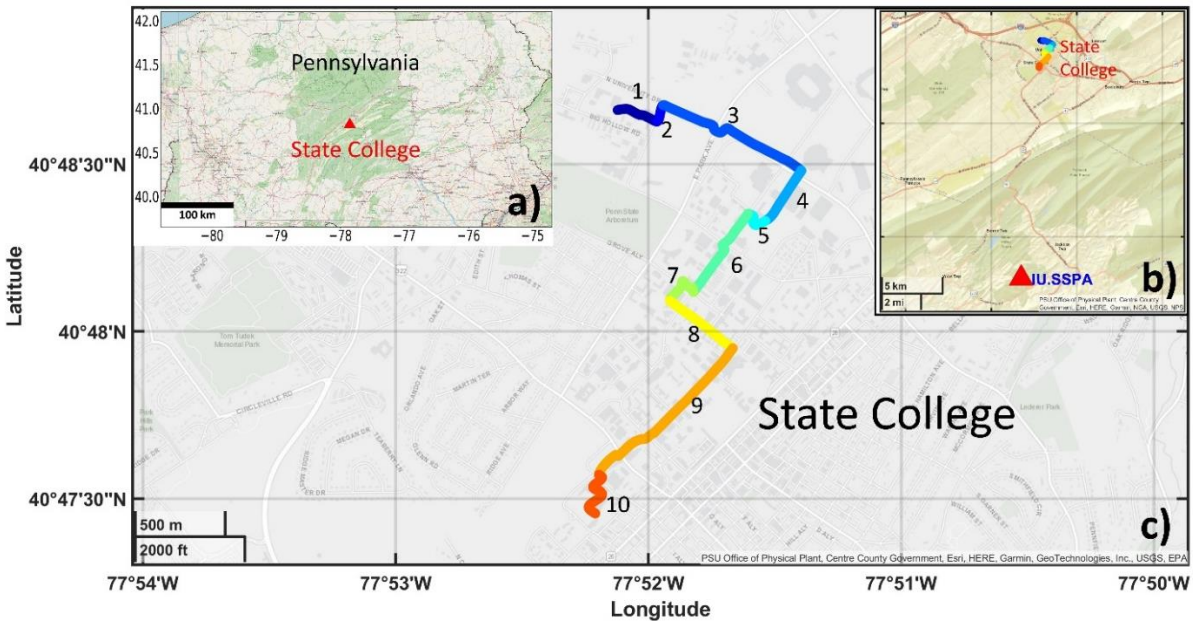


Figure 4.4 Local map view of a) State College location in central Pennsylvania, b) relative position between FORESEE-urban DAS array and a nearby broadband station (IU-SSPA), and c) FORESEE-urban DAS array with segments number that passes through State College.

4.4 Waveform Analysis

4.4.1 Overview of DAS data quality

To conduct preprocessing on the DAS data, we apply the demean and detrend to each channel within the three datasets. In order to emphasize the teleseismic event signal and mitigate high-frequency noise, we implemented a bandpass filter with a range of 0.02 to 1 Hz on the data.

The Enid DAS array boasts the longest total length among the three datasets, spanning over 20 km. Figure 4.5a visually presents the filtered data from all channels of the Enid DAS array, while

the surface wave signal is visible at most channels, there exists distinct data quality along the entire array. Based on the array's geometry, the Enid DAS array is divided into 10 segments, as shown in Figure 4.2. While the first three segments (channel 1-726) and segments 7, 8, and 9 were deployed alongside the residential city road, the remaining segments primarily situate along OK state highway Route 412, a state highway that passes through the town of Enid in an east-west direction. Notably, vibrations from passing traffic can be observed at various times and segments (Figure 4.3).

Segments 1, 2, and 3 (channel 1-726) display a clearer response to the earthquake wave incidence, suggesting a higher data quality compared to the other segments while the quantified signal-to-noise ratio (SNR) of each segment is investigated in the following section. The drastic amplitude reduction between segments 3 and 4 coincides with the transition from local road to the state highway, likely due to the different coupling of the fiber. Given the significant variation in data quality between the first three segments and the later part of the array, we have selected the first three segments for detailed data visualization in Figure 4.5b. It is worth noting the amplitude phase shift that occurs as the array geometry changes. This phenomenon arises from the polarization differences between the incident wave and the fiber's axis orientation.

Figure 4.6 displays the DAS data of Ridgecrest array following the implementation of a bandpass filter (0.02-1 Hz). Since the Ridgecrest DAS array is oriented in a single direction (east-west), there is no polarization variation observed across the array. Moreover, the Ridgecrest dataset consistently exhibits high-quality data across different sections of the array.

In contrast, similar to the Enid DAS array, the FORESEE DAS array is arranged in a complex geometry throughout the State College town (Figure 4.4). Consequently, the DAS data from all

channels within the FORESEE array exhibit distinct polarization characteristics and data quality across different segments of the array (Figure 4.7).

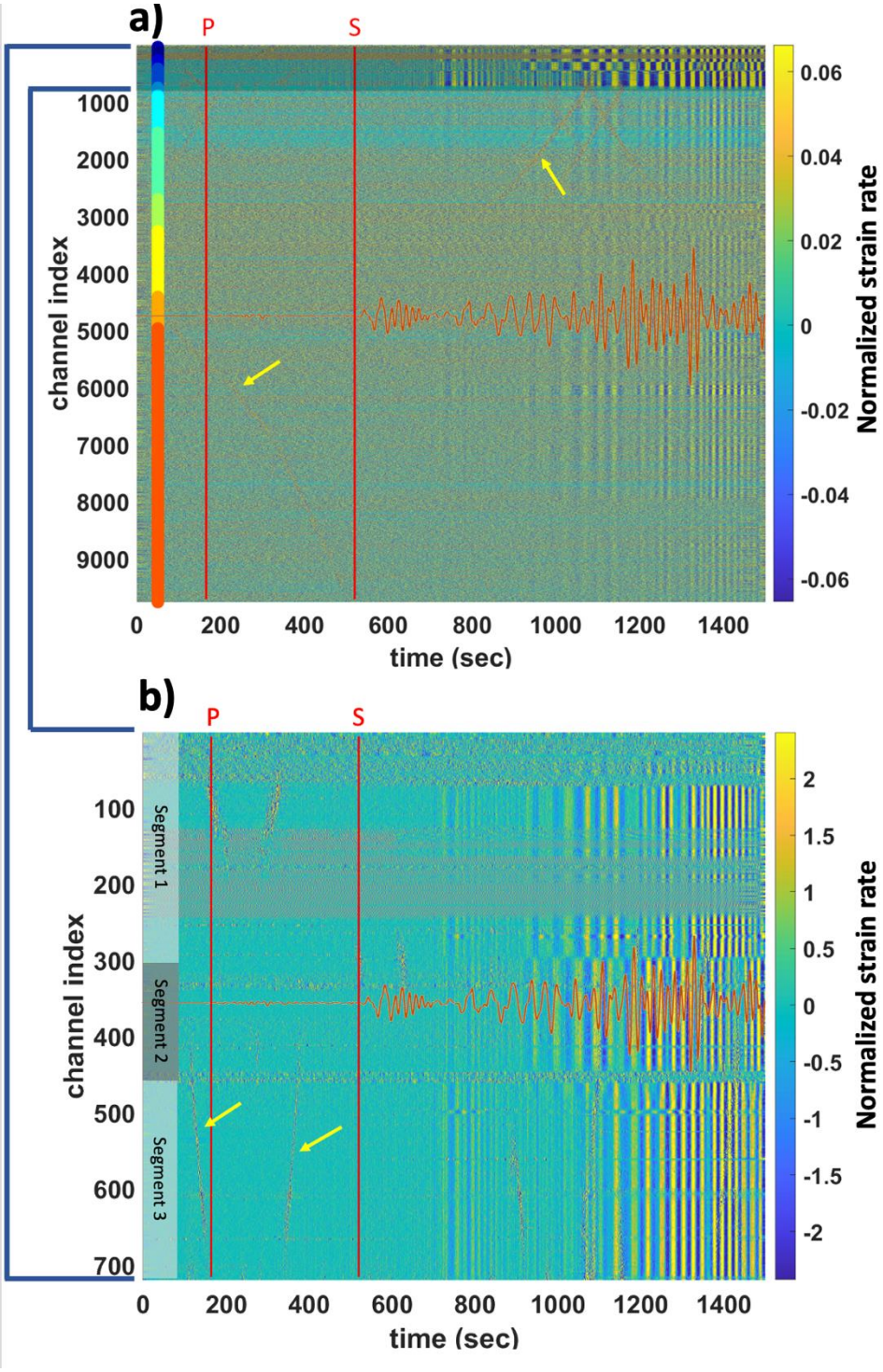


Figure 4.5 Enid DAS data (strain rate, bandpass filter: 0.02-1 Hz) of the Alaska Peninsula earthquake. a) Normalized strain rate waveform of Enid DAS array b) Normalized strain rate waveform of first three segments (channel 1- 726). Segment assignment of the whole array is

laid out at the left side of a) whose color is consistent with that in Figure 4.2. For comparison, the east channel of OK-AMES is also shown in solid red line. The arrival time of P wave and S wave for AMES is marked in red line. Yellow arrows in (a) point out passing traffic signals along state highway. Shaded channels in a) denote the segments that have higher SNR which is zoomed in at the bottom figure.

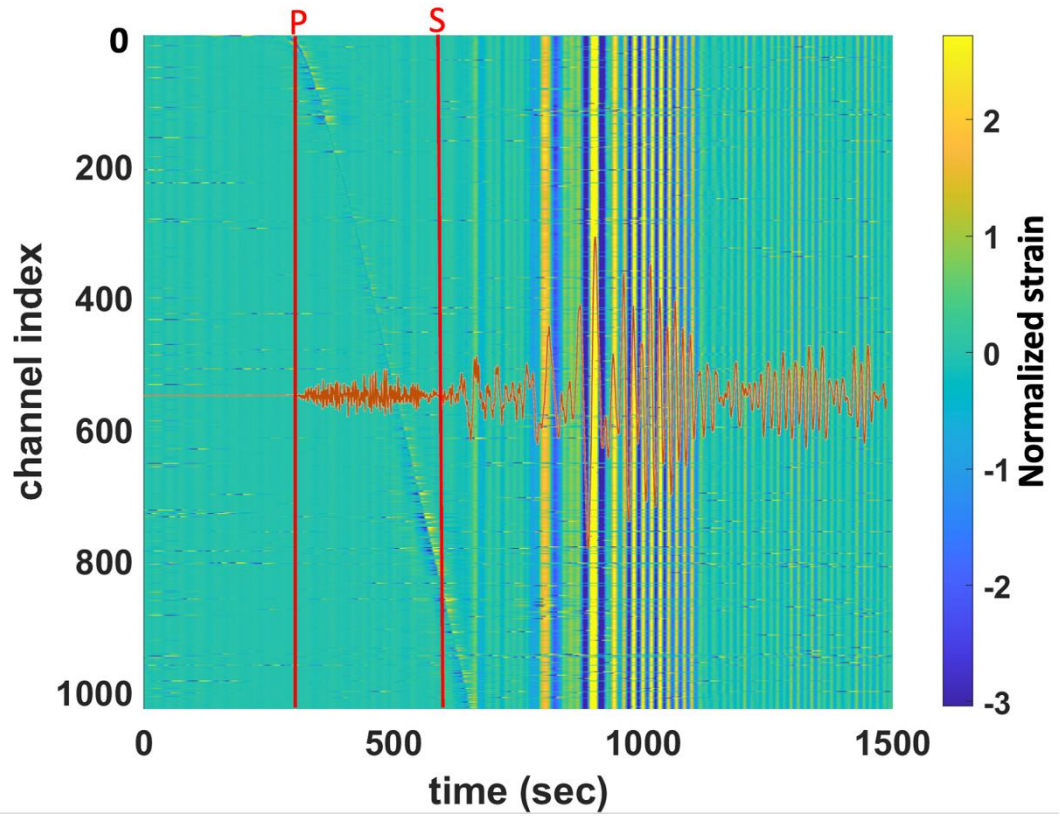


Figure 4.6 Ridgecrest DAS data (strain, bandpass filter: 0.02-1 Hz) of the Alaska Peninsula earthquake. For comparison, the east channel of CI-SRT (bandpass filter: 0.02-1 Hz) is also shown in solid red line. The arrival time of P wave and S wave for SRT is marked in red line. Note the consistent waveform quality throughout all the channels.

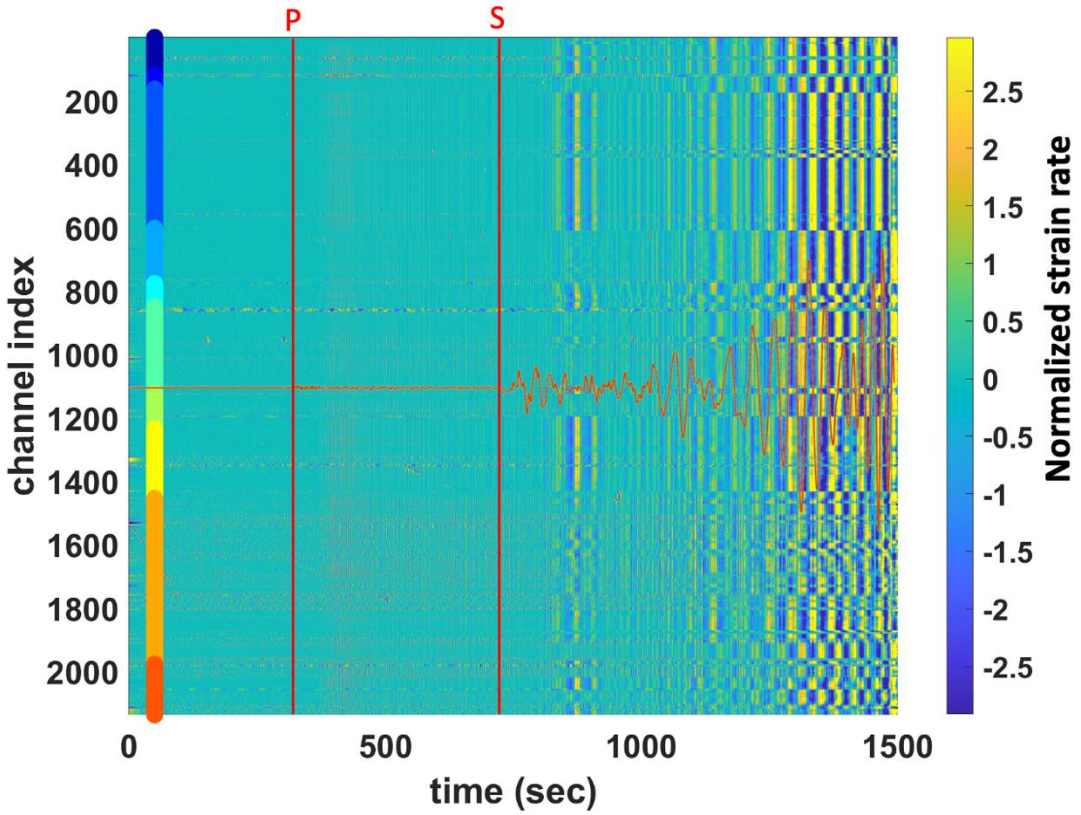


Figure 4.7 State College FORESEE-urban DAS data (strain rate, bandpass filter: 0.02-1 Hz) of the Alaska Peninsula earthquake. Segment assignment of the whole array is laid out at the left side whose color is consistent with that in Figure 4.4. For comparison, the east channel of IU-SSPA (bandpass filter: 0.02-1 Hz) is also shown in solid red line. The arrival time of P wave and S wave for SSPA is marked in red line.

4.4.2 Comparison of stacked DAS data and broadband seismometer data

DAS typically exhibits a higher noise level compared to traditional seismometers due to various factors influencing array stability and the decay of backscattered light (Lindsey et al., 2017; Lindsey, Rademacher and Ajo-Franklin, 2020). To address this, we employ a stacking technique on the DAS data from the three arrays, which is a commonly used method in DAS teleseismic studies (Lindsey et al., 2017; Ajo-Franklin et al., 2019; Yu et al., 2019; Lindsey, Rademacher and Ajo-Franklin, 2020). The stacking helps enhance the SNR and improves the overall quality of the DAS data. For the Enid and FORESEE array, considering the waveform variation across different sections in geometry, we assign 10 segments based on the array orientation and stack the DAS channels within each segment to enhance the coherent phases. In the case of the Ridgecrest array, we simply stacked every 100 channels, as the array layout follows a consistent orientation. The stacked DAS data of three DAS arrays is analyzed regarding teleseismic body wave frequencies (0.02 – 1 Hz) and surface wave frequencies (0.01 – 0.1 Hz), respectively, by utilizing distinct bandpass filters.

As the ground motion along the DAS optical fiber is recorded in terms of relative strain or strain rate between gauges, a conversion from strain or stain rate to particle velocity is required for wavefield analysis. Yu et al. (2019) comprehensively documents the relationship between strain and particle velocity for plane waves, specifically applicable to teleseismic wave incidences. This relationship can be described by the following equation:

$$\varepsilon_{xx} = -\frac{1}{c}\dot{u}_x$$

where ε_{xx}, $\dot{u}_x$, c represents strain, particle velocity, and apparent phase velocity along the cable axial direction, respectively. In the waveform comparison with broadband seismometer recordings, DAS data is converted to particle velocity, and the broadband seismometer is rotated to match the orientation of the fiber segment of the DAS array.

To facilitate a comparison between the particle velocity waveforms of the broadband seismometer and DAS, we appropriately rotated the horizontal component of the broadband seismometer to match the orientation of the respective compared segment. It is important to note that for this comparison, we selected segment 3 of the Enid array due to its high signal-to-noise ratio. Bandpass filtering (0.01-0.1 Hz) is applied to both the stacked DAS particle velocity waveform and the seismometer waveform.

Note that the stacked traces of Enid DAS array exhibit distinct data quality throughout different segments which is also observed from the data overview (Figure 4.5a & 4.8a). Although the low-frequency surface wave around 1400 s might be observable in the stacked traces of segment 4-10, the early phases, including S wave are masked by high-frequency noise. Except for the Enid DAS array, both the Ridgecrest and FORESEE arrays exhibited more consistent SNR throughout the entire array, as shown in Figure 4.9a and Figure 4.10a while the segment 2,4,6,9 of FORESEE array exhibit weak response on the body wave arrival due to their transverse orientation against the wave propagation direction. Comparing the bandpass filtered (0.01-0.1 Hz), DAS particle velocity waveform with broadband particle velocity waveform (Figure 4.8c, 4.9c, 4.10c), all three DAS arrays exhibit a strong correlation with the seismometer waveform, indicating the remarkable capability of DAS in capturing low-frequency components. We demonstrate the teleseismic event response of DAS data for various frequency bands by applying four different frequency band filters to the selected stacked trace (Figure 4.8d, 4.9d, 4.10d). It is noteworthy that the SNR exhibits a

notable improvement when the high-pass threshold is set at or below 0.02 Hz, allowing for the observation of body wave arrival phases.

To quantify the signal quality changes within each array in Figures 4.5 to 4.10, a numerical value of SNR is computed for each segment using the ratio of the power of the waveform within signal and noise window (Figure 4.11) in both body wave frequency band and surface wave frequency band, respectively. Note that the Enid DAS data in body wave frequency band exhibit relatively lower SNR (0 ~ 6 dB) than Ridgecrest and Foresee DAS array (14 ~ 45 dB). Within the Enid array, the first three segments appear higher SNR, which is in agreement with the waveform prescreening (Figure 4.5). A significant improvement of SNR of Enid DAS data is observed for surface-wave frequency band, while the changes in SNR in surface wave frequency band for Ridgecrest and FORESEE arrays is minor. The most significant change in SNR for the Enid array is observed for the first three segments along local roads (Figure 4.11b), which reach a similar level of SNR to the Ridgecrest and the FORESEE arrays, while the improvement of SNR for other segments along the state highway is less significant.

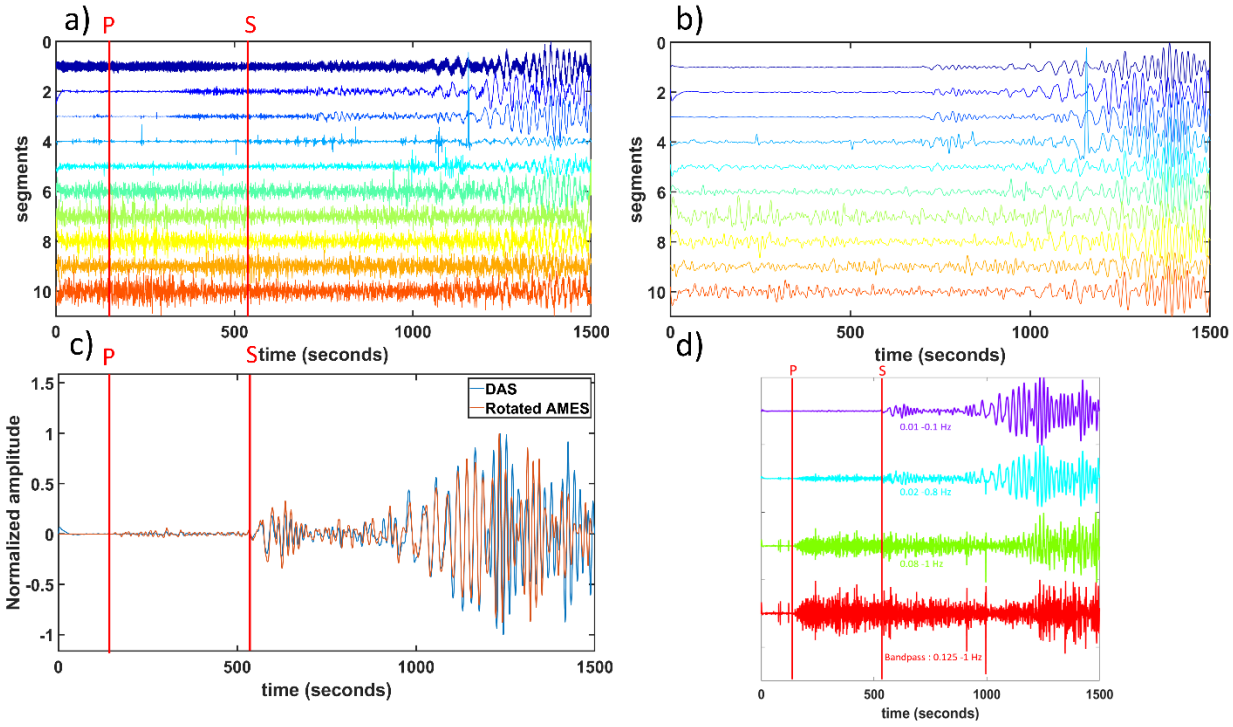


Figure 4.8 Stacked DAS data of Enid and rotated horizontal component of broadband seismometer. a) Stacked DAS particle velocity waveform by segment (bandpass filter: 0.02- 1 Hz). b) Stacked DAS particle velocity waveform by segment (bandpass filter: 0.01- 0.1 Hz). c) Filtered DAS particle velocity (segment 3) and rotated horizontal component of OK-AMES (bandpass filter: 0.01-0.1 Hz). d) DAS particle velocity waveform of segment 3 with different bandpass filter. Frequency band is printed below each trace.

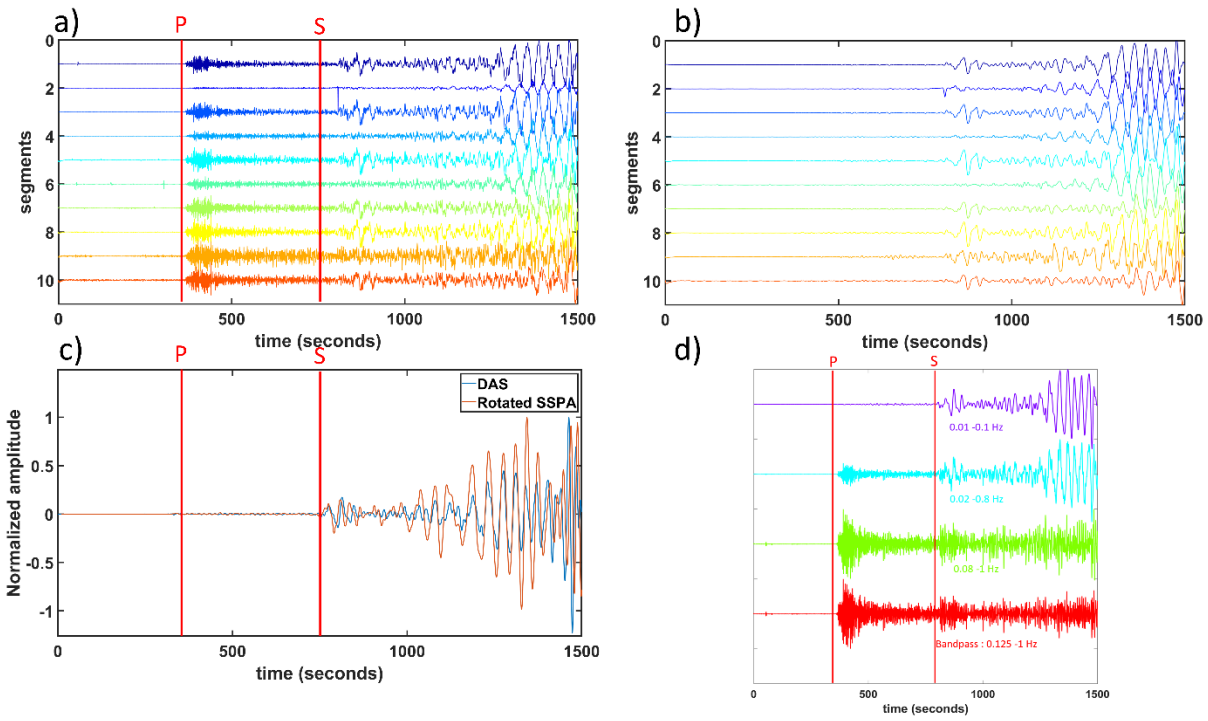


Figure 4.9 Stacked DAS data of FORESEE-urban array and rotated horizontal component of broadband seismometer. a) Stacked DAS particle velocity waveform by segment (bandpass filter: 0.01- 1 Hz). b) Stacked DAS particle velocity waveform by segment (bandpass filter: 0.01- 0.1 Hz). c) Filtered DAS particle velocity (segment 3) and rotated horizontal component of IU-SSPA (bandpass filter: 0.01-0.1 Hz). d) DAS particle velocity waveform of segment 3 with different bandpass filter. Frequency band is printed below each trace.

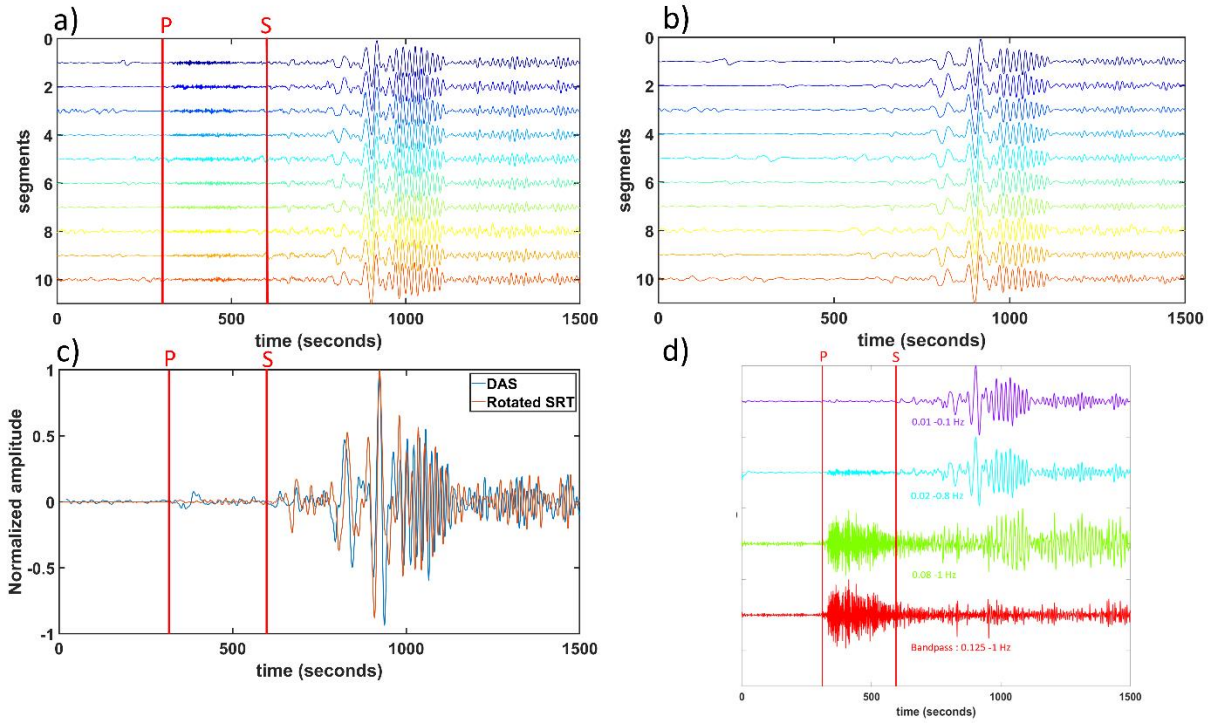


Figure 4.10 Stacked DAS data of Ridgecrest array and rotated horizontal component of broadband seismometer. a) Stacked DAS particle velocity waveform by segment (bandpass filter: 0.01- 1 Hz). b) Stacked DAS particle velocity waveform by segment (bandpass filter: 0.01- 0.1 Hz). c) Filtered DAS particle velocity (segment 3) and rotated horizontal component of CI-SRT (bandpass filter: 0.01-0.1 Hz). d) DAS particle velocity waveform of segment 3 with different bandpass filter. Frequency band is printed below each trace.

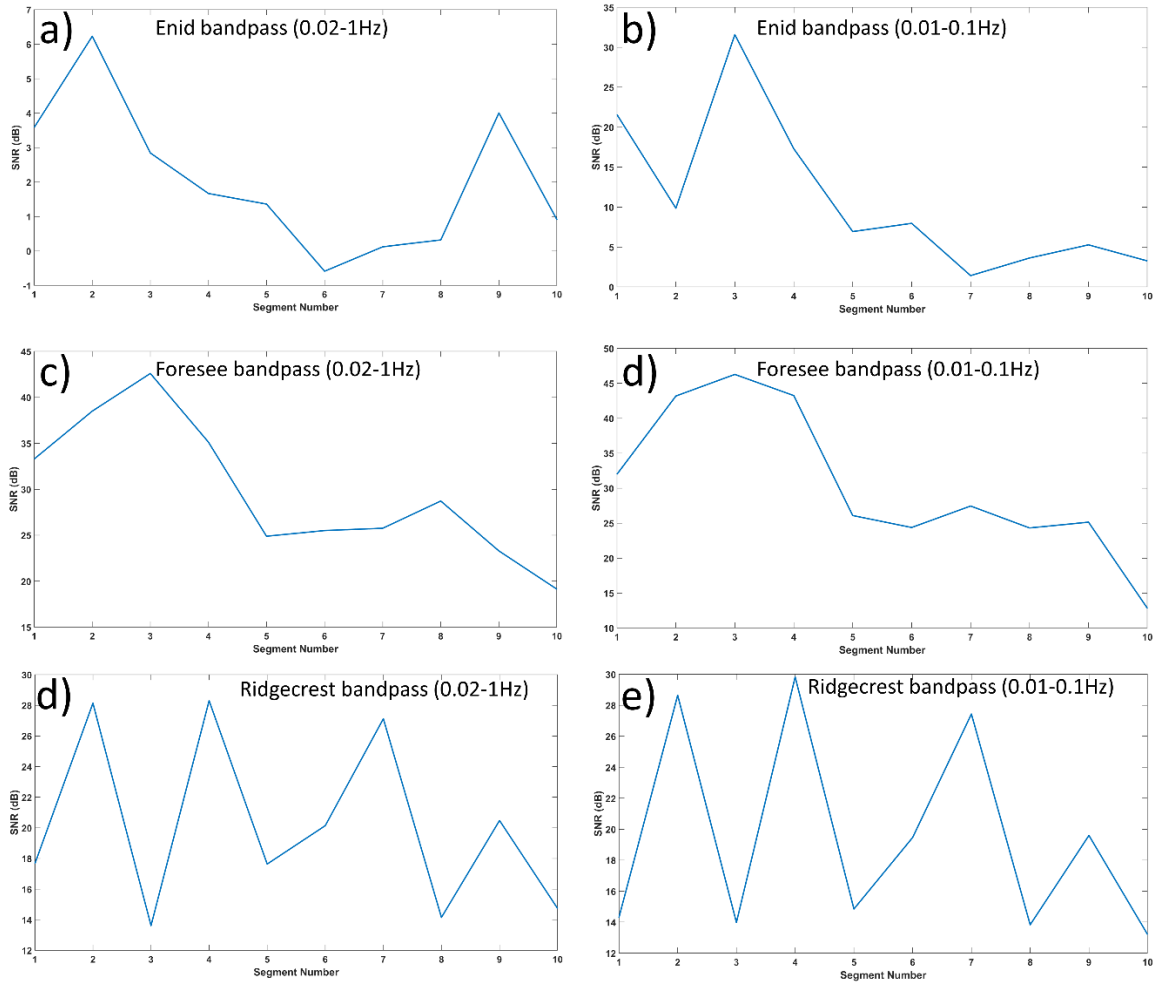


Figure 4.11 SNR of each segment of Enid (a, b), FORESEE (c, d), Ridgecrest (d, e) DAS array under body wave frequency band (0.02-1 Hz) and surface wave frequency band (0.01-0.1 Hz).

4.4.3 Spectral Analysis

To analyze the spectral characteristics of the DAS waveform for the Alaska Peninsula mega-earthquake, we computed the scalogram of the DAS data and the nearby broadband seismometer

data. We applied a bandpass filter (0.02-1 Hz) to both waveforms in order to emphasize the dominant frequency components of teleseismic body waves and surface waves. The results indicate that the DAS array is capable of detecting the low-frequency component, suggesting a comparable sensitivity to long-period waves as the broadband seismometer (Figure 4.12 – 4.14). In the higher frequency range (0.1 - 1 Hz), we observe a similar level of sensitivity to the broadband seismometer, although the identification of body waves (P-wave and S-wave) on the DAS is influenced by the array orientation and wave polarization. It is worth noting that the FORESEE DAS array may outperform the SSPA broadband high-gain seismometer (BHE) at frequencies near 1 Hz with more clear identification of P-wave.

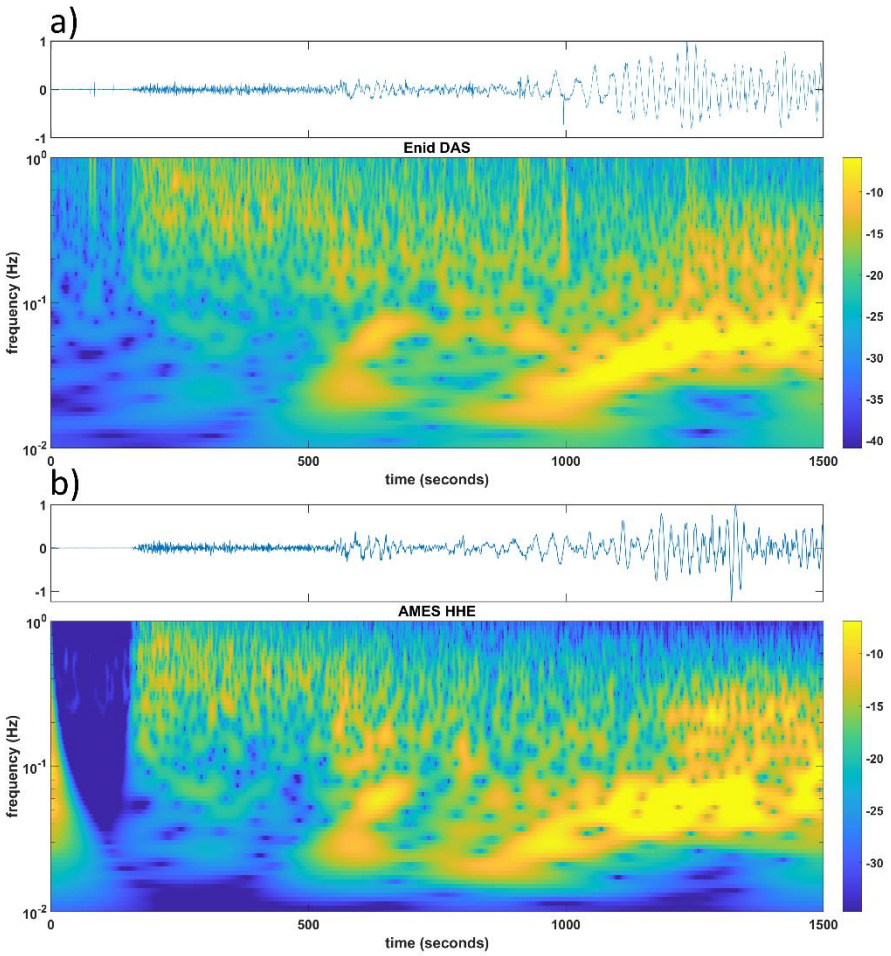


Figure 4.12 Spectrogram of a) Enid DAS data and b) broadband seismometer (AMES HHE) waveform.

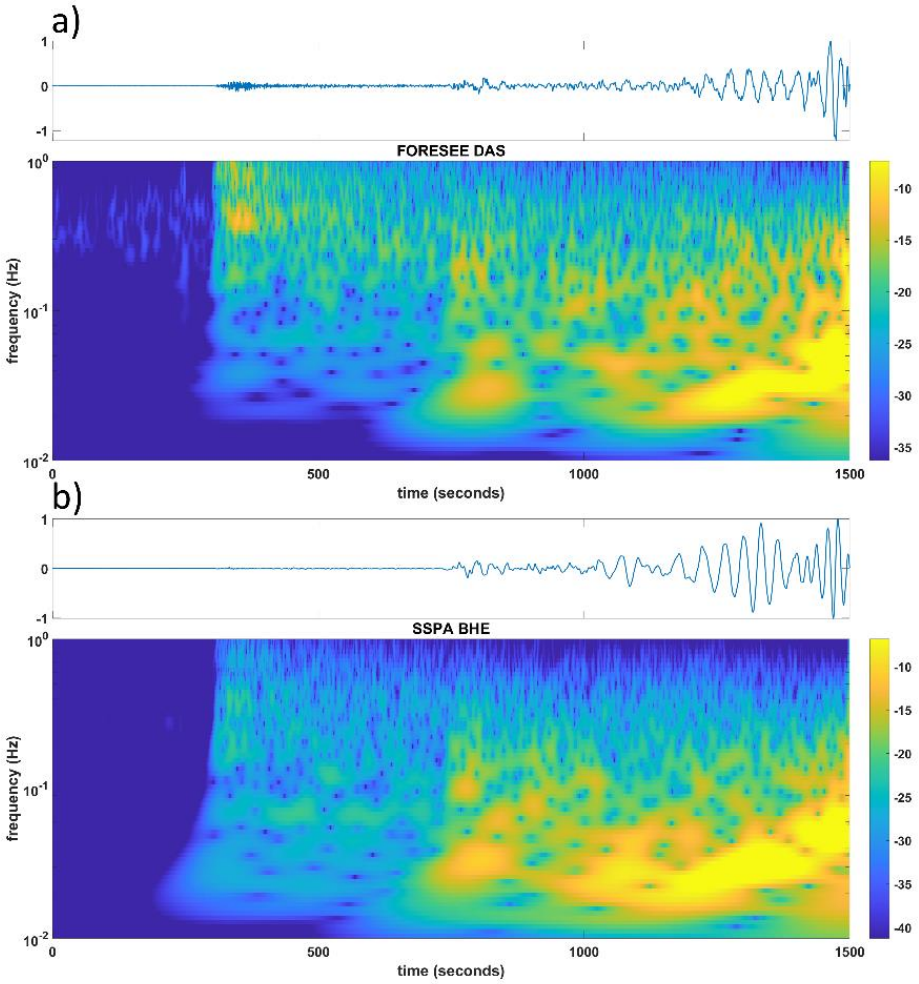


Figure 4.13 Spectrogram of a) FORESEE-urban DAS data and b) broadband seismometer (SSPA BHE) waveform.

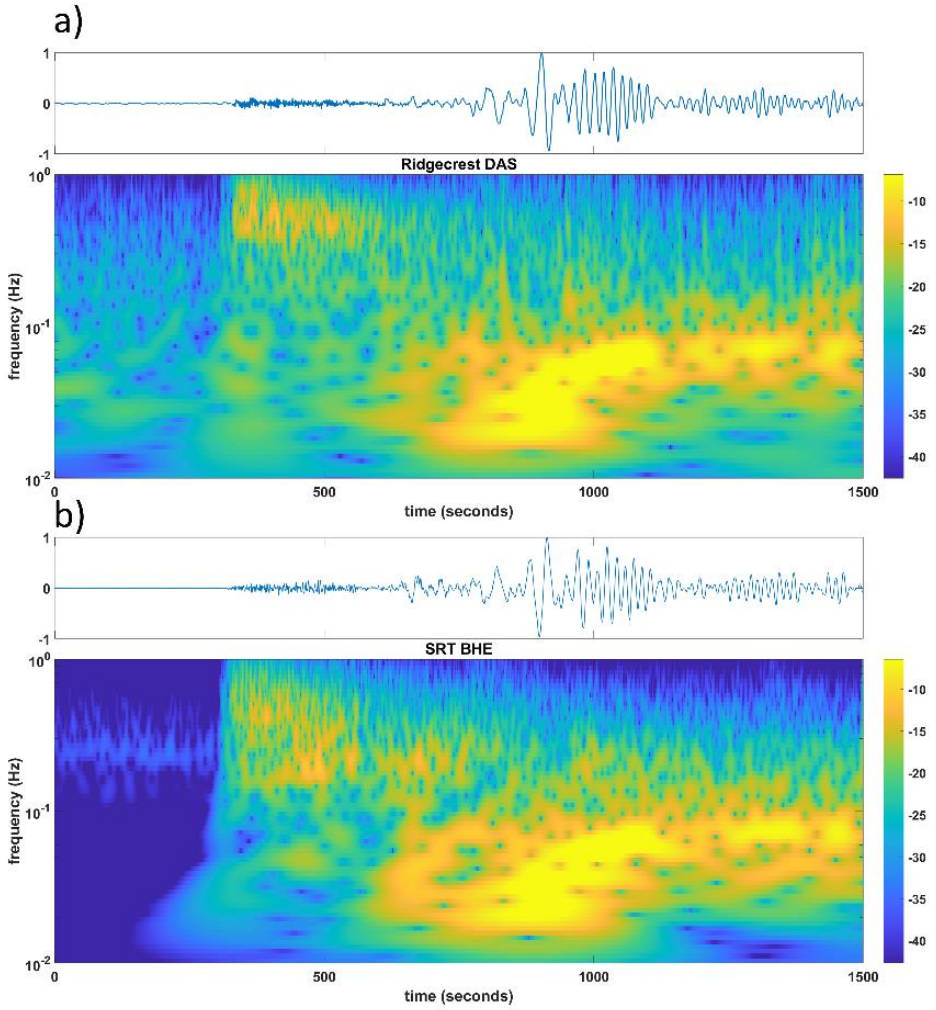


Figure 4.14 Spectrogram of a) Ridgecrest DAS data and b) broadband seismometer (SRT BHE) waveform.

4.5 DAS Receiver functions.

Receiver function (RF) is an established technique in earthquake seismology to investigate the crustal and mantle structure (Zhu and Kanamori, 2000; Li et al., 2003; Persaud, Pérez-Campos and Clayton, 2007; Gans et al., 2011; McGlannan and Gilbert, 2016; Zhang et al., 2016; Liu, Persaud and Clayton, 2018; Wang et al., 2023). By deconvolving the source wavelet of teleseismic from

the horizontal component of P-wave coda, receiver function can present the conversion boundaries where incident P-wave is converted to S-wave at impedance contrast. Common practice of traditional RF analysis approximates the vertical component of teleseismic wave to source wavelet and deconvolve it from radial component or transverse component that are rotated from two horizontal components of the seismometer.

With the increasing availability of DAS data in terms of temporal and spatial coverage, there is potential for utilizing DAS data in Receiver Function (RF) analysis. While RF analysis traditionally requires 3-component data for teleseismic events, the 1-component horizontal particle velocity waveform obtained from DAS, when combined with collocated or nearby seismometer data, can provide an approximation of the radial or transverse receiver function. Although this approach is still in the exploratory stage, Yu et al. (2019) demonstrated RF analysis based on data from a DAS array at Goldstone, CA, and a nearby broadband station. In this study, we applied RF analysis to the Enid DAS array data and compared the DAS-derived RFs with those obtained from a broadband seismometer. Unfortunately, the collocated 3-component nodes were not active during the Alaska Peninsula Mw8.2 teleseismic event incidence. As a substitute, we utilized the vertical component from a nearby broadband station (Fig. 4.2b; OK-AMES) as an approximation of the source wavelet. Considering the high signal-to-noise ratio (SNR) and sub-parallel axis to the radial orientation, we selected segment 3 of the DAS data for RF analysis.

To calculate the Receiver Functions (RFs), we employ a time-domain iterative deconvolution approach. We compute the RFs for a subset of segment 3 (Figure 4.15b) as well as the stacked trace of all channels within this segment (Figure 4.15c). It is important to note that the interpretation of RFs typically involves stacking RFs derived from multiple teleseismic events. Therefore, our goal is not to provide a definitive interpretation solely based on the Enid DAS

receiver function. Instead, our focus is on comparing the DAS-derived RFs with the receiver function obtained from the broadband station. By examining the DAS RF alongside the single broadband receiver function traces and stacked receiver function (Wang et al., 2023), we can identify comparable phases in the DAS RF (Fig. 15c). This observation suggests the feasibility of utilizing DAS data for RF analysis and indicates its potential as a valuable tool in seismic studies.

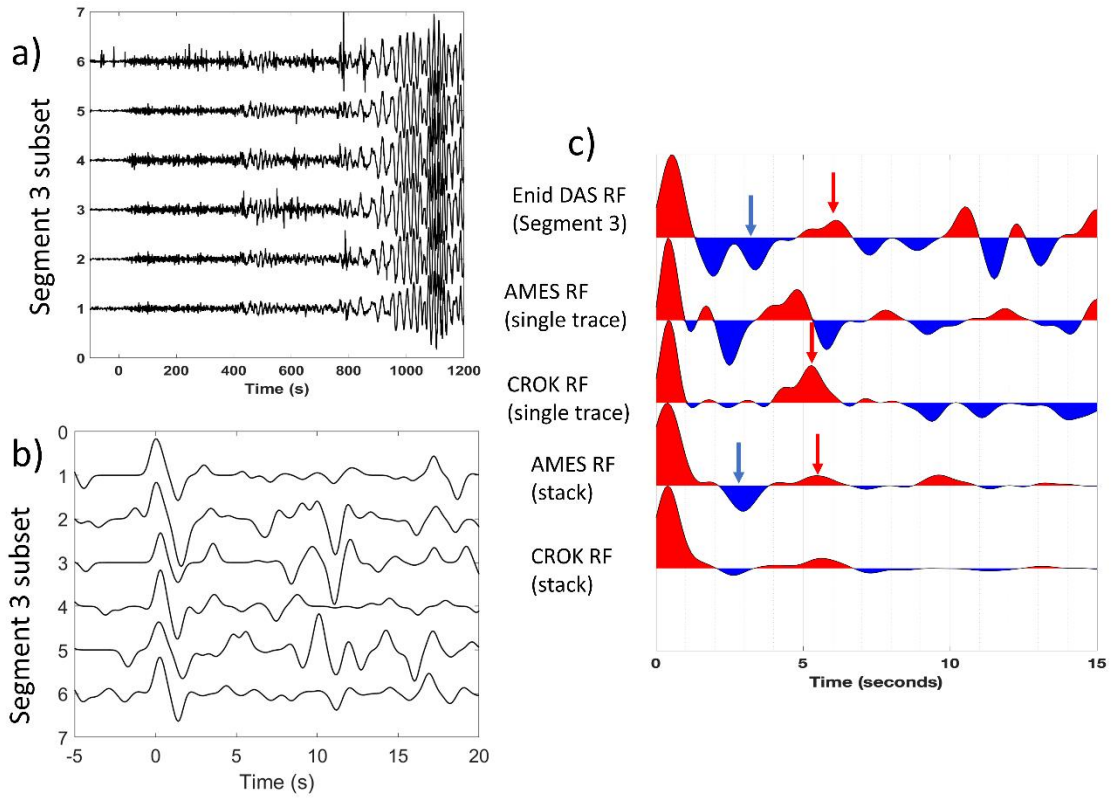


Figure 4.15 Stacked subset DAS data and RFs derived from DAS and vertical channel of broadband station. a) Stacked DAS particle velocity of subset of Enid array segment 3. b) RFs derived from the DAS waveform in a) and vertical channel of OK-AMES. c) RFs from two broadband stations (OK-AMES & OK-CROK) and DAS RFs. Note the stacked RF traces from AMES and CROK are modified from (Wang et al., 2023). Coherent phases (red arrow: Moho conversion; blue arrow: basement reverberation) are marked by arrows.

4.6 Discussion

To fulfill the performance in industrial project, in-well DAS is commonly deployed with industrial standard alongside other well-logging equipment. Correa et al. (2017) conducted an examination of in-well Distributed Acoustic Sensing (DAS) arrays in terms of signal to noise ratio (SNR), demonstrating an average SNR of in-well DAS vertical seismic profile (VSP) at around 30 dB. However, a challenge arises when dealing with dark fibers deployed by various telecom companies

in different regions. These fibers have distinct coupling and layout geometries, making it difficult to process and calibrate data across various arrays. The waveform analysis and quantified SNR of Enid DAS data regarding teleseismic event suggest distinct data qualities for sections that are deployed in residential areas and those are deployed along state highway, while the FORESEE and Ridgecrest DAS array that are deployed mainly in the residential or rual areas exhibit relatively high SNR in both body wave frequency band (0.02 – 1 Hz) and surface wave frequency band (0.01 – 1 Hz).

Yu et al. (2019) have highlighted the potential of using receiver function (RF) analysis with Distributed Acoustic Sensing (DAS) data. The results have shown convincing conversion phases and comparable phases to those obtained from traditional seismometers such as nodes, broadband stations, and short period seismometers. However, a major limitation in employing DAS RF in a general deployment scenario is the necessity of a vertical component, which can only be obtained from a co-located node or a nearby broadband station. Moreover, the application of DAS RF for imaging purposes is still in its early stages. When it comes to teleseismic RF for deep structure imaging, traditional seismometers need to be distributed over a large area to capture lateral structure variations from the mantle and crust. However, the dark fiber DAS array, which extends over tens of kilometers, lacks sufficient horizontal expansion to adequately capture lateral variations for deep structure imaging. Nevertheless, the densely spaced channels provided by DAS arrays offer an advantage for local earthquake RF analysis. Multichannel deconvolution algorithms applied to DAS data may yield promising results for investigating shallow and local geological structures.

4.7 Conclusion

This study presents a comparative analysis of the response to the 2019 Mw 8.2 Alaska Peninsula earthquake in three different Distributed Acoustic Sensing (DAS) arrays located across the United States. Waveform analysis reveals distinct signal-to-noise ratios (SNRs) among the various DAS arrays and different sections of the optical fiber. The Ridgecrest DAS array and the FORESEE-urban DAS array exhibit relatively higher SNR than the Enid array and all three arrays exhibit variabilities of SNR among different segments. The Enid array exhibits a significant decrease in SNR when transitioning from local road to state highway. Despite the SNR differences, all three DAS arrays demonstrate remarkable capabilities in capturing and retaining low-frequency components. Additionally, we present preliminary results from receiver function analysis using Enid DAS data. It is important to note that the interpretation of these results is limited due to the availability of receiver functions from multiple teleseismic events. Nonetheless, our findings show comparable phases to the receiver function obtained from the broadband station, indicating the potential utility of DAS data in receiver function analysis.

These findings highlight the potential of DAS arrays, including Enid, Ridgecrest, and FORESEE, as valuable tools for seismic monitoring and analysis. The ability of DAS arrays to capture body waves as well as low-frequency signals of teleseismic events, combined with the comparable conversion phases observed in receiver functions, further validates their potential for seismological studies. The research contributes to the growing body of knowledge on the capabilities and effectiveness of DAS technology in seismic monitoring and provides insights for future studies and applications in earthquake research.

4.8 References

Ajo-Franklin, J. B., Dou, S., Lindsey, N. J., Monga, I., Tracy, C., Robertson, M., Rodriguez Tribaldos, V., Ulrich, C., Freifeld, B., Daley, T., & Li, X. (2019). Distributed Acoustic Sensing Using Dark Fiber for Near-Surface Characterization and Broadband Seismic Event Detection. *Scientific Reports*, *9*(1), 1328. https://doi.org/10.1038/s41598-018-36675-8

Aoyama, K., Nakagawa, K., & Itoh, T. (1981). Optical time domain reflectometry in a single-mode fiber. *IEEE Journal of Quantum Electronics*, *17*(6), 862–868. https://doi.org/10.1109/JQE.1981.1071237

Byerley, G., Monk, D., Aaron, P., & Yates, M. (2018). Time-lapse seismic monitoring of individual hydraulic frac stages using a downhole DAS array. *The Leading Edge*, *37*(11), 802–810. https://doi.org/10.1190/tle37110802.1

Cantono, M., Castellanos, J. C., Kamalov, V., Mecozzi, A., Muller, R., Yin, S., & Zhan, Z. (2021). Seismic Sensing in Submarine Fiber Cables. 2021 European Conference on Optical Communication (ECOC), 1–3. https://doi.org/10.1109/ECOC52684.2021.9605838

Castellanos, J. C., Zhan, Z., Kamalov, V., Cantono, M., Yin, S., Mecozzi, A., Bhattacharya, S., & Allen, R. M. (2022). Optical polarization-based sensing and localization of submarine earthquakes. Optical Fiber Communication Conference (OFC) 2022, M1H.4. https://doi.org/10.1364/OFC.2022.M1H.4

Chambers, K. (2020). Using DAS to investigate traffic patterns at Brady Hot Springs, Nevada, USA. *The Leading Edge*, *39*(11), 819–827. https://doi.org/10.1190/tle39110819.1

Correa, J., Egorov, A., Tertyshnikov, K., Bona, A., Pevzner, R., Dean, T., ... & Marshall, S. (2017). Analysis of signal to noise and directivity characteristics of DAS VSP at near and far offsets—A CO2CRC Otway Project data example. The Leading Edge, 36(12), 994a1-994a7.

Gans, C. R., Beck, S. L., Zandt, G., Gilbert, H., Alvarado, P., Anderson, M., & Linkimer, L. (2011). Continental and oceanic crustal structure of the Pampean flat slab region, western Argentina, using receiver function analysis: new high-resolution results. *Geophysical Journal International*, *186*(1), 45–58. https://doi.org/10.1111/J.1365-246X.2011.05023.X

Jin, G., & Roy, B. (2017). Hydraulic-fracture geometry characterization using low-frequency DAS signal. *The Leading Edge*, *36*(12), 975–980. https://doi.org/10.1190/tle36120975.1

Jousset, P., Reinsch, T., Ryberg, T., Blanck, H., Clarke, A., Aghayev, R., Hersir, G. P., Henninges, J., Weber, M., & Krawczyk, C. M. (2018). Dynamic strain determination using fibre-optic cables allows imaging of seismological and structural features. *Nature Communications*, *9*(1), 2509. https://doi.org/10.1038/s41467-018-04860-y

Lancelle, C. (2016). *Distributed Acoustic Sensing for Imaging Near-Surface Geology and Monitoring Traffic at Garner Valley, California*. UNIVERSITY OF WISCONSIN – MADISON.

Li, X., Bock, G., Vafidis, A., Kind, R., Harjes, H.-P., Hanka, W., Wylegalla, K., van der Meijde, M., & Yuan, X. (2003). Receiver function study of the Hellenic subduction zone: imaging crustal thickness variations and the oceanic Moho of the descending African lithosphere. *Geophysical Journal International*, *155*(2), 733–748. https://doi.org/10.1046/j.1365-246X.2003.02100.x

Li, Z. (2021). Recent advances in earthquake monitoring I: Ongoing revolution of seismic instrumentation. *Earthquake Science*, *34*(2), 177–188. https://doi.org/10.29382/eqs-2021-0011

Li, Z., Shen, Z., Yang, Y., Williams, E., Wang, X., & Zhan, Z. (2021). Rapid Response to the 2019 Ridgecrest Earthquake With Distributed Acoustic Sensing. *AGU Advances*, *2*(2). https://doi.org/10.1029/2021AV000395

Lindsey, N. J., & Martin, E. R. (2021). Fiber-Optic Seismology. *Annual Review of Earth and Planetary Sciences*, *49*(1), 309–336. https://doi.org/10.1146/annurev-earth-072420-065213

Lindsey, N. J., Martin, E. R., Dreger, D. S., Freifeld, B., Cole, S., James, S. R., Biondi, B. L., & Ajo-Franklin, J. B. (2017). Fiber-Optic Network Observations of Earthquake Wavefields. *Geophysical Research Letters*, *44*(23). https://doi.org/10.1002/2017GL075722

Lindsey, N. J., Rademacher, H., & Ajo-Franklin, J. B. (2020). On the Broadband Instrument Response of Fiber-Optic DAS Arrays. *Journal of Geophysical Research: Solid Earth*, *125*(2). https://doi.org/10.1029/2019JB018145

Liu, C., Bai, Y., Lay, T., Feng, Y., & Xiong, X. (2023). Megathrust complexity and the up-dip extent of slip during the 2021 Chignik, Alaska Peninsula earthquake. *Tectonophysics*, *854*, 229808. https://doi.org/10.1016/j.tecto.2023.229808

Liu, C., Lay, T., & Xiong, X. (2022). The 29 July 2021 Mw 8.2 Chignik, Alaska Peninsula Earthquake Rupture Inferred From Seismic and Geodetic Observations: Re-Rupture of the Western 2/3 of the 1938 Rupture Zone. *Geophysical Research Letters*, *49*(4). https://doi.org/10.1029/2021GL096004

Liu, G., Persaud, P., & Clayton, R. W. (2018). Structure of the Northern Los Angeles Basins Revealed in Teleseismic Receiver Functions from Short-Term Nodal Seismic Arrays. *Seismological Research Letters*, *89*(5), 1680–1689. https://doi.org/10.1785/0220180071

Mateeva, A., Mestayer, J., Cox, B., Kiyashchenko, D., Wills, P., Lopez, J., Grandi, S., Hornman, K., Lumens, P., Franzen, A., Hill, D., & Roy, J. (2012). Advances in Distributed Acoustic Sensing (DAS) for VSP. *SEG Technical Program Expanded Abstracts 2012*, 1–5. https://doi.org/10.1190/segam2012-0739.1

McGlannan, A. J., & Gilbert, H. (2016). Crustal signatures of the tectonic development of the North American midcontinent. *Earth and Planetary Science Letters*, *433*, 339–349. https://doi.org/10.1016/j.epsl.2015.10.048

Muir, J. B., & Zhan, Z. (2021). Wavefield-based evaluation of DAS instrument response and array design. *Geophysical Journal International*, *229*(1), 21–34. https://doi.org/10.1093/gji/ggab439

Persaud, P., Pérez-Campos, X., & Clayton, R. W. (2007). Crustal thickness variations in the margins of the Gulf of California from receiver functions. *Geophysical Journal International*, *170*(2), 687–699. https://doi.org/10.1111/j.1365-246X.2007.03412.x

Sun, Y., Liu, J., Xue, Z., Li, Q., Fan, C., & Zhang, X. (2021). A critical review of distributed fiber optic sensing for real-time monitoring geologic CO2 sequestration. *Journal of Natural Gas Science and Engineering*, *88*, 103751. https://doi.org/10.1016/j.jngse.2020.103751

Verdon, J. P., Horne, S. A., Clarke, A., Stork, A. L., Baird, A. F., & Kendall, J.-M. (2020). Microseismic monitoring using a fibre-optic Distributed Acoustic Sensor (DAS) array. *GEOPHYSICS*, 1–48. https://doi.org/10.1190/geo2019-0752.1

Wang, Z., Behm, M., Persaud, P., Chen, X., & Carpenter, B. M. (2023). New insights on Moho depth and regional lithospheric structure of central Oklahoma based on receiver function analysis from dense seismic networks. *Tectonophysics*, *854*, 229818. https://doi.org/10.1016/j.tecto.2023.229818

Williams, E. F., Fernández-Ruiz, M. R., Magalhaes, R., Vanthillo, R., Zhan, Z., González-Herráez, M., & Martins, H. F. (2019). Distributed sensing of microseisms and teleseisms with submarine dark fibers. *Nature Communications*, *10*(1), 5778. https://doi.org/10.1038/s41467-019-13262-7

Ye, L., Bai, Y., Si, D., Lay, T., Cheung, K. F., & Kanamori, H. (2022). Rupture Model for the 29 July 2021 Mw 8.2 Chignik, Alaska Earthquake Constrained by Seismic, Geodetic, and Tsunami Observations. *Journal of Geophysical Research: Solid Earth*, *127*(7). https://doi.org/10.1029/2021JB023676

Yu, C., Zhan, Z., Lindsey, N. J., Ajo-Franklin, J. B., & Robertson, M. (2019). The Potential of DAS in Teleseismic Studies: Insights From the Goldstone Experiment. *Geophysical Research Letters*, *46*(3), 1320–1328. https://doi.org/10.1029/2018GL081195

Zhan, Z. (2020). Distributed Acoustic Sensing Turns Fiber-Optic Cables into Sensitive Seismic Antennas. *Seismological Research Letters*, *91*(1), 1–15. https://doi.org/10.1785/0220190112

Zhang, H., Lee, S., Wolin, E., Bollmann, T. A., Revenaugh, J., Wiens, D. A., Frederiksen, A. W., Darbyshire, F. A., Aleqabi, G. I., Wysession, M. E., Stein, S., & Jurdy, D. M. (2016). Distinct crustal structure of the North American Midcontinent Rift from P wave receiver functions. *Journal of Geophysical Research: Solid Earth*, *121*(11), 8136–8153. https://doi.org/10.1002/2016JB013244

Zhu, L., & Kanamori, H. (2000). Moho depth variation in southern California from teleseismic receiver functions. *Journal of Geophysical Research: Solid Earth*, *105*(B2), 2969–2980. https://doi.org/10.1029/1999JB900322

Zhu, T., Shen, J., & Martin, E. R. (2021). Sensing Earth and environment dynamics by telecommunication fiber-optic sensors: an urban experiment in Pennsylvania, USA. *Solid Earth*, *12*(1), 219–235. https://doi.org/10.5194/se-12-219-2021

Chapter 5

5 Conclusions and Future Work

5.1 Conclusion

In this dissertation, I present the applications of receiver function analysis on broadband seismometer data, a densely spaced nodal array, and a dark fiber DAS array, characterizing the Oklahoma subsurface from mantle to shallow crust. While using traditional teleseismic receiver function imaging contributes to the understanding of Oklahoma's deep structure, this dissertation also demonstrates the potential of using local and regional earthquakes in receiver function analysis to image shallow structures. By evaluating the teleseismic responses of different DAS arrays (Enid, Ridgecrest, and FORESEE-urban), the data quality in terms of signal-to-noise ratio (SNR) and spectral responses is reviewed. Despite receiver function being a well-established technique and a major tool in passive seismic imaging, this dissertation emphasizes the untapped potential of these methods on incorporating new datasets for understudied areas, implementing novel algorithms to achieve higher resolution, and utilizing different types of data from alternative sources or acquired through innovative instruments.

Some of the key results are:

(1) I applied teleseismic RF analysis to the broadband and short period seismometers widely distributed in central Oklahoma and provide the first image of the Moho discontinuity in Oklahoma. Upon updating the knowledge of crustal thickness from previous studies, the

Moho map from RF reveals the crust thickness ranges from 40 km to 55 km where the deepest Moho is observed in the Anadarko Shelf to the northwest and a shallowing trend towards the east. A mid-lithosphere discontinuity is observed within the upper mantle, in depth ranging from 60 km to 100 km. An intracrustal discontinuity observed near the linear gravity anomalies close to Kansas may suggest rift-filling magmatism related to the midcontinent rift although evidence of rifting is not observed from RF profiles.

(2) I developed an inversion routine using multi-channel blind deconvolution to calculate the RF from local and regional earthquakes. RFs derived from a densely spaced nodal array in Cushing, Oklahoma present a high-resolution image of the shallow subsurface. In particular, the conversion phase of basement top interface is well-depicted in the RF profiles that arrange the RFs in terms of strike and crossline to the fault beneath the nodal array. The estimated depth of the basement conversion is around 1.2 km, remarkably consistent with the basement depth map from previous studies.

(3) I presented comparative analysis for the 2021 Mw 8.2 Alaska Peninsula earthquake waveforms recorded by Enid, Ridgecrest, and FORESEE-urban DAS array. The analysis illustrates distinct SNR between DAS arrays and between internal sections. For the internal section with similar SNR, variations on the waveform are predominantly resulted from axis orientation relative to the wave propagation direction. All the three DAS array exhibit capability of capturing low-frequency signal of the earthquake wave. RFs derived from the Enid DAS array present comparable phases to the RFs obtained from broadband station.

5.2 Future work

While the Moho map from the locally deployed broadband stations covers mainly the central part of Oklahoma, data gaps remain for the Anadarko Basin area and eastern Oklahoma. With a

comprehensive velocity model of the sedimentary columns of the Anadarko Basin and advanced de-reverberation algorithm, receiver function in the Anadarko Basin might provide more reliable configuration of the crustal and mantle structure.

The high-resolution receiver function from local and regional earthquakes opens up a new scenario of receiver function application, in which local and regional earthquakes can be used in receiver function analysis. Also, the multichannel blind deconvolution works great for the densely spaced array. In the future work, it would be interesting to apply this inversion routine to another array where the basin structure is more complex than Cushing. Besides, the emerging DAS array deployment can also be a fitting situation for the multichannel inversion routine.

As the study of comparative DAS waveform analysis is in preparation for submission, some additional work, such as quantitative measurement of SNR and waveform analysis from other earthquake events, can be supplemented to the current manuscript. Additionally, a more comprehensive analysis can be conducted with DAS data from other arrays.

Appendix

The appendix chapter contains supplemental information of the RF analysis for Oklahoma deep structure imaging presented in Chapter 2.

A1. Station and event information

A total of 221 teleseismic events and 169 stations are used in this study for receiver function analysis. Detailed information about the station and events is listed below. The total number of events used for preliminary RF calculation and prescreened number of RF for depth-conversion and H-k stacking are shown in the figure in section III.

Table A 1 Stations used in the study chapter 2.

Station	Longitude	Latitude	Elevation (m)
GS-OK025-00	-97.338	35.581	348
GS-OK029-00	-97.455	35.797	333
GS-OK030-00	-96.784	35.928	289
GS-OK031-00	-96.839	35.953	290
GS-OK032-00	-98.21	36.804	345
GS-OK033-00	-96.938	36.044	258
GS-OK034-00	-96.713	36.01	254
GS-OK035-00	-98.71	36.708	485
GS-OK036-00	-98.632	36.506	460
GS-OK037-00	-98.745	36.508	468
GS-OK038-00	-98.742	36.478	443
GS-OK039-00	-98.652	36.382	400
GS-OK040-00	-98.674	36.483	453
GS-OK041-00	-98.533	36.467	445
GS-OK042-00	-98.831	36.403	442
GS-OK043-00	-98.746	36.433	406
GS-OK044-00	-96.796	36.373	290
GS-OK045-00	-96.925	36.448	284
GS-OK046-00	-96.907	36.397	294
GS-OK047-00	-96.724	36.469	253
GS-OK048-00	-96.944	36.416	295
GS-OK049-00	-97.304	36.407	327
GS-OK050-00	-96.982	36.395	315

GS-OK051-00	-96.836	36.505	261
GS-OK052-00	-96.803	35.994	259
GS-OK053-00	-96.788	36.014	280
NX-STN01-	-97.655	35.833	316
NX-STN02-	-97.507	35.951	342
NX-STN03-	-97.186	35.926	276
NX-STN05-	-96.645	35.847	285
NX-STN07-	-97.797	36.083	345
NX-STN08-	-97.492	36.179	359
NX-STN09-	-97.267	36.176	310
NX-STN11-	-96.732	36.159	252
NX-STN12-	-96.492	36.259	260
NX-STN13-	-97.821	36.307	343
NX-STN15-	-97.375	36.349	316
NX-STN16-	-97.127	36.349	294
NX-STN17-	-96.908	36.4	299
NX-STN18-	-96.647	36.418	255
NX-STN19-	-97.903	36.683	337
NX-STN20-	-97.743	36.521	339
NX-STN21-	-97.561	36.752	333
NX-STN22-	-97.411	36.565	312
NX-STN23-	-97.197	36.655	296
NX-STN24-	-97.854	36.92	344
NX-STN26-	-97.208	36.926	353
NX-STN33-	-96.721	35.657	272
NX-STN35-	-96.79	35.442	320
O2-ARCA-	-97.27	35.743	323
O2-CHAN-	-96.785	35.653	266
O2-CRES-	-97.534	36.037	311
O2-DOVR-	-97.988	35.954	337
O2-DRUM-	-96.605	35.919	296
O2-FW01-	-98.941	36.495	431
O2-FW02-	-98.729	36.378	434
O2-FW03-	-99.173	36.527	628
O2-FW04-	-98.665	36.596	448
O2-FW05-	-98.605	36.47	444
O2-FW06-	-98.499	36.514	420
O2-FW07-	-98.801	36.45	404
O2-FW08-	-98.796	36.238	554
O2-FW09-	-99.041	36.551	517
O2-GORE-	-97.947	36.786	348
O2-MRSH-	-97.695	36.132	309
O2-PERK-	-97.13	35.926	288
O2-PERY-	-97.235	36.26	209
O2-PW01-	-96.929	36.402	322
O2-PW02-	-96.858	36.419	314
O2-PW05-	-96.964	36.485	289
O2-PW06-	-96.972	36.421	303
O2-PW09-	-96.817	36.448	291

O2-PW10-	-96.831	36.366	297
O2-PW13-	-96.818	36.328	290
O2-PW15-	-97.014	36.469	270
O2-PW18-	-97.044	36.279	299
O2-PW19-	-97.036	36.569	301
O2-SC01-	-97.82	35.185	373
O2-SC02-	-97.389	34.798	310
O2-SC04-	-97.473	34.364	300
O2-SC05-	-97.833	35.519	388
O2-SC06-	-97.521	35.073	342
O2-SC07-	-98.214	34.934	349
O2-SC08-	-96.393	34.687	200
O2-SC10-	-98.271	35.423	502
O2-SC11-	-98.741	35.183	414
O2-SC12-	-99.355	34.922	472
O2-SC13-	-96.946	34.728	363
O2-SC14-	-98.244	34.452	339
O2-SC15-	-99.501	35.607	550
O2-SC16-	-98.815	35.975	500
O2-SC17-	-97.598	34.916	1126
O2-SC18-	-97.554	36.503	1051
O2-SC19-	-97.843	36.22	1116
O2-SC20-	-98.441	35.403	490
O2-SHWN-	-97.023	35.343	320
O2-SMNL-	-96.565	35.294	317
O2-TUTT-	-97.756	35.238	407
OK-AMES-	-98.193	36.336	394
OK-BCOK-	-97.609	35.657	302
OK-BLOK-	-97.215	36.761	301
OK-CCOK-	-97.656	35.357	378
OK-CHOK-	-97.061	35.561	338
OK-CROK-	-97.983	36.505	403
OK-CSTR-	-98.689	35.646	516
OK-DEOK-	-96.498	35.843	291
OK-ELIS-	-99.418	36.065	641
OK-FNO-01	-97.401	35.257	360
OK-FRLY-	-97.452	35.415	385
OK-HTCH-	-98.333	36.017	347
OK-MOOR-	-97.659	35.342	371
OK-NOKA-	-98.932	36.635	476
OK-OKCFA-	-97.451	35.415	385
OK-QUOK-	-96.708	36.171	296
OK-SMO-	-97.475	35.523	357
OK-SWND-	-97.438	35.405	390
OK-U32A-	-99.001	36.38	525
OK-W35A-	-96.874	35.153	322
OK-X34A-	-97.833	34.601	364
OK-X37A-	-95.371	34.589	207
XR-ALF1	-97.533	36.652	292

XR-ALL1	-97.575	36.432	357
XR-BC01	-97.396	36.543	308
XR-BC02	-97.45	36.521	304
XR-BER1	-97.839	36.628	320
XR-BLA1	-97.538	36.542	318
XR-BRY1	-97.647	36.716	309
XR-BUF1	-97.72	36.583	337
XR-BUF2	-97.696	36.519	325
XR-CAR1	-97.431	36.714	311
XR-DIR1	-97.529	36.783	232
XR-ENI1	-97.788	36.418	361
XR-GLE1	-97.327	36.547	301
XR-GRA1	-97.507	36.502	310
XR-HAC1	-97.802	36.297	331
XR-KRE1	-97.832	36.581	330
XR-LIB1	-97.777	36.72	320
XR-LIB2	-97.734	36.707	311
XR-MAR1	-97.543	36.232	337
XR-MED2	-97.712	36.781	323
XR-MIL1	-97.197	36.659	293
XR-NOB2	-97.627	36.562	326
XR-NUM1	-97.618	36.82	337
XR-OAK1	-97.459	36.369	319
XR-OLI1	-97.561	36.346	336
XR-OWE2	-97.376	36.63	309
XR-PER1	-97.261	36.365	311
XR-REN1	-97.723	36.644	313
XR-REN2	-97.765	36.624	319
XR-RR01	-97.346	36.46	291
XR-SF01	-97.669	36.659	307
XR-SF02	-97.598	36.641	313
XR-SF03	-97.659	36.617	308
XR-WOO2	-97.48	36.25	355
XR-WR01	-97.379	36.503	294
XR-WV01	-97.377	36.292	328
NX-STN10-	-96.937	36.146	287
NX-STN14-	-97.626	36.47	329
NX-STN31-	-97.443	35.758	329
NX-STN32-	-97.155	35.681	292
NX-STN34-	-97.11	35.442	339
O2-FW10-	-98.718	36.506	457
O2-POCA-	-98.075	35.218	396
O2-PW07-	-96.765	36.504	282
O2-PW17-	-96.7	36.245	324
O2-PW30-	-96.822	36.417	314
O2-SC03-	-97.849	34.94	349
O2-SC09-	-97.366	34.545	296
OK-BLUF-	-97.609	35.657	302

Table A 2 Teleseismic events information of receiver function analysis in chapter 2.

Longitude	Latitude	Event depth	Magnitude	Date	Time
-42.669	10.691	17.5	6.5	6/24/2013	22:04:14
-78.125	5.718	18.6	6.6	8/13/2013	15:43:16
-175.214	51.5	30.2	7	8/30/2013	16:25:02
-174.695	51.481	30.3	6.5	9/4/2013	2:32:32
-74.601	-15.9	38.2	7	9/25/2013	16:42:43
141.5	48.55	10	6.6	10/11/2013	9:28:47
23.372	35.528	46.9	6.8	10/12/2013	13:11:54
144.754	37.146	14.7	7.1	10/25/2013	17:10:17
-73.151	-35.402	11.9	6.3	10/30/2013	2:51:49
-71.502	-30.314	19.8	6.5	10/31/2013	23:03:59
162.143	54.677	60.5	6.5	11/12/2013	7:03:52
-66.868	18.992	30.9	6.3	1/13/2014	4:01:05
-58.972	14.596	28.3	6.5	2/18/2014	9:27:15
-80.935	-5.672	26.5	6.3	3/15/2014	23:51:32
-70.616	-19.905	9.4	6.7	3/16/2014	21:16:29
-70.828	-20.06	5.3	6.4	3/17/2014	5:11:33
-70.788	-19.619	17.1	8.1	4/1/2014	23:46:47
-70.501	-20.364	10.6	6.6	4/3/2014	1:58:29
-70.491	-20.589	12	7.7	4/3/2014	2:43:14
-70.541	-20.749	13	6.5	4/3/2014	5:26:14
-114.763	-49.925	7.1	6.4	5/12/2014	18:38:37
-82.24	7.145	13.1	6.5	5/13/2014	6:35:25
25.37	40.276	8.2	6.9	5/24/2014	9:25:03
178.643	51.703	102.1	7.9	6/23/2014	20:53:10
176.782	52.009	23.2	6.4	6/24/2014	3:15:39
-175.514	-15.101	26	6.4	6/29/2014	15:52:28
-175.458	-15.235	26	6.6	6/29/2014	17:15:12
142.452	37.005	20	6.6	7/11/2014	19:22:01
142.39	36.97	12	6.5	7/11/2014	19:22:06
-174.452	-15.824	227.3	6.3	7/19/2014	12:27:10
148.784	44.642	61	6.3	7/20/2014	18:32:48
-71.442	-32.695	32	6.4	8/23/2014	22:32:23
-73.535	-14.52	70	6.8	8/24/2014	23:21:42
-73.45	-14.589	74.4	6.8	8/24/2014	23:21:43
-151.916	61.986	106.9	6.3	9/25/2014	17:51:18
-110.924	-32.299	4.2	7	10/9/2014	2:14:30
-110.92	-32.161	10.5	6.6	10/9/2014	2:32:06
-82.687	7.94	20	6.6	12/8/2014	8:54:53
-82.657	6.109	7.9	6.5	1/7/2015	5:07:06
-67.15	-32.648	172.7	6.3	2/2/2015	10:49:48
-66.662	-23.065	203.6	6.7	2/11/2015	18:57:20
-32.021	52.51	16.9	7.1	2/13/2015	18:59:14
143.177	39.947	10.8	6.7	2/16/2015	23:06:28
-69.188	-18.354	127.1	6.4	3/23/2015	4:51:38

-172.905	-15.439	15.2	6.3	3/30/2015	8:18:02
-173.335	-15.337	31.2	6.3	4/7/2015	0:46:21
142.022	38.901	39.3	6.8	5/12/2015	21:12:59
-156.676	56.708	64.6	6.8	5/29/2015	7:00:08
-73.667	-36.335	17.4	6.4	6/20/2015	2:10:08
148.004	43.97	51.1	6.3	7/7/2015	5:10:28
-58.57	13.801	19.4	6.5	7/16/2015	15:16:33
-169.535	52.276	27.8	6.9	7/27/2015	4:49:46
-153.325	59.972	121.2	6.4	7/29/2015	2:35:58
-71.674	-31.573	22.4	8.3	9/16/2015	22:54:33
-71.745	-31.618	26.7	6.4	9/16/2015	22:59:15
-71.688	-31.424	27	6.5	9/17/2015	3:55:15
-71.81	-31.52	23	6.8	9/17/2015	4:10:27
-71.804	-31.517	23	6.7	9/17/2015	4:10:28
-71.379	-31.728	35	6.6	9/21/2015	17:40:00
-71.322	-30.815	46	6.3	9/26/2015	2:51:19
-71.452	-30.88	46	6.8	11/7/2015	7:31:44
-173.075	51.639	15	6.5	11/9/2015	16:03:46
-72.007	-29.507	12	6.9	11/11/2015	1:54:39
-72.059	-29.51	10	6.9	11/11/2015	2:46:20
20.6	38.67	11	6.5	11/17/2015	7:10:07
141.087	44.476	238.8	6.2	1/11/2016	17:08:04
-63.329	-19.76	582.6	6.1	1/14/2016	3:25:28
142.781	41.972	46	6.7	1/14/2016	3:25:34
-3.682	35.649	12	6.3	1/25/2016	4:22:03
158.513	54.006	163.2	7.2	1/30/2016	3:25:11
-71.584	-30.572	29	6.3	2/10/2016	0:33:05
-173.942	51.565	19	6.3	3/12/2016	18:06:45
-174.142	51.514	17	6	3/19/2016	1:35:12
-60.702	17.996	26	6	3/19/2016	11:26:33
162.813	54.294	30	6.4	3/20/2016	22:50:20
-157.932	57.008	11.4	6.2	4/2/2016	5:50:00
-79.922	0.382	20.6	7.8	4/16/2016	23:58:37
-80.21	0.639	14	6.2	4/20/2016	8:33:47
-80.035	0.708	10	6	4/20/2016	8:35:11
-80.504	-0.292	10	6	4/22/2016	3:03:42
-79.79	0.426	16	6.7	5/18/2016	7:57:03
-79.616	0.495	30	6.9	5/18/2016	16:46:44
-45.14	22.658	10	6.1	6/21/2016	16:26:34
-173.201	-15.083	8	6	7/10/2016	13:44:41
-79.638	0.581	21	6.3	7/11/2016	2:11:05
-70.507	-26.105	72	6.1	7/25/2016	17:26:50
-66.026	-22.309	270	6.2	8/4/2016	14:15:13
143.68	40.356	10	6	8/20/2016	9:01:26
143.754	40.293	10	6	8/20/2016	15:58:04
13.188	42.723	4.4	6.2	8/24/2016	1:36:33
-17.829	-0.047	10	7.1	8/29/2016	4:29:58
168.542	54.415	8	6.1	9/5/2016	22:54:04
-76.954	-5.573	121	6.1	9/10/2016	10:08:20

-76.169	7.374	18	6	9/14/2016	1:58:32
-174.872	-15.54	10	6.1	10/26/2016	5:19:51
13.043	42.934	10	6.1	10/26/2016	19:18:08
13.088	42.855	10	6.6	10/30/2016	6:40:19
-70.996	-35.103	90.8	6.4	11/4/2016	16:20:44
141.566	38.497	42.4	6.1	11/11/2016	21:43:00
-68.765	-31.643	115.8	6.4	11/20/2016	20:57:44
-68.765	-31.643	115.8	-12345	11/20/2016	21:08:02
141.402	37.392	11.4	6.9	11/21/2016	20:59:49
141.402	37.392	11.4	-12345	11/21/2016	21:11:39
-70.823	-15.294	10	6.2	12/1/2016	22:40:26
-70.823	-15.294	10	-12345	12/1/2016	22:49:16
174.201	52.244	26.9	6	12/3/2016	9:23:35
174.201	52.244	26.9	-12345	12/3/2016	9:32:43
-70.97	-9.966	622.5	6.4	12/18/2016	13:30:11
-70.97	-9.966	622.5	-12345	12/18/2016	13:37:30
-73.94	-43.405	38	7.6	12/25/2016	14:22:27
-73.94	-43.405	38	-12345	12/25/2016	14:33:47
176.058	-19.354	12	-12345	1/3/2017	22:05:08
-92.404	74.392	31	6	1/8/2017	23:47:14
-92.404	74.392	31	-12345	1/8/2017	23:53:27
-66.659	-23.861	222	6.3	2/18/2017	12:10:18
-66.659	-23.861	222	-12345	2/18/2017	12:19:46
-63.905	-19.281	596	6.5	2/21/2017	14:09:04
-63.905	-19.281	596	-12345	2/21/2017	14:17:42
172.199	52.798	10	6.1	3/27/2017	10:50:19
162.787	56.938	15.5	6.6	3/29/2017	4:09:24
-67.766	-23.271	155	6.2	4/15/2017	8:19:43
-72.006	-33.036	21	6	4/23/2017	2:36:08
-72.045	-33.029	28	6.9	4/24/2017	21:38:31
-136.676	59.83	8	6.2	5/1/2017	12:31:55
-136.704	59.829	2.5	6.2	5/1/2017	14:18:15
-178.636	51.755	10	6.2	5/8/2017	17:00:47
170.91	54.029	8.2	6.8	6/2/2017	22:24:48
26.371	38.915	12	6.3	6/12/2017	12:28:39
-80.493	-0.288	13	6	6/30/2017	22:29:45
168.647	54.583	10	6.3	7/17/2017	11:05:09
168.815	54.472	11	7.7	7/17/2017	23:34:14
-73.63	-16.421	44.9	6.4	7/18/2017	2:05:20
-49.326	13.396	10	6	7/27/2017	17:53:25
-13.663	-1.091	10	6.6	8/18/2017	2:59:22
144.66	37.981	11	6.1	9/20/2017	16:37:16
144.02	37.503	9	6.2	10/6/2017	7:59:33
176.808	52.45	111.8	6.6	10/8/2017	22:34:34
-69.641	-18.521	82.4	6.3	10/10/2017	6:32:21
-173.168	-15.32	10	6.8	11/4/2017	9:00:19
-175.074	-14.726	6	6	11/20/2017	18:51:07
-23.432	-1.08	10	6.5	11/30/2017	6:32:51
-80.311	-0.489	16	6.2	12/3/2017	11:19:05

-74.71	-15.759	39	7.1	1/14/2018	9:18:46
-69.456	-18.852	116	6.3	1/21/2018	1:06:43
-149.073	56.046	25	7.9	1/23/2018	9:31:43
142.432	41.103	31	6.3	1/24/2018	10:51:19
166.446	55.542	11.2	6.2	1/25/2018	2:10:35
-63.006	-20.659	559	6.8	4/2/2018	13:40:35
-71.557	-30.986	76.1	6.2	4/10/2018	10:19:34
-111.654	-24.26	10	6	5/2/2018	6:32:49
-154.997	19.313	2.1	6.9	5/4/2018	22:32:54
157.84	51.499	45	6.1	7/6/2018	1:40:05
-145.3	69.562	2.2	6.3	8/12/2018	14:58:54
-144.36	69.521	1.7	6	8/12/2018	21:15:02
-178.052	51.422	20	6.6	8/15/2018	21:56:54
-83.153	8.769	15	6.1	8/17/2018	23:22:25
-62.907	10.779	146.2	7.3	8/21/2018	21:31:48
-177.881	51.511	43.9	6	8/23/2018	3:35:16
-70.817	-11.042	609.5	7.1	8/24/2018	9:04:07
141.929	42.686	35	6.6	9/5/2018	18:07:59
-78.896	-2.345	93.5	6.2	9/7/2018	2:12:04
156.232	49.394	20	6.1	10/9/2018	7:45:12
156.297	49.29	20	6.5	10/10/2018	23:16:02
153.243	52.855	461	6.7	10/13/2018	11:10:22
20.563	37.515	14	6.8	10/25/2018	22:54:53
-69.292	-19.588	102	6.2	11/1/2018	22:19:52
-11.25	71.626	10	6.7	11/9/2018	1:49:40
-49.872	15.565	10	6.3	11/11/2018	14:04:00
162.001	55.632	50.2	6.1	11/14/2018	21:21:51
-149.955	61.346	46.7	7	11/30/2018	17:29:29
-101.072	-36.138	10	6.3	12/19/2018	1:37:41
164.699	55.1	16.6	7.3	12/20/2018	17:01:55
164.435	55.417	10	6.1	12/24/2018	12:41:19
-71.583	-8.149	571.2	6.8	1/5/2019	19:25:39
-71.42	-30.071	54.8	6.7	1/20/2019	1:32:52
-36.079	35.422	10	6.2	2/14/2019	19:57:05
-77.023	-2.199	132.4	7.5	2/22/2019	10:17:22
-70.135	-14.702	267	7	3/1/2019	8:50:43
-65.907	-17.874	359	6.3	3/15/2019	5:03:50
-76.223	4.563	122	6.1	3/23/2019	19:21:18
159.963	50.502	9	6.2	3/28/2019	22:06:49
-80.809	-1.944	18	6.2	3/31/2019	7:04:05
178.068	52.167	7.9	6.4	4/2/2019	21:35:30
143.298	40.41	18	6	4/11/2019	8:18:21
-82.833	8.623	19	6	5/12/2019	19:24:50
-105.731	-4.588	10	5.8	5/16/2019	22:52:44
-178.239	51.308	30	6.1	5/23/2019	8:45:18
-75.277	-5.813	122.4	8	5/26/2019	7:41:15
-72.082	-30.056	11	6.4	6/14/2019	0:19:12
139.48	38.637	12	6.4	6/18/2019	13:22:19
164.184	56.208	10	6.3	6/25/2019	9:05:41

164.11	56.178	10	6.3	6/26/2019	2:18:08
-82.768	8.449	26.2	6.2	6/26/2019	5:23:51
-116.744	-49.551	10	5.8	7/13/2019	7:59:34
-72.308	-34.237	25	6.8	8/1/2019	18:28:07
-113.833	-49.731	10	6	8/2/2019	5:50:55
141.609	37.76	38	6.3	8/4/2019	10:23:04
-27.875	1.039	10	5.9	8/5/2019	0:40:46
142.995	41.068	23.8	5.9	8/28/2019	23:46:40
-45.217	23.777	10	5.9	9/2/2019	22:45:49
-67.27	19.077	10	6	9/24/2019	3:23:40
-72.003	-40.816	129	6.1	9/26/2019	16:36:18
-102.774	-35.922	10	5.9	9/27/2019	15:11:30
-73.163	-35.476	11	6.7	9/29/2019	15:57:53
-13.837	-1.099	10	6.3	10/23/2019	16:08:14
-170.139	52.308	35	5.8	10/26/2019	0:41:26
-71.378	-31.812	53	6.1	11/4/2019	21:53:25
-172.85	-15.764	35	5.8	11/8/2019	9:41:14
-80.724	-45.006	35	6.3	5/20/2013	9:49:08
-71.018	-19.962	10.8	7	4/1/2014	23:57:57
140.63	46.93	10	7.6	11/9/2014	14:38:16
-172.914	-15.575	15.8	6.4	3/30/2015	8:48:26
-71.426	-31.562	28.4	7	9/16/2015	23:18:42
-71.65	-31.104	42.3	6.4	9/17/2015	1:41:06
-153.339	59.62	125.6	7.1	1/24/2016	10:30:30
-161.513	54.427	31	6	12/31/2018	2:35:38
-85.266	1.451	10	5.8	4/5/2019	18:46:43
-172.716	-15.4	10	5.8	4/12/2019	12:23:04
-177.414	-14.658	10	5.9	8/22/2019	19:27:12

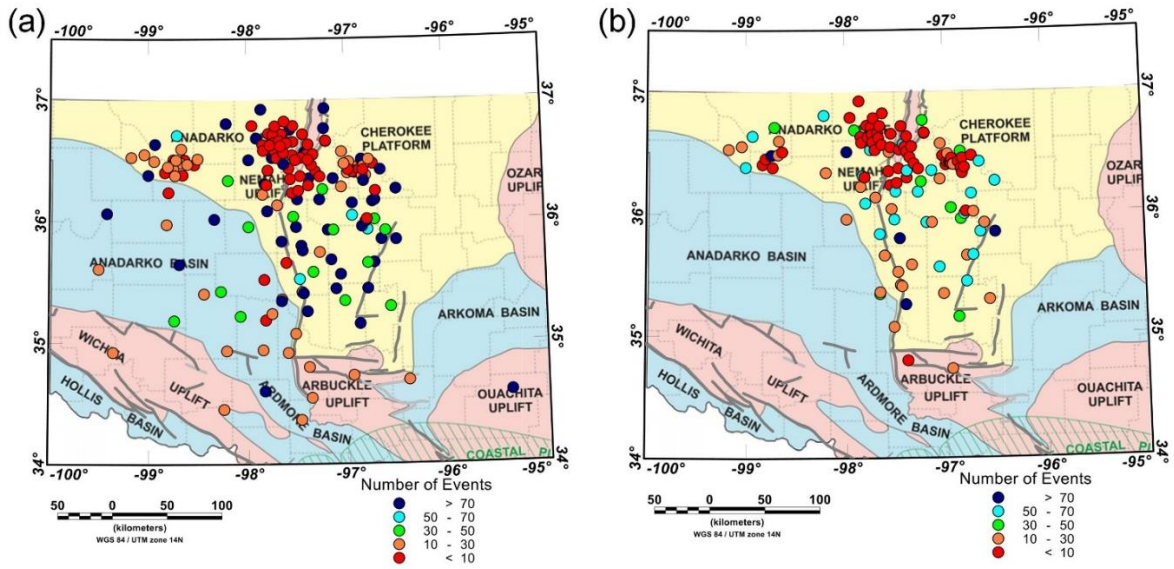


Figure A 1 Number of events used in this study and for deriving the Moho map. a) the total number of events used in each station. b) number of prescreened events used in the H-k stacking and depth-conversion

A2. H − κ stacking results and Moho depth from depth converted RFs

Table A 3 Moho depth and Vp/Vs ratio of each station from H − κ stacking.

Station	Longitude	Latitude	Moho depth	Moho depth error	Velocity ratio	Velocity ratio error	Num of events
GS-OK025	-97.338	35.581	46.22	1.574	1.7312	0.0303	31
GS-OK029	-97.455	35.797	38.244	0.266	1.8688	0.0076	87
GS-OK030	-96.784	35.928	53.52	0.396	2.1	0	31
GS-OK031	-96.839	35.953	43.1	0.463	1.7824	0.0122	46
GS-OK032	-98.21	36.804	36.412	0.094	2.0994	0.0047	70
GS-OK033	-96.938	36.044	51.372	8.614	1.6648	0.1563	42
GS-OK034	-96.713	36.01	35	0	1.6	0	20
GS-OK035	-98.71	36.708	60	0	2.1	0	40
GS-OK036	-98.632	36.506	46.368	0.757	1.796	0.0198	9
GS-OK037	-98.745	36.508	47.016	0.998	1.9152	0.0272	8
GS-OK038	-98.742	36.478	51.604	0.423	1.69	0.0105	79
GS-OK039	-98.652	36.382	51.064	0.991	1.6966	0.0526	9
GS-OK040	-98.674	36.483	48.76	1.365	1.7682	0.0314	21
GS-OK041	-98.533	36.467	56.372	3.183	2.1	0	9
GS-OK042	-98.831	36.403	46.508	0.948	1.9908	0.0333	9
GS-OK043	-98.746	36.433	37.276	0.906	2.0094	0.037	17
GS-OK044	-96.796	36.373	59.128	1.074	2.0038	0.0227	10
GS-OK045	-96.925	36.448	39.428	1.49	1.8496	0.046	9
GS-OK046	-96.907	36.397	38.612	1.258	1.8644	0.0376	14

GS-OK047	-96.724	36.469	43.728	1.179	1.7368	0.0295	2
GS-OK048	-96.944	36.416	39.384	0.734	1.842	0.021	72
GS-OK049	-97.304	36.407	38.576	2.045	1.866	0.0652	5
GS-OK050	-96.982	36.395	38.18	1.295	1.9038	0.043	10
GS-OK051	-96.836	36.505	47.768	13.231	1.9724	0.2373	48
GS-OK052	-96.803	35.994	38.556	0.464	1.9346	0.0144	68
GS-OK053	-96.788	36.014	38.328	0.892	1.912	0.0319	9
NX-STN01-	-97.655	35.833	43.276	0.44	1.8082	0.0117	53
NX-STN02-	-97.507	35.951	40.6	0.434	1.9056	0.0144	58
NX-STN03-	-97.186	35.926	57.672	0.787	1.9854	0.0178	52
NX-STN05-	-96.645	35.847	41.38	0.365	1.8694	0.0121	58
NX-STN07-	-97.797	36.083	41.844	0.39	1.8224	0.0116	53
NX-STN08-	-97.492	36.179	42.44	0.513	1.7752	0.0164	52
NX-STN09-	-97.267	36.176	39.324	0.426	1.8374	0.0124	63
NX-STN11-	-96.732	36.159	42.484	0.489	1.834	0.0148	64
NX-STN12-	-96.492	36.259	43.428	0.434	1.7798	0.0122	59
NX-STN13-	-97.821	36.307	36.564	5.211	1.6676	0.0754	51
NX-STN15-	-97.375	36.349	43.04	0.501	1.744	0.0125	54
NX-STN16-	-97.127	36.349	39.128	0.402	1.8538	0.0153	65
NX-STN17-	-96.908	36.4	40.772	0.513	1.81	0.0158	53
NX-STN18-	-96.647	36.418	38.984	0.295	1.951	0.0133	58
NX-STN19-	-97.903	36.683	35.656	4.404	1.9078	0.0924	48
NX-STN20-	-97.743	36.521	41.076	0.474	1.8378	0.016	55
NX-STN21-	-97.561	36.752	43.64	7.121	1.7674	0.1134	66
NX-STN22-	-97.411	36.565	41.52	0.482	1.7858	0.0143	56
NX-STN23-	-97.197	36.655	40.748	0.597	1.8456	0.0173	57
NX-STN24-	-97.854	36.92	59.232	0.971	1.9606	0.0222	6
NX-STN26-	-97.208	36.926	39.852	0.586	1.8392	0.0181	54
NX-STN33-	-96.721	35.657	41.296	0.49	1.8064	0.0147	52
NX-STN35-	-96.79	35.442	41.668	0.431	1.8862	0.0137	58
O2-ARCA-	-97.27	35.743	59.036	2.224	2.0656	0.0361	11
O2-CHAN-	-96.785	35.653	41.372	0.677	1.8902	0.0222	29
O2-CRES-	-97.534	36.037	41.604	1.281	1.8244	0.0359	13
O2-DOVR-	-97.988	35.954	49.88	1.837	1.7294	0.033	20
O2-DRUM	-96.605	35.919	40.544	0.619	1.8282	0.0197	24
O2-FW01-	-98.941	36.495	46.612	1.579	1.9186	0.0446	8
O2-FW02-	-98.729	36.378	39.504	0.99	1.8224	0.0333	9
O2-FW03-	-99.173	36.527	46.496	6.072	1.8018	0.1301	12
O2-FW04-	-98.665	36.596	35.64	1.15	1.727	0.0355	12
O2-FW05-	-98.605	36.47	40.5	8.257	1.721	0.1368	9
O2-FW06-	-98.499	36.514	59.008	4.5	2.0246	0.0657	12
O2-FW07-	-98.801	36.45	53.396	2.27	2.018	0.0477	8
O2-FW08-	-98.796	36.238	41.132	1.537	1.7192	0.0417	5
O2-FW09-	-99.041	36.551	48.62	1.181	1.7746	0.0302	11
O2-GORE-	-97.947	36.786	44.508	1.233	1.7104	0.0299	9
O2-MRSH-	-97.695	36.132	41.68	4.482	1.8406	0.1021	14
O2-PERK-	-97.13	35.926	35.344	1.846	1.6158	0.0138	25
O2-PERY-	-97.235	36.26	42.172	0.695	1.7456	0.0182	32
O2-PW01-	-96.929	36.402	37.908	5.172	1.9108	0.1358	3
O2-PW02-	-96.858	36.419	38.528	1.847	1.8824	0.0633	5
O2-PW05-	-96.964	36.485	58.18	4.383	1.8226	0.081	16
O2-PW06-	-96.972	36.421	41.844	2.458	1.8136	0.0697	3
O2-PW07-	-96.765	36.504	35	0	1.9148	0.0099	2
O2-PW09-	-96.817	36.448	42.34	2.454	1.7802	0.0525	10
O2-PW10-	-96.831	36.366	48.2	0	1.7	0	1
O2-PW13-	-96.818	36.328	42.544	0.462	2.1	0	10
O2-PW15-	-97.014	36.469	41.168	1.478	1.7674	0.0365	9
O2-PW18-	-97.044	36.279	40.416	1.525	1.8268	0.0407	11
O2-PW19-	-97.036	36.569	35.012	0.123	1.9912	0.0146	14

O2-SC01-	-97.82	35.185	49.532	2.804	2.0152	0.0754	5
O2-SC02-	-97.389	34.798	53.136	0.444	2.0978	0.0107	7
O2-SC04-	-97.473	34.364	53.268	14.234	1.6456	0.2238	12
O2-SC05-	-97.833	35.519	47.296	1.612	2.056	0.0528	4
O2-SC06-	-97.521	35.073	44.82	2.24	1.818	0.0682	14
O2-SC07-	-98.214	34.934	49.932	0.401	1.6012	0.0064	9
O2-SC08-	-96.393	34.687	59.936	0.185	2.0464	0.0216	8
O2-SC10-	-98.271	35.423	35.14	0.477	1.619	0.016	14
O2-SC11-	-98.741	35.183	48.032	0.527	1.6008	0.0054	11
O2-SC12-	-99.355	34.922	58.504	1.664	1.7172	0.0266	14
O2-SC13-	-96.946	34.728	45.852	11.985	1.7812	0.2056	11
O2-SC14-	-98.244	34.452	37.716	1.002	1.6	0	15
O2-SC15-	-99.501	35.607	46.336	12.653	1.6738	0.1791	5
O2-SC16-	-98.815	35.975	47.392	6.202	1.6746	0.058	13
O2-SC17-	-97.598	34.916	38.316	6.912	1.6506	0.0728	16
O2-SC18-	-97.554	36.503	47.856	0.999	2.0248	0.0322	18
O2-SC19-	-97.843	36.22	38.24	1.051	1.8946	0.0334	15
O2-SC20-	-98.441	35.403	39.704	0.752	1.6084	0.0183	10
O2-SHWN	-97.023	35.343	43.188	0.33	1.6	0	19
O2-SMNL-	-96.565	35.294	51.132	1.082	1.7632	0.0313	22
O2-TUTT-	-97.756	35.238	48.348	1.667	1.7838	0.0801	8
OK-AMES-	-98.193	36.336	45.26	21.906	1.8606	0.3562	16
OK-BCOK-	-97.609	35.657	58.908	2.505	2.0804	0.0338	29
OK-BLOK-	-97.215	36.761	46.652	11.286	1.744	0.1843	45
OK-CCOK-	-97.656	35.357	43.396	1.102	1.7924	0.0318	14
OK-CHOK-	-97.061	35.561	59.98	0.119	2.1	0	69
OK-CROK-	-97.983	36.505	37.924	8.066	1.6864	0.1229	86
OK-CSTR-	-98.689	35.646	35.168	0.383	1.636	0.0097	40
OK-DEOK-	-96.498	35.843	37.384	0.191	1.6	0	72
OK-ELIS-	-99.418	36.065	43.436	0.725	2.0326	0.0243	52
OK-FNO-01	-97.401	35.257	35.008	0.078	2.0604	0.0055	78
OK-FRLY-	-97.452	35.415	41.472	0.998	1.8922	0.0302	19
OK-HTCH-	-98.333	36.017	47.608	1.054	1.6408	0.0185	51
OK-MOOR-	-97.659	35.342	45.016	0.746	1.77	0.0181	48
OK-NOKA-	-98.932	36.635	42.444	0.793	1.7866	0.0212	58
OK-OKCFA-	-97.451	35.415	44.088	12.592	1.8246	0.2443	6
OK-QUOK-	-96.708	36.171	54.832	0.714	2.0332	0.0188	66
OK-SMO-	-97.475	35.523	42.568	0.391	1.6	0	24
OK-SWND-	-97.438	35.405	51.548	0.586	1.9782	0.0162	27
OK-U32A-	-99.001	36.38	43.84	0.525	1.634	0.0131	54
OK-W35A-	-96.874	35.153	40.244	15.135	1.76	0.4618	46
OK-X34A-	-97.833	34.601	45.312	0.739	1.8906	0.0203	42
OK-X37A-	-95.371	34.589	38.408	5.26	2.0928	0.0998	54
XR-ALF1	-97.533	36.652	54.468	2.631	1.8258	0.0462	9
XR-ALL1	-97.575	36.432	38.876	9.037	1.8894	0.3082	7
XR-BC01	-97.396	36.543	53.648	13.905	1.87	0.235	3
XR-BC02	-97.45	36.521	57.54	1.629	1.8296	0.0331	8
XR-BER1	-97.839	36.628	39.568	1.143	1.6678	0.0325	4
XR-BLA1	-97.538	36.542	55.564	18.749	2.0696	0.1258	6
XR-BRY1	-97.647	36.716	38.588	0.719	1.9218	0.0246	9
XR-BUF1	-97.72	36.583	35.036	0.152	2.0226	0.0111	8
XR-BUF2	-97.696	36.519	37.34	6.189	1.709	0.1064	10
XR-CAR1	-97.431	36.714	44.828	12.032	1.7592	0.1517	9
XR-DIR1	-97.529	36.783	58.08	1.32	1.6124	0.0226	4
XR-ENI1	-97.788	36.418	42.616	13.617	1.9984	0.2748	9
XR-GLE1	-97.327	36.547	42.108	1.459	1.764	0.0394	6
XR-GRA1	-97.507	36.502	51.092	19.676	1.8084	0.0639	9
XR-HAC1	-97.802	36.297	44.96	8.325	1.7708	0.1258	7
XR-KRE1	-97.832	36.581	52.576	0.729	1.6812	0.0162	5

XR-LIB1	-97.777	36.72	41.496	0.846	1.7524	0.0222	6
XR-LIB2	-97.734	36.707	57.54	0.659	1.605	0.0099	5
XR-MAR1	-97.543	36.232	41.012	0.962	1.8074	0.0293	8
XR-MED2	-97.712	36.781	40.06	1.764	1.8604	0.0521	7
XR-MIL1	-97.197	36.659	42.6	1.419	1.7774	0.0394	3
XR-NOB2	-97.627	36.562	41.608	1.7	1.8272	0.0501	4
XR-NUM1	-97.618	36.82	35.348	1.481	2.0042	0.0419	4
XR-OAK1	-97.459	36.369	56.8	0	1.86	0	1
XR-OLI1	-97.561	36.346	41.432	0.789	1.7778	0.0261	7
XR-OWE2	-97.376	36.63	42.732	8.723	1.786	0.0365	7
XR-PER1	-97.261	36.365	38.82	0.9	1.8244	0.0291	10
XR-REN1	-97.723	36.644	53.86	1.095	1.6544	0.021	6
XR-REN2	-97.765	36.624	52.028	4.894	1.6916	0.0977	7
XR-RR01	-97.346	36.46	41.644	1.021	1.7544	0.0305	8
XR-SF01	-97.669	36.659	40.636	0.936	1.8408	0.0324	6
XR-SF02	-97.598	36.641	43.424	17.619	1.722	0.0703	7
XR-SF03	-97.659	36.617	41.624	1.096	1.8206	0.033	3
XR-WOO2	-97.48	36.25	38.472	1.171	1.845	0.0374	3
XR-WR01	-97.379	36.503	56.932	8.552	1.8238	0.1577	8
XR-WV01	-97.377	36.292	36.92	0.913	1.9034	0.036	6

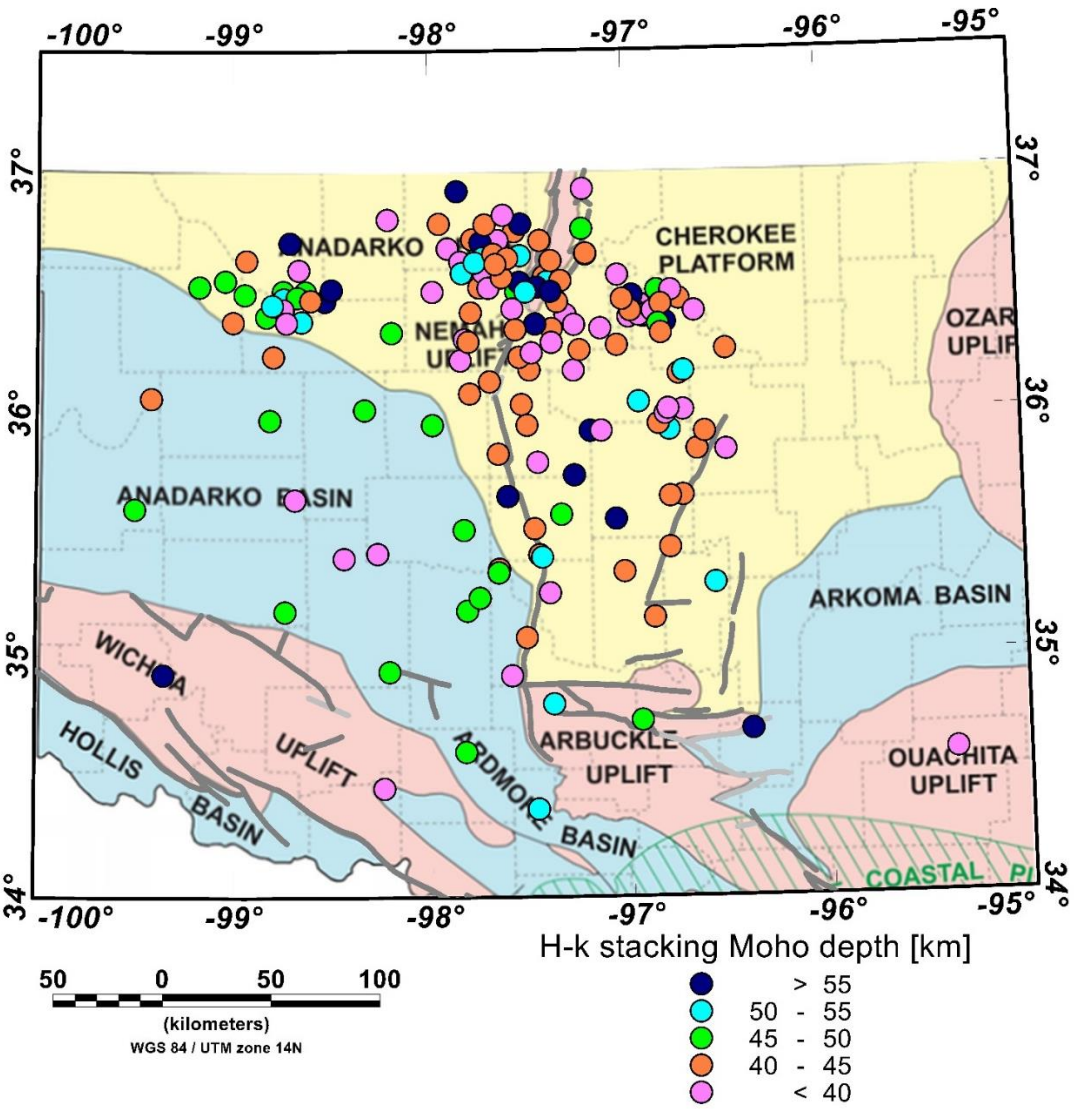


Figure A 2 The Moho depth of each station obtained by H-kappa stacking. The result is shown in five intervals from 40 km to 55 km. Note the compelling scattering of results for nearby stations where the depth of Moho fluctuates dramatically in short distances.

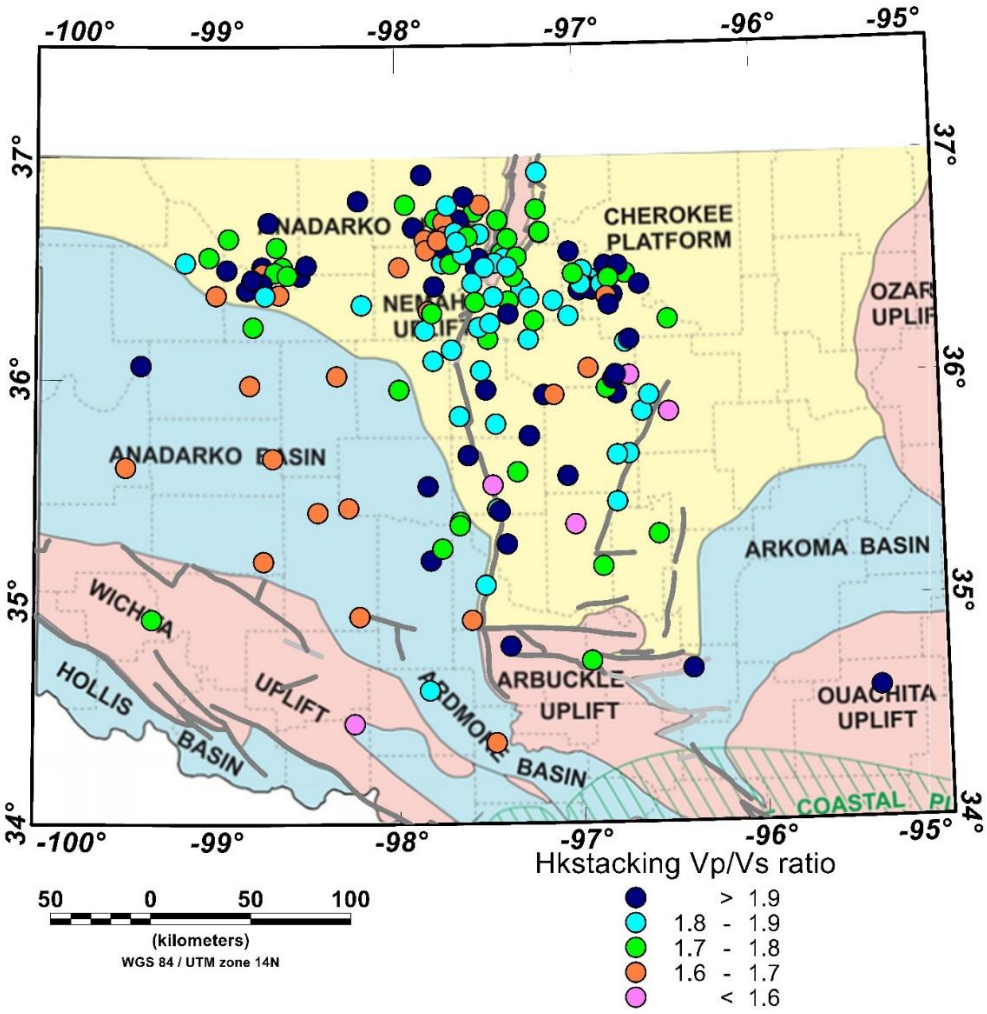


Figure A 3 The Vp/Vs ratio of each station obtained from H-kappa stacking. The result is shown in five intervals from 1.6 to 1.9. Note the scattering of the Vp/Vs ratio is even more significant than the Moho depth result, where the crustal Vp/Vs ratio oscillates greatly across the study area.

Table A 4 Moho depth from converted RFs by semi-automatically picking

Longitude	Latitude	Station	Moho depth (km)	Moho depth error	Number of events
-99.173	36.527	O2-FW03-	50.14	1.80	12
-99.041	36.551	O2-FW09-	50.19	2.01	11
-99.001	36.38	OK-U32A-	51.00	3.35	54
-98.932	36.635	OK-NOKA-	50.37	3.75	58
-98.831	36.403	GS-OK042-00	52.30	3.99	9
-98.801	36.45	O2-FW07-	50.51	4.07	8
-98.742	36.478	GS-OK038-00	49.19	3.71	79
-98.729	36.378	O2-FW02-	50.57	3.26	9
-98.71	36.708	GS-OK035-00	48.24	4.04	40
-98.674	36.483	GS-OK040-00	48.31	3.97	21
-98.665	36.596	O2-FW04-	49.12	3.14	12
-98.632	36.506	GS-OK036-00	46.00	3.00	9
-98.21	36.804	GS-OK032-00	43.00	3.31	70
-98.193	36.336	OK-AMES-	41.72	4.14	16
-97.988	35.954	O2-DOVR-	42.32	4.07	20
-97.983	36.505	OK-CROK-	43.41	3.57	86
-97.947	36.786	O2-GORE-	40.03	2.93	9
-97.903	36.683	NX-STN19-	39.84	2.29	48
-97.854	36.92	NX-STN24-	43.92	1.43	6
-97.843	36.22	O2-SC19-	41.57	3.40	15
-97.839	36.628	XR-BER1	41.33	2.70	4
-97.832	36.581	XR-KRE1	44.80	2.22	5
-97.821	36.307	NX-STN13-	43.49	2.77	51
-97.802	36.297	XR-HAC1	44.00	2.51	7
-97.797	36.083	NX-STN07-	44.52	2.39	53
-97.777	36.72	XR-LIB1	45.87	3.71	6
-97.765	36.624	XR-REN2	45.01	3.33	7
-97.743	36.521	NX-STN20-	44.30	2.83	55
-97.734	36.707	XR-LIB2	44.20	2.36	5
-97.723	36.644	XR-REN1	43.58	2.76	6
-97.72	36.583	XR-BUF1	44.96	3.06	8
-97.712	36.781	XR-MED2	42.70	1.52	7
-97.696	36.519	XR-BUF2	43.35	2.99	10
-97.695	36.132	O2-MRSH-	43.67	2.28	14
-97.669	36.659	XR-SF01	43.77	2.62	6
-97.659	35.342	OK-MOOR-	45.83	2.78	48
-97.659	36.617	XR-SF03	43.83	1.97	3
-97.656	35.357	OK-CCOK-	46.26	3.21	14
-97.655	35.833	NX-STN01-	43.85	3.45	53
-97.647	36.716	XR-BRY1	44.06	2.55	9
-97.627	36.562	XR-NOB2	44.78	2.96	4
-97.618	36.82	XR-NUM1	45.05	2.24	4
-97.609	35.657	OK-BCOK-	45.64	3.85	29
-97.561	36.346	XR-OLI1	41.54	2.02	7
-97.554	36.503	O2-SC18-	42.24	2.99	18
-97.543	36.232	XR-MAR1	40.45	2.64	8

-97.538	36.542	XR-BLA1	42.42	4.16	6
-97.534	36.037	O2-CRES-	42.42	1.54	13
-97.533	36.652	XR-ALF1	43.26	1.90	9
-97.521	35.073	O2-SC06-	44.51	4.30	14
-97.507	35.951	NX-STN02-	42.55	2.05	58
-97.492	36.179	NX-STN08-	40.73	2.04	52
-97.48	36.25	XR-WOO2	40.07	0.42	3
-97.475	35.523	OK-SMO-	46.48	2.91	24
-97.455	35.797	GS-OK029-00	45.77	3.56	82
-97.452	35.415	OK-FRLY-	44.55	3.51	19
-97.45	36.521	XR-BC02	42.09	2.07	8
-97.438	35.405	OK-SWND-	44.86	3.27	27
-97.431	36.714	XR-CAR1	40.70	1.85	9
-97.411	36.565	NX-STN22-	40.90	2.25	56
-97.401	35.257	OK-FNO-01	47.13	2.80	78
-97.396	36.543	XR-BC01	40.93	1.20	3
-97.389	34.798	O2-SC02-	45.99	3.39	7
-97.379	36.503	XR-WR01	41.64	1.08	8
-97.377	36.292	XR-WV01	41.32	1.12	6
-97.376	36.63	XR-OWE2	41.70	1.17	7
-97.375	36.349	NX-STN15-	41.65	2.50	54
-97.346	36.46	XR-RR01	43.25	3.10	8
-97.338	35.581	GS-OK025-00	47.24	3.96	19
-97.327	36.547	XR-GLE1	39.78	2.06	6
-97.304	36.407	GS-OK049-00	39.56	4.32	5
-97.267	36.176	NX-STN09-	40.96	2.58	63
-97.261	36.365	XR-PER1	40.20	1.88	10
-97.235	36.26	O2-PERY-	40.73	1.88	32
-97.215	36.761	OK-BLOK-	42.67	3.04	45
-97.197	36.655	NX-STN23-	42.03	2.13	57
-97.197	36.659	XR-MIL1	42.73	0.97	3
-97.186	35.926	NX-STN03-	43.12	1.68	52
-97.13	35.926	O2-PERK-	43.45	2.74	25
-97.127	36.349	NX-STN16-	40.36	1.79	65
-97.061	35.561	OK-CHOK-	45.09	3.61	69
-97.044	36.279	O2-PW18-	40.10	1.78	11
-97.036	36.569	O2-PW19-	41.83	2.72	14
-97.023	35.343	O2-SHWN-	41.29	3.36	19
-97.014	36.469	O2-PW15-	42.03	2.21	9
-96.982	36.395	GS-OK050-00	41.77	1.90	10
-96.972	36.421	O2-PW06-	41.80	0.66	3
-96.964	36.485	O2-PW05-	42.16	2.47	16
-96.946	34.728	O2-SC13-	45.34	2.05	11
-96.944	36.416	GS-OK048-00	40.35	2.37	72
-96.938	36.044	GS-OK033-00	45.15	2.96	42
-96.929	36.402	O2-PW01-	41.00	0.46	3
-96.925	36.448	GS-OK045-00	41.27	1.86	9
-96.908	36.4	NX-STN17-	40.75	1.77	53
-96.907	36.397	GS-OK046-00	40.83	2.56	14

-96.874	35.153	OK-W35A-	42.17	3.33	46
-96.858	36.419	O2-PW02-	40.42	0.77	5
-96.839	35.953	GS-OK031-00	40.69	3.01	46
-96.836	36.505	GS-OK051-00	40.00	2.37	48
-96.818	36.328	O2-PW13-	41.50	2.47	10
-96.817	36.448	O2-PW09-	41.11	1.02	10
-96.803	35.994	GS-OK052-00	43.47	3.15	68
-96.796	36.373	GS-OK044-00	41.65	2.63	10
-96.79	35.442	NX-STN35-	43.48	2.95	58
-96.788	36.014	GS-OK053-00	41.92	2.71	9
-96.785	35.653	O2-CHAN-	46.29	3.51	29
-96.732	36.159	NX-STN11-	42.89	2.94	64
-96.724	36.469	GS-OK047-00	41.30	1.13	2
-96.721	35.657	NX-STN33-	44.17	3.51	52
-96.713	36.01	GS-OK034-00	44.54	3.68	20
-96.647	36.418	NX-STN18-	43.12	2.08	58
-96.645	35.847	NX-STN05-	42.37	2.73	58
-96.605	35.919	O2-DRUM-	42.10	2.42	24
-96.565	35.294	O2-SMNL-	42.75	3.00	22
-96.498	35.843	OK-DEOK-	46.77	2.98	72
-96.492	36.259	NX-STN12-	45.26	3.04	59
-96.492	36.259	GS-OK041-00	41.26	3.70	5
-96.492	36.259	GS-OK030-00	42.41	2.67	31
-96.492	36.259	GS-OK037-00	48.99	4.50	8
-96.492	36.259	O2-FW06-	39.01	2.42	11
-96.492	36.259	XR-GRA1	43.02	0.96	9

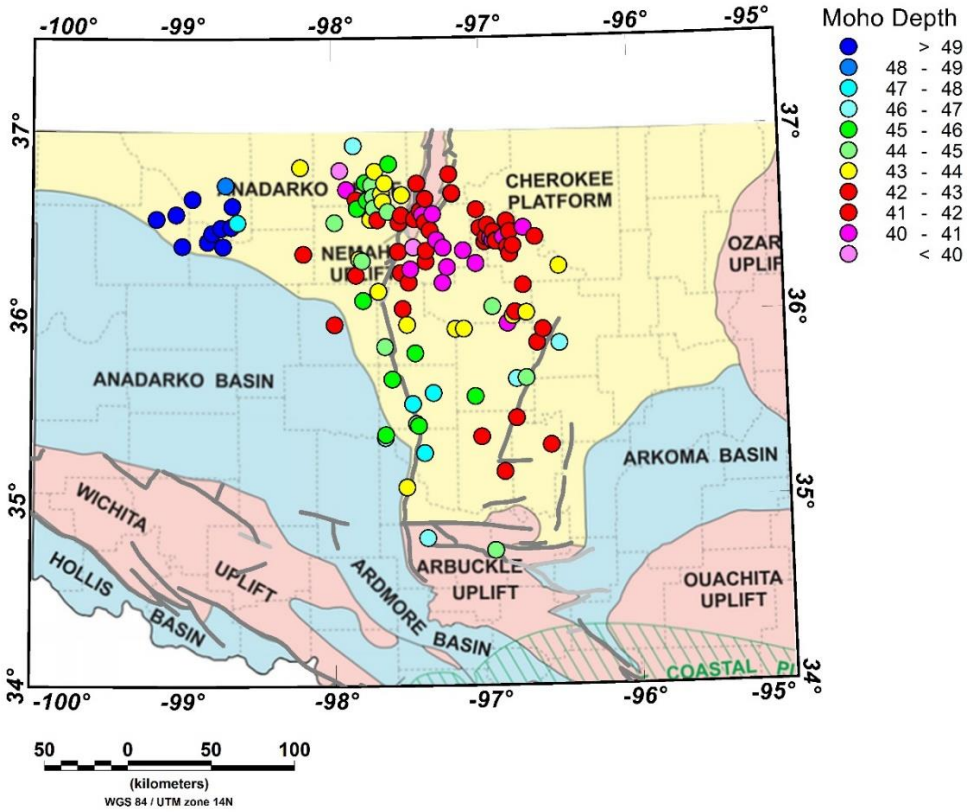


Figure A 4 The semi-automatically picked Moho depth of each station. The result is shown in 11 intervals from 40 to 49. The color range corresponds to the same color range of interpolated Moho map (Figure 2.5).

A3. Uncertainty analysis

We define the uncertainty of Moho estimation from depth-converted RF as the standard deviation of the semi-automatically picked Pms phase from individual RFs of one station. The time-domain RFs of the individual station are moveout corrected regarding the event-station epicentral distance and then converted to depth with a tomography-derived Oklahoma crust velocity model (Retra and Behm, 2021). A manually picked Pms from stacked RF is designated to the searching

algorithm as a reference depth. The Pms of individual RF traces are then picked around the reference depth.

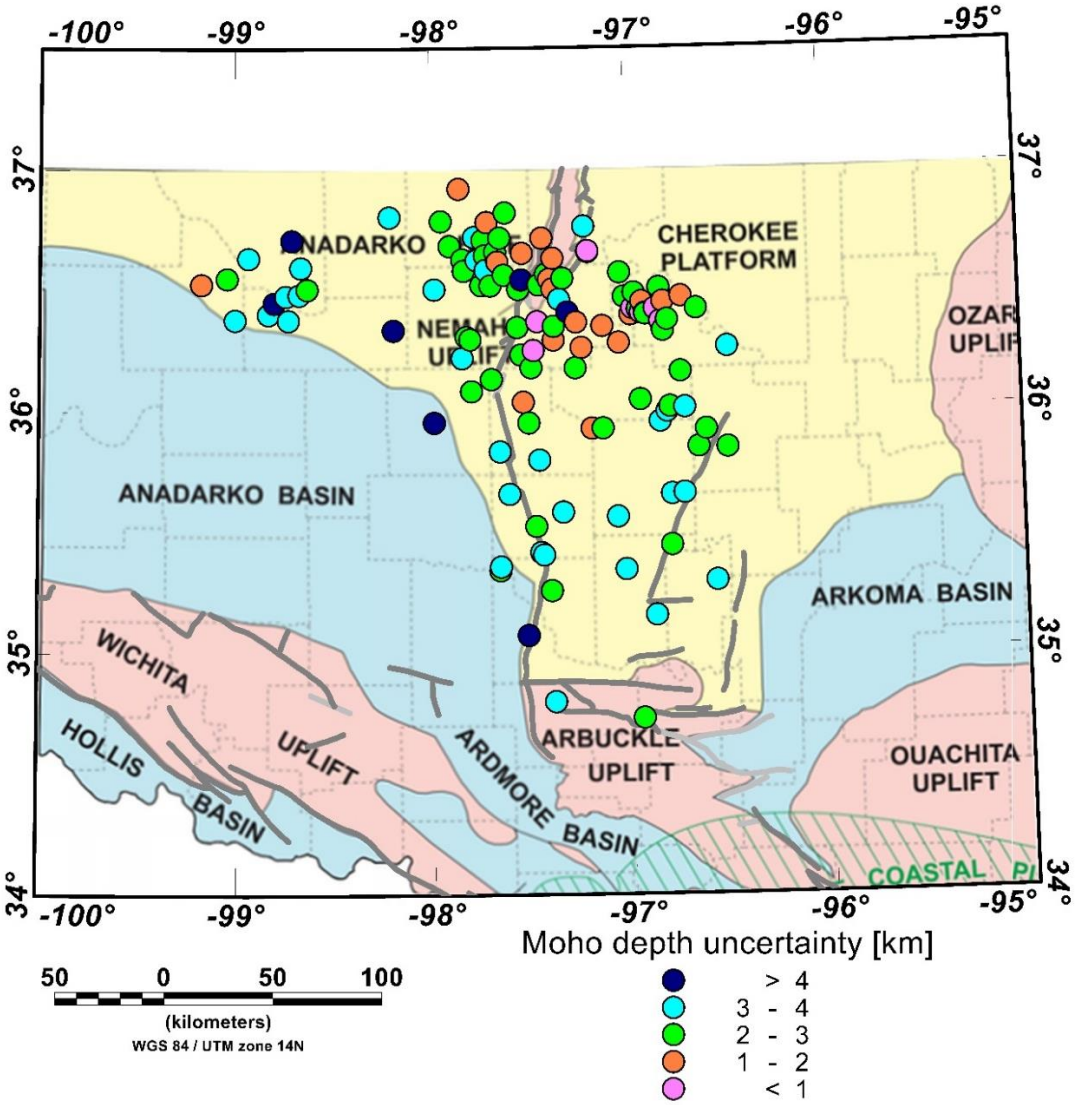


Figure A 5 Uncertainty of individual stations for Moho map interpolation. Note the majority of stations have the error of Moho depth estimation of 1-4 km.